# Spatio-temporal variability in Southern Hemisphere Glacier Snowline Altitudes from 2000-2020

**Mia Weller Macfee**

Submitted in accordance with the requirements for the degree of

Master of Science by Research

The University of Leeds

School of Geography

September 2023

The candidate confirms that the work submitted is her own and that appropriate credit has been given where reference has been made to the work of others.

## Acknowledgements

Firstly, this research would not be half the success without the untiring enthusiasm and support of my supervisors, Professor Jonathan Carrivick, and Professor Duncan Quincey. I would like to give a huge thanks to both, for the time and wisdom they have offered, the stimulating questions they have brought to the table in supervision meetings, and the confidence they have shown in my abilities and research. I was either very lucky to receive such fantastic guidance throughout the year, or the beers I 'bribed' them with at Christmas paid off.

I would also like to extend thanks to fellow postgraduate researcher, Chris Stringer, who made a brilliant counsellor for all Google Earth Engine related hurdles in the early days of the project, and whose support for this research is also very much appreciated.

Thank you finally to my family, friends, and partner for the unreserved optimism and encouragement they have shown me this year.

## Abstract

The glacierised Southern Hemisphere is vulnerable to continued shrinkage under climate change, but representation of these mountainous regions in climate research is limited by hemispheric and altitudinal scarcity of meteorological observations. End-of-summer snowline altitude ($SLA_{EOS}$) indicates glacier response to climatic forcing, though has been estimated with low spatio-temporal coverage for the Southern Hemisphere. This study presents the first Southern Hemisphere-wide quantification of $SLA_{EOS}$, with analysis of regional and intra-regional trends. An automated approach was implemented in Google Earth Engine, in which glacier snow cover was classified in Landsat scenes using Otsu image segmentation and $SLA_{EOS}$ was estimated as the lowest altitude from which snow cover ratio was continuously > 0.5. Results encompassed 6485 glaciers of the Southern Alps, Andes, and Antarctic Peninsula, with trends calculated from 2000-2020. Snowlines underwent widespread retreat in this period; mean rates of $SLA_{EOS}$ rise were between 2.19 and 6.28 m $yr^{-1}$ for regions, between 1.63 and 7.55 m $yr^{-1}$ for east/west sub-regions, and were mostly accelerated for the recent decade (2010-2020). Mean $SLA_{EOS}$ lowering (-30 to -1 m $yr^{-1}$) indicated stability in the southernmost Andes, contrasting to rapid $SLA_{EOS}$ rise (10 to 30 m $yr^{-1}$) in the southern Central Chilean Andes, and eastern slopes generally experienced increased rates of $SLA_{EOS}$ rise compared to western slopes. $SLA_{EOS}$ variability was reflected in periods of summer warming and reductions in summer snowfall, though correlation with these variables was not consistently identified. East-west and north-south disparities in absolute $SLA_{EOS}$ and rates of $SLA_{EOS}$ change were linked to spatial variability in terrain elevation and prevailing moisture transport, with the latter evidencing the variability and impact of large-scale climatic modes. Given implications of observed trends for glacier mass loss, continued research may involve developing an annually-updated global dataset, investigating additional drivers of $SLA_{EOS}$ variability, and estimating glacier response times.

## Table of Contents

## List of Figures

### Main



### Appendix A: ERA5-Land climate maps

## List of Tables

### Main



### Appendix B: Study region information

# 1. Introduction

## 1.1. Glaciological and climatological change

Glaciers are key components of the cryosphere and pivotal indicators of global climatic variation (Bojinski et al., 2014; Oerlemans, 1994). On account of glaciological sensitivity to climate change, recent decades have seen a severe overall deterioration of glaciers and of snow cover across mountain regions (Fox-Kemper et al., 2021; Hock et al., 2019). Global glacier mass loss equated to 267 ±16 Gt $yr^{-1}$ for 2000 to 2019 (Hugonnet et al., 2021), with the Sixth Assessment Report of the Intergovernmental Panel on Climate Change (IPCC) identifying polar regions as hotspots of the highest magnitude climate changes (Constable et al., 2022), and mountain regions as among the most sensitive to climate impacts (Adler et al., 2022). Snow cover is a particularly sensitive indicator of climate, and its extent and duration has been in decline for almost all world regions since the mid-20$^{th}$ century (Hock et al., 2019).

With glaciological imbalance expected to continue throughout the 21$^{st}$ century regardless of climate stability (Zemp et al., 2015), concerns are raised for the ongoing environmental and social impacts of glacier mass loss, which cover local to global scales. Globally, glacier mass loss is a key contributor to sea level rise (Gardner et al., 2013; Zemp et al., 2019), while regionally, glacier mass loss drives critical changes to natural hydrological systems (Bliss et al., 2014; Huss and Hock, 2018) and to the potential for cryospheric hazards (Stoffel and Huggel, 2012). Livelihoods dependent on local glaciers will continue to face long-term changes to hydrological resources used for hydropower, agriculture, and consumption (Milner et al., 2017), as well as likely deterioration of the glacier tourism industry (Stewart et al., 2016). Monitoring glacier variation in the context of an unstable climate is, therefore, critical and timely.

Climate monitoring is currently limited by the clear disparity in coverage of climate records between the Northern and Southern hemispheres. The coverage of Global Historical Climatology Network-daily (GHCNd), one of the largest networks of land-based climate observations, is over 3.7 times greater in the Northern Hemisphere (Figure 1); the disparity is also enhanced for mountain regions (Thornton et al., 2022) and, therefore, for many glacierized regions (e.g., Southern Alps, Andes, and Antarctica; Figure 1). This affects representation of high-altitude Southern Hemisphere regions in climate research; for instance, a recent study into global scale high elevation warming trends used data collected from 2,104 global stations, of which only 138 (6.6%) were situated in the Southern Hemisphere (Qixiang et al., 2018). Larger scarcity of climate records in the Southern Hemisphere is evidenced in this lower temporal and spatial coverage of surface-based observations compared to the Northern Hemisphere (Barrell et al., 2013; Jones et al., 2016; Morris and Vaughan, 2003; Schauwecker, 2011; Schauwecker et al., 2017), but also in lack of proxy records for large scale and long-term temperature reconstructions (Mann et al., 2008; Neukom et al., 2014). Either by direct or proxy climate observations, further data

collection needs to be undertaken to increase knowledge of climate change in the Southern Hemisphere; thus, increasing reliability of global climate change knowledge and inter-hemispheric comparisons.

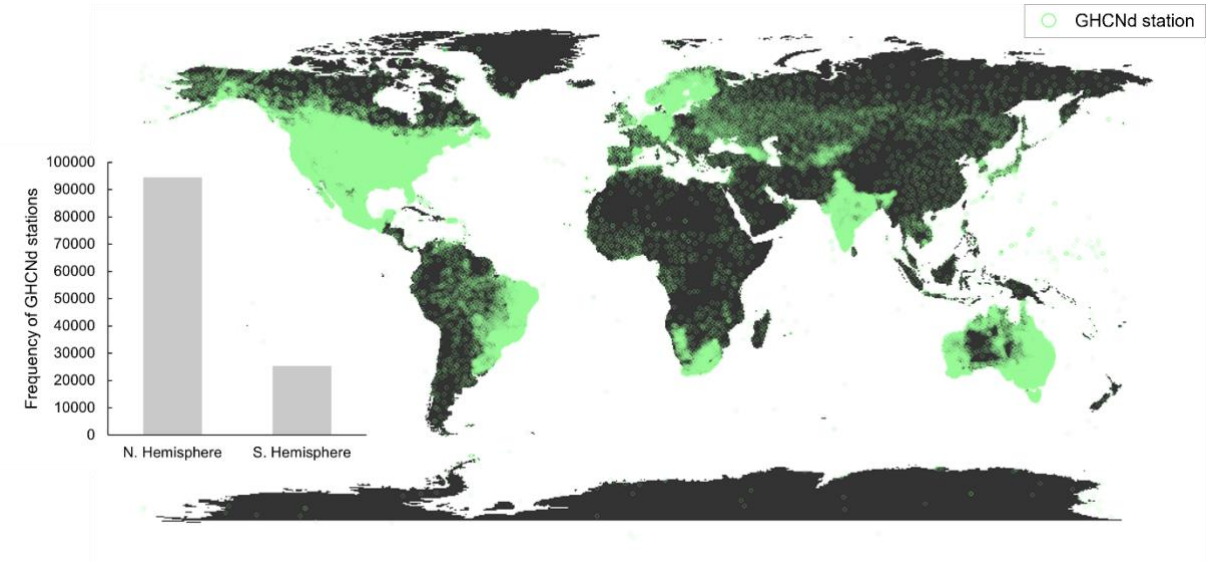


**Figure 1.** Frequency and distribution of GHCNd climatological recording stations in Northern and Southern hemispheres (based on data from the National Oceanic and Atmospheric Administration: https://www.ncei.noaa.gov/products/land-based-station/global-historical-climatology-network-daily). Particularly limited coverage in Southern Hemisphere glacierized regions of the Southern Alps (New Zealand), Andes (western South America), and Antarctica.

Derived from the limited existing data, potential future climate change impacts in glacierized regions of the Southern Hemisphere are particularly concerning; for instance, the dry Andes is one of the most critical regions for understanding future changes in water resource seasonality (Adler et al., 2022; Masiokas et al., 2020), and the Antarctic Peninsula is experiencing some of the highest magnitudes of warming (Constable et al., 2022). The glacierized area of the Andes, Southern Alps, and Antarctic Peninsula covers a range of climatic settings from maritime to semi-arid. Current understanding is that Southern Hemisphere glaciers with maritime situation are subjected to high precipitation from westerly air flows over surrounding oceans (Fitzharris et al., 2007) which increases their temperature sensitivity (Anderson et al., 2010), while glaciers with semi-arid situation experience increased precipitation sensitivity (Kinnard et al., 2020). Due to the limited coverage of climate recording stations in the glacierized Southern Hemisphere, this enhanced climatic sensitivity of Southern Hemisphere glaciers can be utilised in the provision of glaciological proxy climate records for these data-sparse regions. Uniform and comprehensive collection of proxy climate observations across the Southern Hemisphere would also aid understanding of potential spatial variation in glacier-climate relationships, which are likely to exist across this large scale.

### 1.2. Snowline altitude (SLA)

Evolution of glacier state in response to climatic fluctuations can be indicated by spatio-temporal variation in glaciological parameters. Glacier evolution is ideally determined by direct mass balance estimations using in-situ observations with snow pits and stakes (e.g., Kaser et al., 2003). However, these methods are associated with significant financial and practical requirements, especially in alpine regions where terrain is often rugged or inaccessible; they are therefore only applicable to a fraction of glaciers globally. As mass balance is the sum of accumulation in the upper glacier and ablation in the lower glacier, it may also be determined from observations of where these two processes are balanced. The equilibrium line altitude (ELA) marks the elevation of accumulation and ablation balance (Benn and Lehmkuhl, 2000), and is confirmed to be highly correlated with overall glacier mass balance (Braithwaite, 1984). Monitoring of the glacier ELA can therefore provide an efficient approximation of the glacier state. Snowlines mark the transient snow-ice boundary on a glacier and reach a maximum altitude at the end-of-summer (EOS) ablation season. At this elevation, net mass balance of a glacier is zero (Meier and Post, 1962), meaning snowline altitude (SLA) at the end of summer is a proxy for ELA (Figure 2) and can, therefore, be used as a means of assessing mass balance variation (Cuffey and Paterson, 2010; McFadden et al., 2011; Paterson, 1994; Rabatel et al., 2005; Rabatel et al., 2012; Tawde et al., 2016). Consequently, studying spatio-temporal variations in end-of-summer SLA ($SLA_{EOS}$) provides estimates of glacier snow cover trends which are a proxy indicator of climate forcing on the cryosphere (Chinn, 1995). Aided by recent improvements in spatial and temporal resolution of freely available satellite datasets, remote sensing methods can be used to efficiently discern the glacier $SLA_{EOS}$, which is generally visible in optical imagery due to the reflectance differences of snow and ice (Dozier, 1989).

A majority of previous research has observed and quantified SLA for individual glaciers or individual catchments (Falaschi et al., 2013; Gaddam et al., 2022; Huang et al., 2011; Veettil et al., 2017; López-Moreno et al., 2014; Pandey et al., 2013; Simões et al., 2015). Where glacier to catchment scale observations may provide basin-specific information to resource managers on the responses of local glacier dynamics to the environment (Prieur et al., 2022), regional scale observations also provide opportunity to assess the prevailing trends in glaciological response, and spatial variation in those trends. However, there are few published analyses of glacier SLA with regional, national, or continental coverage. This dearth of larger-scale studies is attributed to manual computational analysis of individual snowlines being time-consuming over larger spatial scales, despite being time-effective compared to field-based observation.

There has been recent emergence of studies calculating glacier SLA using automated algorithms (e.g., Li et al., 2022; Liu et al., 2021; Loibl et al., 2022; Racoviteanu et al., 2019; Rastner et al., 2019); such studies exhibit an opportunity to significantly reduce the time consumption of large-scale analyses.

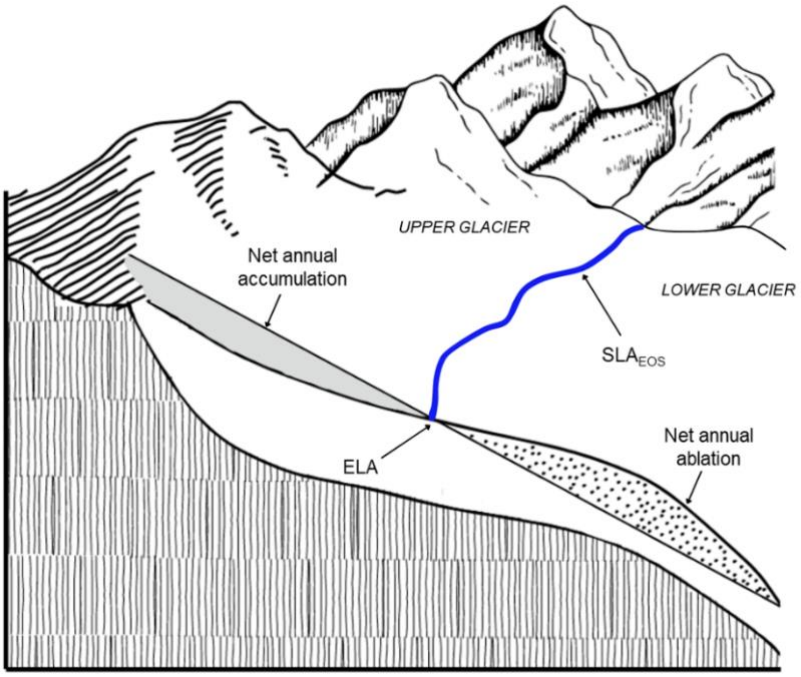


**Figure 2.** Stratigraphic glacier diagram illustrating equality of annual maximum SLA ($SLA_{EOS}$; blue) and ELA, and correlation of ELA position with mass balance parameters of net annual accumulation and net annual ablation.

Despite this opportunity, present applications of automated SLA detection, as with all methods of SLA detection, have also been primarily concentrated on limited samples of glaciers; for example, Rastner et al. (2019), Li et al. (2022), and Racoviteanu et al. (2019) consider just 26, 14, and 10 glaciers respectively. Upon concluding successful accuracy (73-80%) of these methods (Li et al., 2022; Rastner et al., 2019), there is definitive scope to expand the spatial extent of such studies to include a larger glacier sample in a single analysis. To illustrate, Loibl et al. (2022) applied an automated band ratio-based algorithm to over 100,000 Landsat scenes, retrieving regular SLA data for every glacier in High Mountain Asia larger than 0.5 $km^2$. To date, this is the most comprehensive retrieval of SLA data; however, as with all existing applications of automated SLA delineation, analysis is contained in the Northern Hemisphere. Regions receiving particular attention from such studies are High Mountain Asia (e.g., Li et al., 2022; Loibl et al., 2022; Liu et al., 2021; Racoviteanu et al., 2019), and the European Alps (e.g., Prieur et al., 2022; Rastner et al., 2019). In contrast, there have been no automated studies producing glacier-scale SLA records with continental spatial coverage in Southern Hemisphere regions.

There is a clear need to extend spatial coverage of $SLA_{EOS}$ observations across Southern Hemisphere glaciers to, (a) reduce the geographical bias in automated snowline detection, (b) provide these regions with more spatially and temporally comprehensive records of glaciological change, and (c) strengthen understanding of climate change in data-sparse regions. This thesis therefore aims to quantify regional $SLA_{EOS}$ change across the entire glacierized Southern Hemisphere.

# 2. Literature review

## 2.1. SLA identification

Across automated, semi-automated, and non-automated studies, remote sensing of glacier snowlines has been conducted using a range of imagery datasets. Where some studies have utilised satellite-derived synthetic aperture radar (SAR) (Fu et al., 2020; Zhou et al., 2022) for omission of atmospheric conditions, or aerial photography (Chinn, 1995; Lorrey et al., 2022) for increased image resolution, a majority of studies have utilised multi-spectral satellite imagery, such as Landsat TM/ETM+/OLI, ASTER, and MODIS (Davies et al., 2012; Gaddam et al., 2022; Guo et al., 2021; Li et al., 2022; López-Moreno et al., 2014; Pelto, 2011). Although Sentinel-2 multi-spectral imagery provides opportunity to map snow cover at higher spatial and temporal resolution (Hofmeister et al., 2022) and prospective SLA detection on Sentinel-2 imagery has been encouraged (Li et al., 2022; Racoviteanu et al., 2019), the dataset has been rarely used in such studies due to its restricted temporal coverage (post-2013). Automated methods which aimed to identify long-term SLA variability required satellite datasets which have high spatial resolution, consistent temporal resolution, and extended temporal coverage, to increase robustness of calculated trends (Prieur et al., 2022); therefore, such studies have typically favoured the use of Landsat imagery (e.g., Li et al., 2022; Wang et al., 2023).

Remote sensing of SLA necessitates accurate identification of snow cover and bare ice on a given glacier; several methods of snow identification and classification have been developed for use on multi-spectral imagery. Normalized Difference Snow Index (NDSI), for instance, is calculated by the normalized difference of green and shortwave-infrared (SWIR) bands. Like many studies, Girona-Mata et al. (2019) and Parla et al. (2020) applied a threshold (0.45 and 0.6, respectively) to the NDSI of Landsat scenes to classify snow (above threshold) and ice (below threshold), subsequently delineating SLA for glaciers in the Himalaya and Canadian Arctic. Conversely, due to sensitivity of the near-infrared (NIR) band to specific surface area of snow (Matzl and Schneebeli, 2006), thresholds have been applied to histograms of NIR band pixels to classify the glacier snow-covered area (Rastner et al., 2019). Additionally, the NIR band is frequently used in spectral band combinations (Pelto, 2011; Zhang and Kang, 2017) and ratios (e.g., Hall et al., 1987; Li et al., 2022) to detect snowlines. Racoviteanu et al. (2019) applied a threshold to images calculated from the band ratio of NIR/SWIR, delineating SLA for glaciers in two catchments of High Mountain Asia. Li et al. (2022) subsequently compared the thresholding of the NIR band to the thresholding of NIR band ratios, finding that a combination of NIR and NIR/SWIR methods enhances glacier cover classification results.

Irrespective of snow identification method, studies have typically used a uniform threshold value in snow classification; for instance, the NDSI threshold of 0.4, suggested in Hall et al. (1995). Due to strong spatial heterogeneity in snow characteristics globally, some studies have deviated from suggested

threshold values, based on updated research or manual inspection of their region of interest (e.g., Girona-Mata et al., 2019). However, Liu et al. (2021) highlights that even threshold values used uniformly across smaller regional scales may not be effective, due to strong variation in cloud conditions between glaciers and image scenes. Therefore, it is advantageous for SLA delineation studies to constrain snow classification thresholds on a case-by-case basis. This has been achieved in some studies by the statistical thresholding method of Otsu image segmentation (Otsu, 1979); for example, in Li et al. (2022) and Wang et al. (2023). However, use of statistical thresholding for case-by-case snow classification has not yet been achieved in Southern Hemisphere glacier SLA analyses.

### 2.2. Existing Southern Hemisphere SLA records

Existing glacier SLA records for the Southern Hemisphere typically have limited spatial coverage and variable temporal distribution (Table 1). The number of independent records is greatest for the Andes; however, the spatial and temporal comprehensiveness of records is presently greatest for the Southern Alps (Table 1), owing to the long-term New Zealand end-of-summer snowline survey which provides the largest available database of Southern Hemisphere glacier SLAs.

The New Zealand end-of-summer aerial photograph survey documents $SLA_{EOS}$ since 1977 for < 51 Southern Alps glaciers (Chinn, 1995; Lorrey et al., 2022). Although this study ensured that index glaciers had even spatial distribution, the survey is spatially limited in its neglect of several hundreds of Southern Alps glaciers; increasing the sample size of glaciers studied is needed to enhance reliability of regional $SLA_{EOS}$ trend calculations. Technical issues inherent to the survey also limit its result accuracy; Chinn (1995) stated that (a) the flight date is selected with bias for clear weather conditions, (b) typically only one flight can be conducted per year, and (c) $SLA_{EOS}$ estimates are made by visual comparisons to contour maps. Abrahim et al. (2023) also identifies that, with the Southern Alps ablation season extending, there is increasing possibility that the annual surveys have not captured the true $SLA_{EOS}$. Methods that analyse snowlines on a range of dates throughout the end-of-summer period may, therefore, be preferable.

For the Andes, SLAs of individual glaciers (e.g., Hanshaw and Bookhagen, 2014; Rabatel et al., 2012; Veettil and Simões, 2019), cordilleras (e.g., López-Moreno et al., 2014; McFadden et al., 2011; Veettil et al., 2016a; Veettil et al., 2017), or regional latitudinal ranges (e.g., Saavedra et al., 2018; Schauwecker et al., 2022) have previously been determined by non-automated (e.g., manual classification) and semi-automated (e.g., supervised classification) remote sensing methods. The temporal coverage for each of these Andean studies is reasonable, spanning a minimum of one decade. However, the temporal resolution of results is not always annual; for instance, McFadden et al. (2011) examines just five years in the 1986-2002 period, and Hanshaw and Bookhagen (2014) examines just three years in the 1988-2009 period. Therefore, opportunity for comparisons of inter-annual SLA variability are presently

limited. Additionally, the spatial coverage of studies is mostly irregular, meaning validation and comparison of SLA findings within regions is also limited. Saavedra et al. (2018) is an exception to this, with reasonable spatial coverage of SLA findings (~9-36˚S); yet, even with these findings, the Central Chilean and Southern Andes (< 56˚S) remain heavily understudied for glacier SLA trends.

Similarly for the Antarctic Peninsula, the few existing SLA studies conduct non-automated analysis which is irregularly distributed spatially and temporally; for instance, Falk et al. (2016) studies Warszawa Icefield on King George Island from 2010-2011, Simões et al. (2015) studies Collins Glacier on King George Island from 1983-2006, and Simões et al. (2020) studies Drummond and Widdowson glaciers from 1986-2016. Inter-annual variability in SLA is overlooked in each of these studies; Simões et al. (2015) covers the widest temporal range, but only examines SLA on four years in the 1983-2006 period. Further, each of these studies analyse an individual glacier or icefield; therefore, spatial coverage of Antarctic Peninsula SLA findings is extremely limited. Satellite-derived snowline studies have been carried out for the Peninsula with larger spatial and temporal coverage (Zhou et al., 2017; Zhou et al., 2022), but these record perennial dry-snowline altitude which must be noted as unique from the seasonally transient $SLA_{EOS}$.

### 2.3. Temporal and spatial SLA trends

Drawing from the few existing records, temporal trends of SLA in the Southern Hemisphere appear to be well aligned with global-scale trends of glacier mass loss, thinning, and retreat identified in Zemp et al. (2015) and Zemp et al. (2019). Results from the New Zealand aerial survey indicate an overall rise (3.84 m $yr^{-1}$) in Southern Alps $SLA_{EOS}$ since 1977, and a steepening rate of $SLA_{EOS}$ rise in recent decades (Chinn, 1995; Lorrey et al., 2022). Multiple studies similarly report overall increases in SLA for glaciers and ice caps in the Peruvian Andes (e.g., Hanshaw and Bookhagen, 2014; López-Moreno et al., 2014; McFadden et al., 2011; Veettil and Simões, 2019; Veettil et al., 2016a; Veettil et al., 2017), Chilean Andes (e.g., Saavedra et al., 2018), and Antarctic Peninsula (Simões et al., 2015), with documented rates of SLA rise greatest for the Chilean Andes between 29-36˚S (10-30 m $yr^{-1}$). However, contradictory to most SLA trends, Rabatel et al. (2012) report SLA data for Zongo Glacier, Bolivia, which indicate a small overall SLA lowering of ~15 m from 1996-2006. Where overall temporal SLA trends are reasonably well reported in these studies, information on the inter-decadal variability in gradients of SLA change is undocumented outside of the Southern Alps. This indicates the present shortage of studies with extended temporal coverage and annual resolution.

Wide inter-annual variability in SLA is only reported for individual glaciers in the Southern Alps (Lorrey et al., 2022) and Peruvian Andes (Veettil et al., 2016a); but similarly, other studies have reported strong inter-annual variability in snow cover extent, such as Cordero et al. (2019) for the

**Table 1.** Existing SLA findings for the Southern Hemisphere.

| Region/Glacier | Date range | Method | Key SLA finding | Reference |
|---|---|---|---|---|
| Andes (~9-36˚S) * | 2000-2016 | Remote sensing (non-automated) | Rate of SLA rise is significant from 29-36˚S at +10-30 m $a^{-1}$ | Saavedra et al. (2018) |
| Cerro Tilata, Bolivia (n=1) | 2002-2017 | Remote sensing (non-automated) | Overall SLA rise of 51 m** | Veettil and Simões (2019) |
| Nevado Champara, Peru (n=1) | 2002-2017 | Remote sensing (non-automated) | Overall SLA rise of 39 m; but larger SLA rise from 2011-2016 of 48 m** | Veettil and Simões (2019) |
| Zongo Glacier, Bolivia (n=1) | 1996-2006 | Remote sensing (non-automated) | Overall SLA lowering of 15 m*** | Rabatel et al. (2012) |
| Artesonraju Glacier, Peru (n=1) | 2000-2010 | Remote sensing (non-automated) | Overall SLA rise of 200 m*** | Rabatel et al. (2012) |
| Cordillera Blanca, Peru (n=11) | 1984-2015 | Remote sensing (non-automated) | Overall mean SLA rise of 98 m **** | Veettil et al. (2017) |
| Cordillera Ampato, Peru (n=5) | 1986-2014 | Remote sensing (non-automated) | Overall mean SLA rise of 92 m ***** | Veettil et al. (2015) |
| Cordillera Huaytapallana, Peru (n=6) | 1984-2011 | Remote sensing (semi-automated) | Overall SLA rise of 93-157 m dependent on region | López-Moreno et al. (2014) |
| Cordillera Huayhuash, Peru (n=13) | 1986-2005 | Remote sensing (semi-automated) | Overall mean SLA rise of 24 m | McFadden et al. (2011) |
| Cordillera Raura, Peru (n=18) | 1986-2002 | Remote sensing (semi-automated) | Overall mean SLA rise of 97 m | McFadden et al. (2011) |
| Quelccaya Ice Cap, Peru (n=1) | 1988-2009 | Remote sensing (semi-automated) | Overall SLA rise of 70 m | Hanshaw and Bookhagen (2014) |
| Coquimbo Region, Chile * | 2011-2021 | Remote sensing (non-automated) | SLA varies 820-3880 m across all scenes | Schauwecker et al. (2022) |
| Warszawa Icefield, King George Island, AP (n=1) | 2010-2011 | Remote sensing (non-automated) | Mean SLA of 220 m across the period | Falk et al. (2016) |
| Collins Glacier, King George Island, AP (n=1) | 1989-2006 | Remote sensing (non-automated) | Overall SLA rise of ~30 m | Simões et al. (2015) |
| Drummond Glacier, AP (n=1) | 2016 | Remote sensing (non-automated) | SLA of 100 m | Simões et al. (2020) |
| Widdowson Glacier, AP (n=1) | 2016 | Remote sensing (non-automated) | SLA of 200 m | Simões et al. (2020) |
| Southern Alps, New Zealand (n=41) | 1977-2020 | New Zealand EOS aerial survey | Rate of SLA rise +3.84 m $a^{-1}$ | Lorrey et al. (2022) and Chinn (1995) |

*Number of glaciers unspecified.
**Estimated from Figure 2 in Veettil and Simões (2019).
***Estimated from Figure 7 in Rabatel et al. (2012).
****Estimated from Figure 4 in Veettil et al. (2017).
*****Estimated from Figure 4 in Veettil et al. (2016a).

Chilean Andes. Both SLA and snow cover variability have been attributed to accumulation and ablation anomalies driven by modes of climatic variability (Masiokas et al., 2020). Importantly, Lorrey et al. (2022) indicates that analysing these high variability glaciers in isolation can lead to overestimations in annual snowline departures, and that results are better presented in the context of the regional population of results. Across continental regions of the Southern Hemisphere, SLA has been reported to follow spatial trends along east-west and north-south gradients. Although Chinn (1995) does not explore the spatial trends in SLA change through time, this snowline survey study does indicate that glacier SLA in the eastern and northern-facing Southern Alps generally exceeds that in the western and southern-facing sites. Concurrently, Saavedra et al. (2017) highlighted the reduction in minimum elevation of snow cover toward the south and west of the Andes, whilst Davies et al. (2012) also acknowledges existence of lower glacier SLA in the western Antarctic Peninsula. Additionally, Saavedra et al. (2018) identifies east-west gradients in rates of SLA change in the Andes; the study found that rates of SLA increase were greater for western glaciers between 30-32˚S, but greater for eastern glaciers between 34-36˚S. Similar analysis for the Southern Alps and Antarctic Peninsula has not been documented; however, Carrivick and Chase (2011) does report more negative departures of annual ELA from steady-state ELA towards the south and west of the Southern Alps, which may indicate SLA change trends. The dearth of analysis on the spatial trends in rates of SLA change at large scales points again to the current lack of Southern Hemisphere SLA records with suitable spatial and temporal coverage.

Spatial variability in glacier SLA is also scarcely reported within smaller scale sites, despite the importance of understanding intra-catchment glacier variability being previously highlighted (Carrivick and Chase, 2011). McFadden et al. (2011) identifies the significantly contrasting rates of SLA change at two Andean cordilleras which are both situated within 10-10.5˚S. Although spatially incomparable, the finding of strong spatial variability in glacier behaviour within Andean sites is supported in Melkonian et al. (2013), which highlights the contrasting areal changes of neighbouring glaciers within the Cordillera Darwin of the Southern Andes. The scale of intra-site SLA variability addressed in McFadden et al. (2011) is not replicated for studies outside of the Andes; however, Davies et al. (2012) does highlight the significantly contrasting rates of glacier recession within the Trinity Peninsula site of the northern Antarctic Peninsula, which may complement intra-site observations of SLA change when they become available.

### 2.4. SLA-climate associations

Lorrey et al. (2022) identified that Southern Alps snowlines were mostly guided by a strong correlation between glaciers and regional summer temperatures, drawing parallels between the highest annual SLAs and timings of local marine heatwaves. Clare et al. (2002) similarly related Southern Alps SLA variation to regional temperature anomalies, but additionally noted the association of higher (lower)

annual SLAs with weaker (stronger) westerlies and reduced (enhanced) precipitation, which are typical of El Niño (La Niña) conditions (Fitzharris et al., 2007). This view is corroborated in Ohmura (1992), which suggests approximate linear association of ELA change with both temperature and precipitation. Both Lorrey et al. (2022) and Clare et al. (2002) contain SLA-climate analysis conducted using index glaciers and $SLA_{EOS}$ data derived from the New Zealand end-of-summer snowline survey. The addition of SLA records with more comprehensive coverage of the Southern Alps should aid identification of a primary climatic control in this region.

Similarly for the Andes, parallels have been drawn between the climatic changes associated with El Niño and La Niña events, and glacier SLA; however, these relationships are understood to differ across a latitudinal gradient. It is suggested that air temperature variability has primary control over SLA in lower southern latitudes of the tropics and sub-tropics (Francou et al., 2004), where El Niño events are related to warming and drying (Masiokas et al., 2020). Meanwhile, a prolonged dry period is thought to be driving SLA change in mid-to-high southern latitudes (Garreaud et al., 2017), despite El Niño events causing anomalously high precipitation at slightly higher southern latitudes (Masiokas et al., 2006). SLA-climate relationships in the Andes are complex and not consistently applicable, according to Masiokas et al. (2006). Concurrently, Taylor et al. (2022) indicates that temperature and precipitation were separately identified as the primary driver of glacier change for two cordilleras of similar sub-tropical latitude (Fyffe et al., 2021; López-Moreno et al., 2014). Under potential for increasing El Niño frequency (Wang et al., 2017), it is important to constrain understanding of these complex relationships, aided by more comprehensive SLA records.

There is a larger consensus amongst studies focused on the Antarctic Peninsula regarding glacier-climate relationships. Precipitation sensitivity is negligible for Antarctic Peninsula glaciers, with Charton et al. (2021) only acknowledging high precipitation sensitivity for glaciers in sub-Antarctic regions. Correspondingly, multiple studies confirmed glaciers to have higher temperature sensitivity than precipitation sensitivity in the mainland peninsula (Abram et al., 2013), James Ross Island (Davies et al., 2014), and Livingston Island (Navarro et al., 2013). This is corroborated by findings in Rau et al. (2000) that spatial variations in snowline are well aligned with spatial variations in temperature across the Antarctic Peninsula. However, with the gradient of increasing aridity that spans west to east across the peninsula, the ELAs of precipitation-deficient glaciers in the east are recorded by multiple studies as being more sensitive to air temperature changes than those in the west (Davies et al., 2011; Davies et al., 2012; Engel et al., 2023). An understanding of the relative importance of spatial variations in temperature and aridity in SLA-climate relations across the Antarctic Peninsula is, therefore, yet to be constrained.

### 2.5. $SLA_{EOS}$, ELA and mass balance

When interpreting variations in glacier $SLA_{EOS}$, it is necessary to consider the complex relationship of snowlines, mass balance and ELA. As noted in *1.2.*, total mass balance and ELA are reflected in the total sum of accumulation and ablation processes on a glacier (Benn and Lehmkuhl, 2000; Cogley et al., 2011). Variations in $SLA_{EOS}$ are incomparable to variations in ELA and total mass balance where they do not account for all accumulation and ablation processes in play, and incomparable to surface mass balance where they do not account for all surface accumulation and ablation processes in play (Cogley et al., 2011).

Lake and marine terminating glaciers (e.g., of the Antarctic Peninsula and Southern Andes) are subjected to considerable mass losses via frontal ablation, in the form of calving and submarine melt. For example, Bown et al. (2019) claimed that the recent response of Jorge Montt Glacier, Patagonia, from 2012-2017 was characterised by frontal retreat processes, after determining a significant contrast in surface mass balance (-4.15 $km^3$ w.e. $a^{-1}$) and total mass balance (-17.79 $km^3$ w.e. $a^{-1}$) rates, where the latter incorporates losses from calving. Schaefer et al. (2015) has also inferred the strong impact of calving fluxes relative to surface melt in Southern Patagonia, by differencing surface and geodetic mass balances. Similarly, a surface mass balance estimate for Livingston Island, Antarctic Peninsula, from 2007-2011 (0.06 m w.e. $a^{-1}$) showed a different trend to the total mass balance estimate (-0.67 m w.e. $a^{-1}$), emphasising the dominance of frontal ablation in tidewater glacier mass balance (Osmanoğlu et al., 2014). As Antarctic Peninsula glaciers commonly have floating or partially floating tongues, the impact of basal melt is prevalent here and comparable to net mass losses due to calving (Liu et al., 2015). As snowlines may extend to sea level along the high-precipitation maritime western Peninsula (Davies et al., 2012), these frontal and basal ablation processes could be directly responsible for SLA variations. Basal melt may also be induced by percolating surface meltwater or rainfall, geothermal heat, and frictional heat, as found for the high-precipitation temperate Southern Alps (Alexander et al., 2011). Frontal, basal, and internal mass losses are neglected in surface observations of snowline and surface mass balance (Cogley et al., 2011), weakening the relationship of total mass balance, ELA and $SLA_{EOS}$.

Previous studies have also highlighted the inequality of $SLA_{EOS}$ and ELA estimates in regions where there is superimposed ice (caused by freeze-thaw cycles and freezing of rain on the glacier surface), and where basal and internal accumulation occurs via freezing of percolated rain or meltwater (Cogley et al., 2011; Rabatel et al., 2012). In the maritime Antarctic Peninsula where temperatures fluctuate around 0˚C, the polar climate has encouraged refreezing, which had an overall mass retention effect and caused glacier ELA to be located below the observable snowline (Lliboutry, 1998; Rabatel et al., 2012; Van Pelt et al., 2016; van Wessem et al., 2016). Opportunity for superimposed ice is typically considered minimal in mild temperate regions such as Patagonia (Schaefer et al., 2015) and the Southern Alps (Chinn, 1995); however, Abram et al. (2023) has estimated that 10% of meltwater gets refrozen at

Brewster Glacier, New Zealand. Superficial refreezing is accounted for in surface mass balance but not $SLA_{EOS}$, causing disparity; basal and internal refreezing is not accounted for by either parameter (Cogley et al., 2011).

Disparity between the glacier ELA, mass balance and $SLA_{EOS}$ has also arisen in regions where accumulation is largely driven by avalanching snow. Benn and Lehmkuhl (2000) stated that for Ama Dablam Glacier, Nepal, ELA was located at the foot of large avalanche cones at the glacier head, but noted that this altitude differed strongly to SLA. The comparability of ELA and surface mass balance with $SLA_{EOS}$ was reduced because avalanche cones caused the distribution of glacier accumulation to be dependent on avalanche volume rather than avalanche altitude, and a similar result may be plausible across all temperate high-mountain glacier environments (Benn and Lehmkuhl, 2000). Purdie et al. (2021) estimated a significant relationship of annual mass balance and $SLA_{EOS}$ at Rolleston Glacier, New Zealand ($r^2$=0.89), with disparity partly attributed to accumulation by snow avalanche.

Similarly, the relationship of surface mass balance and $SLA_{EOS}$ is weakened where snow drift redistributes mass between glaciers and sublimation contributes mass losses. These processes can be regarded in surface mass balance (e.g., Fyffe et al., 2021; Gallée et al., 2001; Gurgiser et al., 2013), but not in snowline observation alone (e.g., Tawde et al., 2016; Veettil et al., 2016b). Neglect of these processes can result in accumulation (ablation) overestimation (underestimation) (Ayala et al., 2016; MacDonald et al., 2010) for a given period of analysis, during which the visible snowline may not vary.

Previous works have shown that the use of $SLA_{EOS}$ as a proxy for ELA is also limited by the effect of precipitation seasonality and phase on surface mass balance. For instance, Sicart et al. (2011) demonstrated for Zongo Glacier, Bolivia, that contrasting wet and dry seasons, accompanied by limited temperature seasonality, lead to distinct accumulation and ablation seasonality with recurrent snow cover changes throughout the ablation period. These dynamics were also identified during the wet season for three glacier sites in Peru (Fyffe et al., 2021). Rabatel et al. (2012) suggested that dry season SLA can better indicate ELA in these conditions and found a significant relationship of dry season SLA and annual mass balance at Zongo Glacier ($r^2$=0.84) for 1996-2006; but accumulation totals can be higher in the relatively cooler dry season (Fyffe et al., 2021), and where SLA is estimated following a dry season snowfall event, the indicated ELA is underestimated (e.g., Rabatel et al., 2012; Schaefer et al., 2015). A similar issue has arisen for high-precipitation maritime glaciers of the Antarctic Peninsula and, to a lesser extent, the Southern Alps, where snowfall can occur over the summer period causing disparity in $SLA_{EOS}$ and ELA (e.g., Jiang et al., 2023; Porhemmat et al., 2021).

### 2.6. Research questions

With the aim to quantify trends of regional $SLA_{EOS}$ change across the entire glacierized Southern Hemisphere, the key questions that this research will address are:

1) What were the $SLA_{EOS}$ values of individual Southern Hemisphere glaciers up to the year 2020, as identified by an automated approach?
2) How does $SLA_{EOS}$ vary spatially and temporally within regions of the Southern Hemisphere?
3) What associations exist between $SLA_{EOS}$ variation and climatic variation within regions of the Southern Hemisphere?

# 3. Methodology

## 3.1. Study regions

This study focused on the three distinct glacierized regions of the Southern Hemisphere – the Southern Alps, Andes, and Antarctic Peninsula (Figure 3). These regions serve as important study sites, as (a) they lack SLA trend data gathered by an internally consistent approach; (b) they are each experiencing recent and rapid changes in warming and precipitation (González-Herrero et al., 2022; Hock et al., 2019) under the influence of modes of climatic variability, such as the El Niño Southern Oscillation (ENSO) (Masiokas et al., 2020; Purdie et al., 2011; Schneider et al., 2012) and Southern Annular Mode (SAM) (Fogt and Marshall, 2020; Lim et al., 2016); and (c) much of their high elevation area is sparsely covered with weather stations, limiting current understanding of regional climate change. These sites are therefore jointly useful in constraining Southern Hemisphere glacier-climate relationships.

The six regions studied covered a range of climate zones – tropical, sub-tropical, temperate, sub-polar and polar (Alisov, 1954) – with each region's climate additionally influenced by the degree of continentality, mountain elevation range, and latitude. In tropical climates (Tropical Andes and Central Andes here; Figure 3), seasons are driven by precipitation differences (opposite seasonality to that of sub-tropical and temperate zones) and there is little seasonal variation in warm temperatures (Vuille et al., 2008). With increasing latitude toward the sub-tropical zone (Central Chilean Andes here; Figure 3), temperature seasonality is more pronounced (lower in austral winter) and annual precipitation is notably less than at the low and high latitudes (Sagredo and Lowell, 2012). Temperate zones (Southern Alps and Southern Andes here; Figure 3) are warmer and wetter overall but experience distinct seasonality, with drier and warmer austral summers and wetter and cooler austral winters (Sagredo and Lowell, 2012); the seasonality minimises towards maritime temperate regions (Anderson and Mackintosh, 2012). The sub-polar (sub-antarctic) climate parallels the temperate maritime climate with limited seasonality of intense precipitation and humidity, but differs by colder and unvarying temperatures; it encompasses the Southernmost Andes (Tierra del Fuego) and the northern Antarctic Peninsula (Selkirk, 2007). The highest latitudes of the Antarctic Peninsula host a polar climate, with distinctly colder temperatures and lower precipitation quantities; however, an orographic influence on both sub-polar and polar zones of the Antarctic Peninsula creates highly continental (cold and dry) conditions in the east and highly maritime (warm and wet) conditions to the west (Davies et al., 2012). The climatic and geographic factors discussed influence the controls on glacier mass balance and, in turn, the degree to which snowlines reflect mass balance; the regional controls are discussed below.

### *3.1.1. Southern Alps*

On the geographically-isolated New Zealand South Island, the Southern Alps extend southwest along a 650 km transect from the warmer north (43˚S, 171.5˚E) to the cooler south (45˚S, 167.5˚E) (Figure 3).

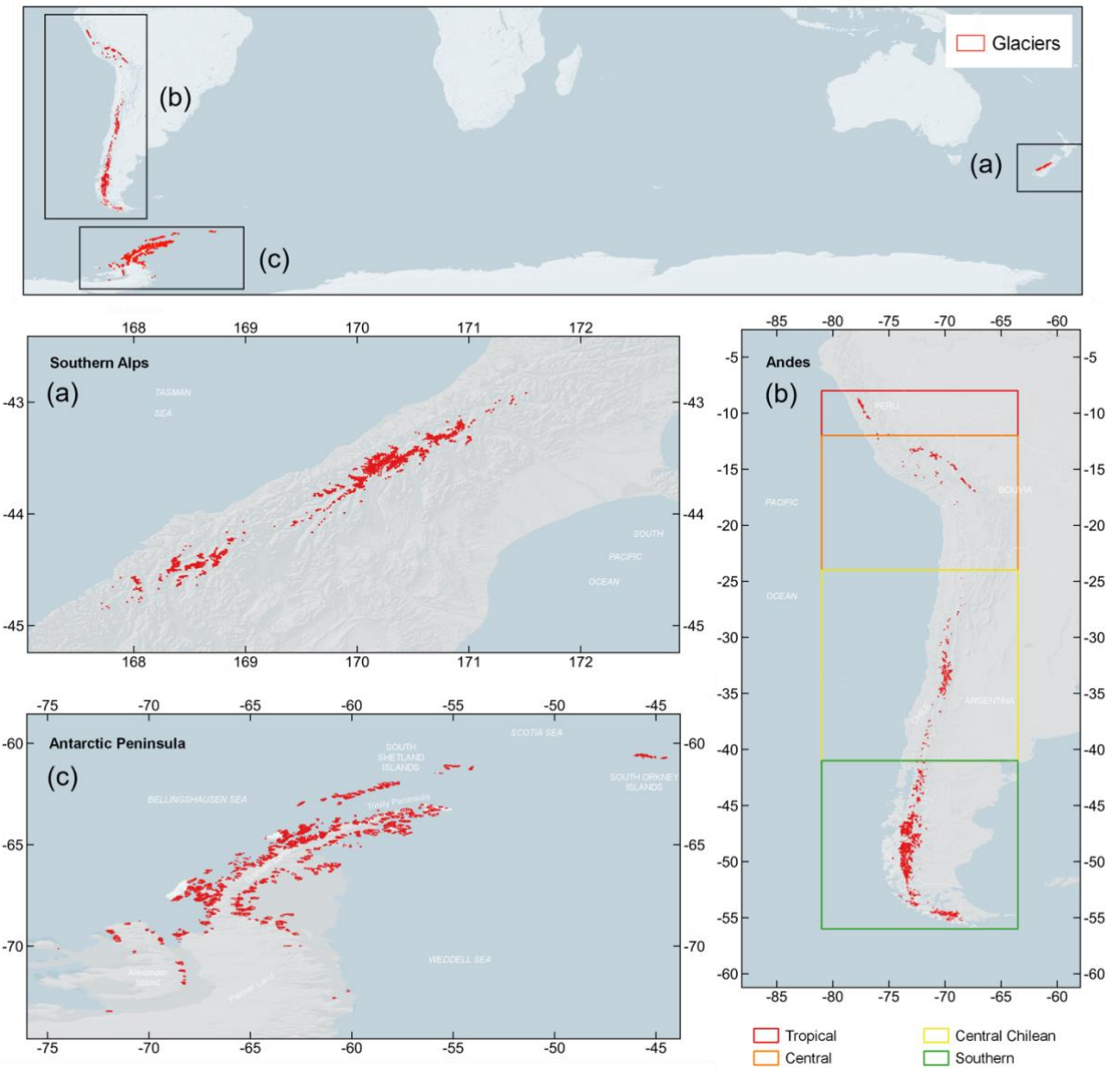


**Figure 3.** Locations of Southern Hemisphere study regions (top) and distribution of studied glaciers (red) in each region. (a) Southern Alps, New Zealand; (b) Andes, South America – covers large latitudinal range so divided into four study regions based on climatic zones (see *3.1.2.*); (c) Antarctic Peninsula.

The maritime setting means high quantities of precipitation are delivered from Southern Hemisphere westerlies over the Tasman Sea (Fitzharris et al., 1999); but distribution of precipitation has a strong east-west gradient due to the mountainous barrier of the Main Divide, separating the humid west (>6000 mm $yr^{-1}$) from the drier east (600-1500 mm $yr^{-1}$) (Ummenhofer and England, 2007). However, compared to other study regions, snowfall and air temperature variability is minimal across the Southern Alps, indicating the regional maritime climate (Appendix A, Figures A1 and A2). The strong summer shortwave radiation and steadily distributed precipitation through the year make for highly sensitive and active glacier systems (Fitzharris et al., 1999; Meier, 1961), which vary from steep to shallow

terrain (Anderson and Mackintosh, 2012) and reach maximum elevation in the Mount Cook region (~3700 m a.s.l.; 43.6˚S).

Warm temperate maritime conditions of the Southern Alps allow mass balance to be dominated by surface melt occurring through the year, with ablation period reducing as continentality increases eastward (Anderson and Mackintosh, 2012). Surface mass balance is also dependent on temperatures for partitioning of precipitation into rain or snow (Anderson and Macintosh, 2012). Under these warm conditions, it may be assumed that surface meltwater produced, or rain supplied, will retain its liquid phase (Clare et al., 2002; cf. Schaefer et al., 2015), minimising opportunity for superimposed ice and improving comparability of $SLA_{EOS}$ and mass balance toward the increasingly maritime west. However, internal freezing of meltwater is still possible in this region (Abram et al., 2023); the percolation of run off and subsequent changes to mass balance via internal or basal ablation and accumulation are not captured by the $SLA_{EOS}$. Similarly to in other mountainous maritime environments, Southern Alps mass balance is also controlled by wind-driven snow redistribution (Purdie et al., 2011) and snow avalanching (Purdie et al., 2021); if these controls alter accumulation volume but not accumulation area, they will be reflected in the surface mass balance but not in snowlines.

*3.1.2. Andes*

The Andes are situated on the western flank of South America, extending ~7000 km from 10˚N to 55˚S down a gradient of lowering relief. Due to this wide latitudinal range, and subsequently distinct climates across the north-south bearing (Appendix A, Figures A1 and A2), this study divides the south-of-equator Andes into four study regions (Figure 3 and Table 2), based on interpretations of climatic zones in the literature. From 8-12˚S, conditions are tropical, with elevated precipitation and temperature, and high-altitude terrain (~4000 m a.s.l.) which subjects glaciers to strong radiative forcing (Chevallier et al., 2011). The Central region, 12-24˚S, is an outer-tropical zone with reduced precipitation (Condom et al., 2007); here, eastern slopes are characterised by humid and warm conditions relative to western slopes (Garreaud, 2009). The Central Chilean region, 24-41˚S, has a semi-arid climate with particularly dry summers; higher quantities of precipitation on western slopes cause dry conditions to dominate the lee eastern slopes (Garreaud, 2009). The Southern region, 41-56˚S, is characterized by reduced mean elevation (~1500 m a.s.l.) and intense precipitation (~6000 mm $yr^{-1}$) governed by strong westerlies (Garreaud, 2009). Due to many existing Andean snowline studies having local-scale focus, this study also looks comparatively at a number of cordilleras and icefields within these four regions; namely, Northern Patagonian Icefield (NPI), Southern Patagonian Icefield (SPI), Cordillera Darwin, Cordillera Vilcanota, and Cordillera Blanca (Appendix B, Table A1).

In the Tropical Andes and Central Andes study regions (both tropical climate zone), mass balance is controlled by the phase and dynamics of wet season precipitation, via influence on albedo and convective cloud cover (determining short and longwave radiation budget) (Fyffe et al., 2021; Mutz

and Aschauer, 2022; Sicart et al., 2016). Temperature variations are tangentially important for determining precipitation phase and sublimation elevation (Fyffe et al., 2021); but the sublimation quantity is primarily steered by humidity (increased sublimation in dry conditions) (Kaser et al., 1990) making it the dominant ablation process in drier outer-tropical regions of southern Bolivia (Kaser, 2001; Stichler et al., 2001). As ablation via sublimation bypasses the ice phase, the mass loss can go unnoticed in $SLA_{EOS}$ observation; however, the degree to which sublimation distorts snowlines' reflection of surface mass balance in these regions varies altitudinally (more sublimation, thus uncertainty, with elevation) and spatially (more sublimation, thus uncertainty, towards sub-tropics). The extent to which $SLA_{EOS}$ reflects surface mass balance is also limited in these regions by the coincidence of glacier accumulation and ablation in the wet season (Rabatel et al., 2012), with opportunity for summer snowfall to produce underestimated $SLA_{EOS}$.

In the Central Chilean Andes, mass balance is primarily controlled by precipitation (Masiokas et al., 2016; Mutz and Aschauer, 2022; Rabatel et al., 2011) due to relatively cool and dry sub-tropical conditions (Sagredo and Lowell, 2012). The seasonality of precipitation minimises opportunity for summer snowfall to reduce $SLA_{EOS}$ validity, though low temperatures make for potential year-round precipitation at higher altitudes, and these conditions (combined with low humidity) make sublimation the dominant ablation process from 26-32˚S (Ayala et al., 2023). Mass balance is also influenced by surface melt in summer, which refreezes over cold nights to form superimposed ice (Rabatel et al., 2011), and by snow avalanching in steep high-altitude terrain (Vergara et al., 2020), which localises accumulation volume. These processes introduce additional discrepancy between snowlines and surface mass balance as the volume of mass retained/gained is not accounted for in $SLA_{EOS}$.

In the Southern Andes, the temperate climate of the mid-latitudes (i.e., Patagonia) can make for reasonable comparability of glacier snowlines and mass balance (cf. Lliboutry, 1965), as warmer temperatures encourage surface melt (especially in maritime west) which is assumed to not refreeze (Schaefer et al., 2015). However, most of these glaciers terminate in lake or marine calving environments (Bravo et al., 2021) and mass balance is largely driven by this frontal ablation, including submarine melt (Bown et al., 2019). These mass losses are unaccounted for in both $SLA_{EOS}$ observation and surface mass balance. Discrepancy between Southern Andes snowlines and surface mass balance is introduced by wind-driven snow redistribution between glaciers (Martin et al., 2022; Schaefer et al., 2015), and snow avalanching (e.g., Casteller et al., 2011); each process alters a given glacier's accumulation volume but not accumulation area, thus is considered in surface mass balance but not in $SLA_{EOS}$.

*3.1.3. Antarctic Peninsula*

The Antarctic Peninsula separates the Bellingshausen and Weddell Seas by a string of glaciers from 60-73˚S (Figure 3). Mountainous terrain increases rapidly in elevation, from sea level at the coastline to

1500-3000 m a.s.l. along inland plateaus (Dong et al., 2021). Plateaus are a barrier to atmospheric circulation and cause saturated air masses travelling east to deposit higher quantities of precipitation in the Bellingshausen Sea region (Silva et al., 2020). An east-west precipitation gradient is therefore highly evident for the Antarctic Peninsula compared to in other study regions (Appendix A, Figure A2). Increased temperatures in the west and in the far-north Trinity Peninsula add to this climatic gradient, forming a polar continental climate in the east and polar maritime climate in the west (Davies et al., 2012). Most glaciers are low-lying and marine-terminating, but with many catchments connecting to the high-altitude snow-covered plateaus (Dong et al., 2021). Glaciers on islands adjacent to the peninsula (such as James Ross or Anvers), and further afield (South Shetland and South Orkney), were also included in this study (Figure 3), to extend the SLA records spatially, and to allow for comparison among regions.

Mass balance of glaciers in the Antarctic Peninsula is largely controlled by wind-driven snow delivery and redistribution, frontal ablation of common marine-terminating glaciers, and sublimation (Engel et al., 2018; Liu et al., 2015; Navarro et al., 2013; van Lipzig et al., 2004). Ablation via surface melt is limited due to low temperatures of the polar climate zone, particularly in the east (Engel et al., 2018); however, run off is locally important on some ice shelves and the north-western region, where it is likely to refreeze (van Wessem et al., 2016) as maritime temperatures fluctuate around 0˚C (Engel et al., 2018). Mass losses due to frontal ablation and mass retention due to refreezing are not reflected in the snowline or surface mass balance. However, with the low-lying nature of many western glacier snowlines (Davies et al., 2012), there is opportunity for snowline variations to be directly altered by frontal ablation and accumulation processes. Mass losses due to sublimation and mass losses/gains due to snow drift are reflected in surface mass balance but may not be reflected in the snowline.

*3.1.4. Test glaciers*

Initial analysis was conducted on Southern Alps glaciers used in the New Zealand end-of-summer snowline survey (Chinn et al., 1995; Lorrey et al., 2022), so that results obtained here could be compared to a consistent existing database, and method adjustments could be evaluated efficiently before application over larger spatial scales. Test glaciers (Appendix B, Table A2) were selected from the survey index list based on availability of recent outline data.

**Table 2.** Geometries used to define Andes study regions.

| Region | Latitude range | Longitude range |
|---|---|---|
| Tropical Andes | 8-12˚S | 63-81˚W |
| Central Andes | 12-24˚S | 63-81˚W |
| Central Chilean Andes | 24-41˚S | 63-81˚W |
| Southern Andes | 41-56˚S | 63-81˚W |

## 3.2. Data sources

A variety of raster and vector datasets were used in automated calculation of $SLA_{EOS}$ and in subsequent analysis and interpretation of results; these are summarised in Table 3.

**Table 3.** Outline of datasets used in this study.

| Data description | Source | Data type | Spatial resolution (m) | Temporal resolution (days) | Reference |
|---|---|---|---|---|---|
| Glacier outlines | Global Land Ice Measurements from Space (GLIMS) | Vector | 30 * | - | GLIMS and NSIDC (2005, updated 2013) |
| Satellite imagery | U.S. Geological Survey (USGS) Landsat surface reflectance | Raster | 30 | 16 | - |
| Elevation | JAXA ALOS World 3D Digital Surface Model (DSM) | Raster | 30 | - | Tadono et al. (2016) |
| Meteorological | ERA5-Land Monthly Aggregated | Raster | 11,132 | 30 ** | Muñoz-Sabater (2019) |
| Drainage basins | World Wildlife Fund (WWF) HydroSHEDS basins | Vector | 500 *** | - | Lehner and Grill (2013) |
| Drainage basins | NASA Goddard Ice Altimetry Group | Vector | 500 *** | - | Zwally et al. (2012) |

*Assuming outlines digitised from 30 m satellite imagery. May not be applicable to all outlines.
**Approximation of monthly temporal resolution.
***Basins digitised from ~500 m raster data.

### *3.2.1. Glacier outlines*

It is critical for this study that outlines correctly delimit glacier extent; accuracy of binary image segmentation is limited when outlines encompass land that is not snow or ice covered, subsequently

limiting accuracy of the calculated snow cover ratio (SCR) and SLA. Outlines can be manually digitised to reduce error, as in Li et al. (2022); however, the spatial scale of this study makes individual adjustments like this unfeasible. Global Land Ice Measurements from Space (GLIMS) provides a comprehensive database of glacier outlines for all three study regions (GLIMS and NSIDC, 2005, updated 2013), with updated outline geometries available compared to the Randolph Glacier Inventory database used in Loibl et al. (2022) and Liu et al. (2021), allowing for an accurate delineation of modern-day glacier snow and ice areas.

GLIMS outline data were downloaded for the regions and prepared in QGIS by removing features not labelled as glacier boundaries, fixing remaining feature geometries, removing duplicate geometries, and removing features with pre-1980 source imagery dates. This process ensured remaining outline data were not erroneous or outdated. Google Earth Engine (GEE) was used to retrieve the most recent outline feature for a given glacier, iterating over a list of glacier GLIMS IDs. In some cases, the GLIMS dataset attributed erroneously small polygons to some glacier IDs; when these features were selected, the largest outline associated with glacier IDs was taken instead. Retrieved features formed new outline shapefiles for each region, which were filtered to select features with manageable areal extent. To reduce the runtime, glaciers with area 1-100 $km^2$ were selected for the Andes and Antarctic Peninsula, while glaciers 0.1-100 $km^2$ were selected for the Southern Alps (Table 4); these thresholds were selected due to, (a) higher relative frequency of smaller glaciers in the Southern Alps, and (b) the comparative New Zealand aerial survey studying multiple index glaciers < 1 $km^2$.

**Table 4.** Description of glacier outlines selected for analysis following filtering process. Total glaciers processed was 6580.

| Region | Area range ($km^2$) | n |
|---|---|---|
| Southern Alps | 0.1-100 | 636 |
| Antarctic Peninsula | 1-100 | 1641 |
| Tropical Andes | 1-100 | 136 |
| Central Andes | 1-100 | 457 |
| Central Chilean Andes | 1-100 | 572 |
| Southern Andes | 1-100 | 3138 |

*3.2.2. Satellite imagery*

Atmospherically corrected surface reflectance products from Landsat 4 TM, Landsat 5 TM, Landsat 7 ETM+, and Landsat 8 OLI were retrieved from the USGS via GEE. Landsat provides optimal

combination of wide temporal coverage (images from 1983), high spatial resolution (30 m), and reasonable image acquisition intervals (16 days), hence its use in most automated snowline analyses (Li et al., 2022; Liu et al., 2021; Racoviteanu et al., 2019; Rastner et al., 2019). Previous work has suggested that top-of-atmosphere products may be preferential for use over the Antarctic Peninsula because of the uncertainty associated with deriving robust surface reflectance for polar regions (Chen and Zhu, 2022), but to ensure internal consistency, surface reflectance was used throughout the study in line with previous automated snowline analyses (Li et al., 2022; Wang et al., 2023). Tier 1 products, with enhanced positional quality (Young et al., 2017), were obtained where possible; however, as these do not exist for the Antarctic Peninsula, Tier 2 products were used here.

*3.2.3. Elevation data*

A digital elevation model (DEM) was required to build glacier contour grids and extract altitude measurements. ALOS World 3D 30 m (AW3D30; Tadono et al., 2016) digital surface model (DSM) contains an elevation band with 30 m horizontal resolution. This DEM was imported in GEE, clipped to the given study region extent, and mosaicked to form a single-band raster. AW3D30 (version 3.2) has previously been used in automated snowline detection (Loibl et al., 2022), and is favoured over NASADEM (used in Li et al. (2022)) and Shuttle Radar Topography Mission (used in Racoviteanu et al. (2019) and Rastner et al. (2019)), due to its higher vertical accuracy (~5 m; Takaku et al. (2014)) and lower root mean square error (RMSE) (Bettiol et al., 2021; Mukul et al., 2017; Uuemaa et al., 2020).

*3.2.4. Meteorological data*

Investigations into relationships of $SLA_{EOS}$ with temperature and snowfall trends across the regions required meteorological data provided by ERA5-Land monthly aggregates (Muñoz-Sabater, 2019). Although this reanalysis dataset incorporates modelled data with observations and has relatively coarse spatial resolution (~11 km), its global coverage allows for consistency across study regions, which is less easily achieved with ground-based meteorological data from multiple sparsely located sources. In GEE, monthly snowfall and mean 2 m air temperature were averaged for (a) the Southern Hemisphere summer of a given year (December-March), and (b) the area over a given glacier. Gradient of change in climatic averages were calculated, for comparison to regional $SLA_{EOS}$ trends.

*3.2.5. Drainage basin data*

As addressed in *3.1.*, region-wide spatial variations in climate are thought to exist across each region, commonly exhibited in contrasting climates east and west of the region (Davies et al., 2012; Garreaud, 2009; Ummenhofer and England, 2007). Association of this climatic variation with glaciological variation was investigated by comparing the $SLA_{EOS}$ trends for east-draining and west-draining glaciers. This required drainage basin vector data, retrieved from the Level 5 WWF HydroSHEDS dataset (Lehner and Grill, 2013) in GEE for the Southern Alps and Andes, and from the NASA Goddard Ice

Altimetry Group dataset (Zwally et al., 2012) for the Antarctic Peninsula. Figure 4 illustrates the designation of 'east' and 'west' sub-regions using these datasets, and the centroid location of studied glaciers within sub-regions.

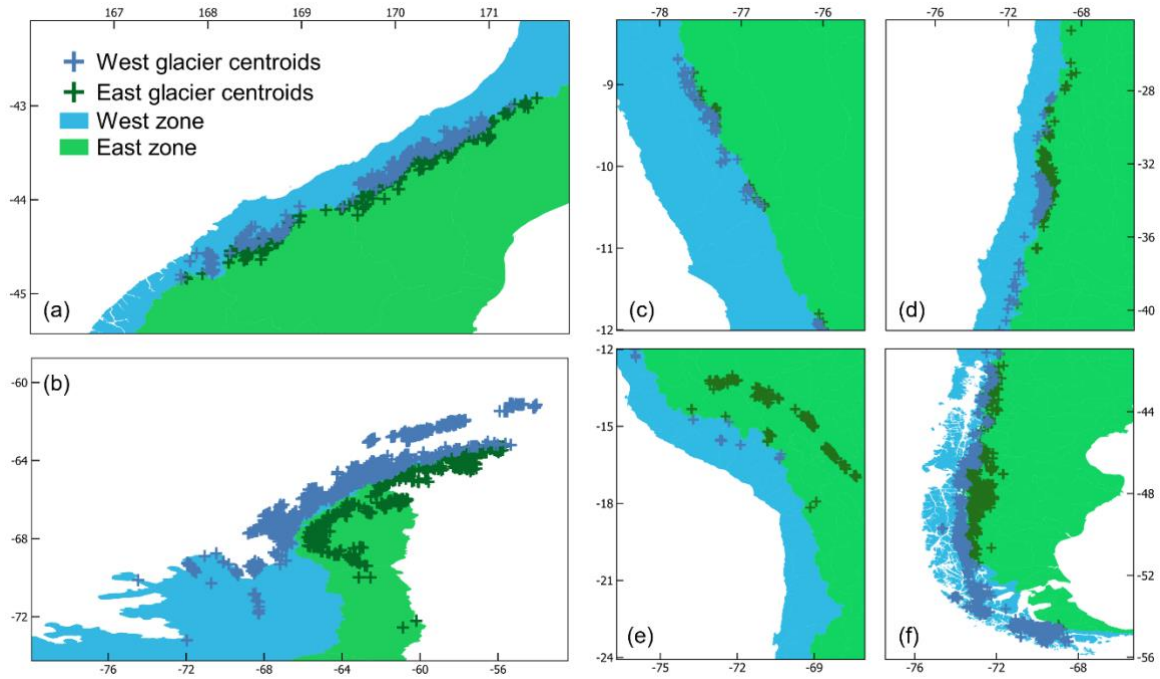


**Figure 4.** 'East' and 'west' sub-regions and glaciers, derived from drainage basins, for the investigation of spatial variation in $SLA_{EOS}$ and climate. (a) Southern Alps; (b) Antarctic Peninsula; (c) Tropical Andes; (d) Central Andes; (e) Central Chilean Andes; (f) Southern Andes.

### 3.3. GEE snowline analysis

GEE was the most appropriate cloud-based platform for efficient monitoring of glacier $SLA_{EOS}$ over this study's vast spatial and temporal extent. Of the previous studies which have used GEE in automated snowline detection (Li et al., 2022; Liu et al., 2021; Loibl et al., 2022; Wang et al., 2023), the workflow of Li et al. (2022) was deemed most suitable to be adapted for this study. In Li et al. (2022), the workflow retrieved monthly SLA across a sequence of years for a singular glacier. This study expanded the workflow to retrieve $SLA_{EOS}$ values across a sequence of years for multiple glaciers simultaneously (Figure 5). Following data preparation, the method involves two core processing steps – snow classification and $SLA_{EOS}$ identification – which are iterated across a list of years and list of glaciers. To avoid exhausting the GEE processing capacities, lists of glacier outlines to be iterated over in a single run were divided, so that each run analysed an aggregated area of < 150 $km^2$.

*3.3.1. Image and elevation data processing*

In GEE, Landsat collections were filtered to (a) the period 1983-2020, mirroring the date range of published aerial survey data from the point Landsat imagery became available (Lorrey et al., 2022), and (b) the end-of-summer timeframe for each region. For the Andes and Southern Alps, previous studies support the timeframe of mid-February to early-April (Abrahim et al., 2023; Mernild et al., 2016; Rivera

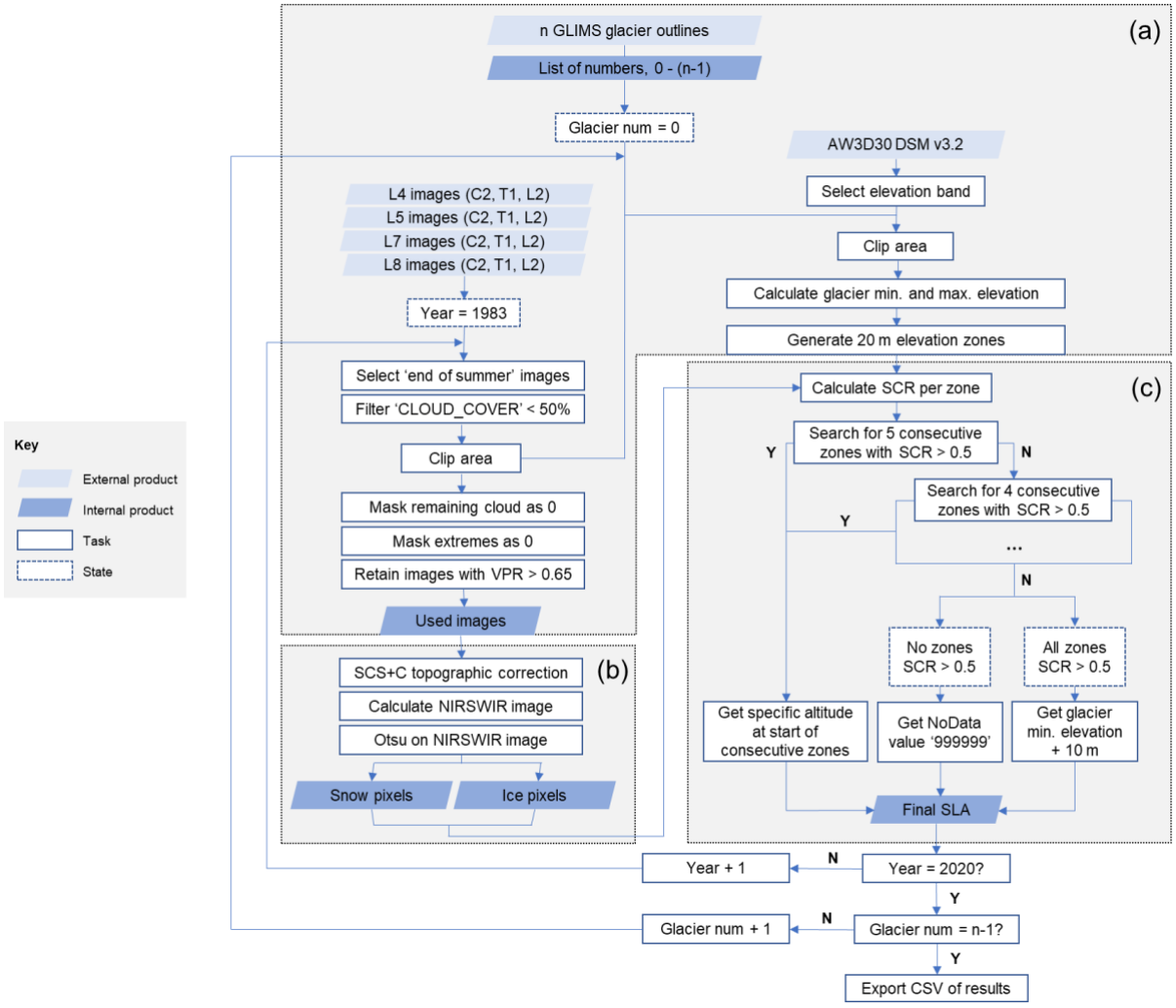


**Figure 5.** Processing scheme for $SLA_{EOS}$ retrieval in GEE, adapted from Li et al. (2022) to analyse multiple glaciers simultaneously. (a) Image and elevation data processing; (b) snow classification; (c) $SLA_{EOS}$ identification.

and Casassa, 1999; Willis et al., 2012). For the Antarctic Peninsula, end-of-summer can be earlier, with annual peak Antarctic snow melt having previously been documented in January (Zwally and Fiegles, 1994). Timeframes used here were 01/02 – 30/04 for the Andes and Southern Alps, and 01/01 – 30/04 for the Antarctic Peninsula, allowing for fluctuations in the timing of maximum SLA between years.

By filtering the Landsat metadata attribute 'CLOUD_COVER', images with a cloud percentage > 50% were removed from analysis. Remaining images were clipped to the glacier outline and the C Function of Mask (CFMask) algorithm was applied to mask any cloud-covered pixels over the glacier area which could be visually mistaken for snow due to their similar reflectances (Crane and Anderson, 1984). As in Li et al. (2022), potential erroneous pixels with a value > 65535 were also masked. The valid pixel ratio (VPR) of every image for a given glacier was calculated, and only images with > 65% visible pixels remaining following cloud masking were retained for further analysis. The valid pixel threshold of 0.65 was chosen based on its successful use in Li et al. (2022). The effect of Landsat 7 scan line corrector error (Markham et al., 2004), which created tracks of invalid image pixels over some glaciers, was also minimised by this step.

Following preparation outlined in *3.2.3.*, the AW3D30 DEM was clipped to the given glacier outline. Functions were run to calculate the minimum and maximum elevation within this clipped extent, and to generate a list sequence of contour elevations between these values at 20 m intervals.

*3.3.2. Snow classification*

Glacier images in the filtered collection were individually processed to detect snow-covered regions. A given image was topographically corrected by sun-canopy-sensor correction (SCS+C; Soenen et al., 2005) using GEE-based code adapted from top-of-atmosphere topographic correction methods in Stringer (2022) and surface reflectance topographic correction methods in Poortinga et al. (2019). Topographic correction reduces underestimation of snow-covered pixels caused by topographic shadow (Jasrotia et al., 2022), and the SCS+C method is well-supported by previous studies, which encourage its use for mountainous environments (AL-Doski et al., 2020**;** Vázquez-Jiménez et al., 2017). Although part of image preparation, topographic correction took place at this stage to prevent time consumption associated with correcting entire image collections simultaneously.

As the use of different band ratios, NDSI and NIRSWIR, currently divides automated snowline analyses (e.g., Li et al., 2022; Wang et al., 2023), and no direct comparison of the two approaches is evident in previous research, this study calculated annual mean $SLA_{EOS}$ for the test glaciers using snow classifications on both NDSI and NIRSWIR images, and compared outputs to those collected by the New Zealand aerial survey for the same glacier sample (Lorrey et al., 2022). Results from the NIRSWIR approach showed a weak positive correlation with aerial survey results ($r$ = 0.19), while results from the NDSI approach showed moderate negative correlation ($r$ = -0.44; Figure 6). Although aerial survey data cannot be treated as ground-truth due to its multiple limitations, this study rejected use of NDSI based on these results. As Li et al. (2022) documents improved accuracy of the NIRSWIR method compared to the NIR method, the former was used to differentiate between snow and ice pixels in an image. The new NIRSWIR band was created for a given glacier image by applying Equation 1, which used bands 4 and 5 in Landsat 4 TM/5 TM/7 ETM+, and bands 5 and 6 in Landsat 8 OLI.

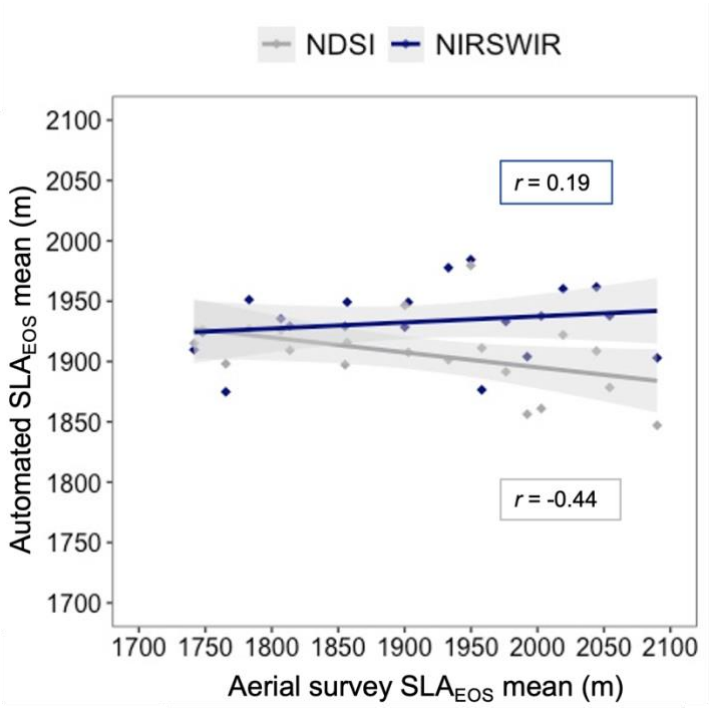


**Figure 6.** Automated annual mean $SLA_{EOS}$ of test glaciers (n=34) showed a non-significant moderate negative correlation (*r*=-0.44; p=0.053) to results collected by the New Zealand aerial survey (Lorrey et al., 2022) when NDSI image was used for snow classification, but non-significant weak positive correlation (*r*=0.19; p=0.43) to survey results when NIRSWIR image was used.

$$NIRSWIR = NIR \times \frac{NIR}{SWIR1} \quad (1)$$

Using a histogram of the new NIRSWIR band, the Otsu method of binary image segmentation (Otsu, 1979) was applied to classify the image into 'snow' and 'ice' pixels. This statistical algorithm identifies case-specific classification thresholds, by identifying the maximum between-class variance, corresponding to the maximum between-sum-of-squares (BSS) of pixel values in an image (Figure 7). Otsu has been applied in several automated snowline detection studies (Li et al., 2022; Liu et al., 2021; Rastner et al., 2019; Wang et al., 2023), as it is favoured over manual and semi-automated methods for adaptively identifying snow-ice boundaries over large glacier samples (Gaddam et al., 2022). This step assumes each glacier image contains only snow and ice pixels; however, if other light-absorbing land cover types (e.g., rock or vegetation) are contained in the glacier area, they will likely be classified as 'ice' and cause a shift in the Otsu threshold value (Liu et al., 2021). As indicated in *3.2.1.*, this study attempts to minimise this error by preferentially selecting the most updated glacier outlines.

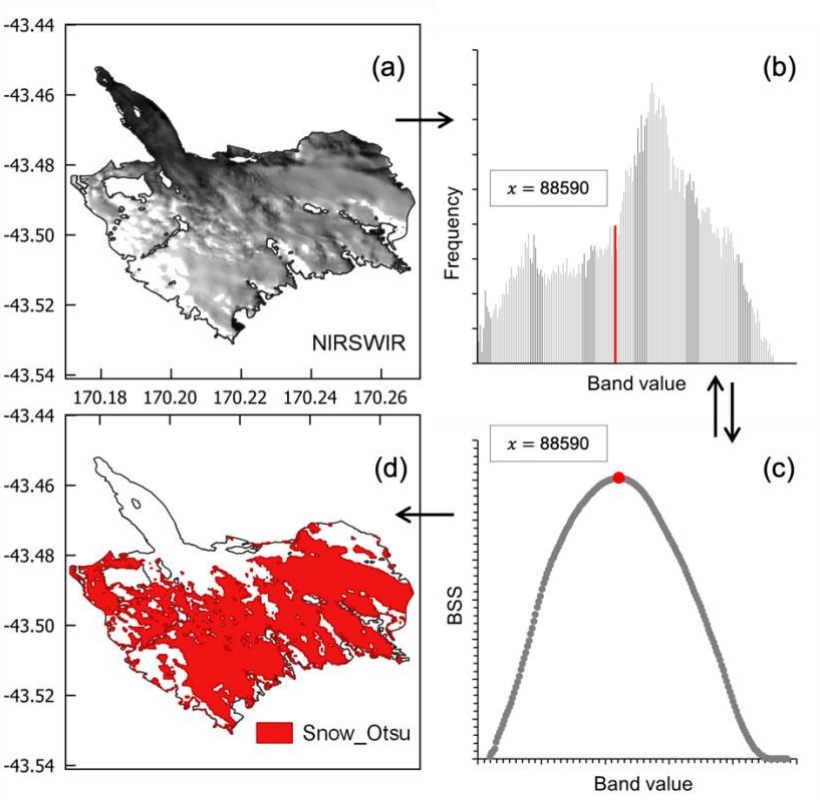


**Figure 7.** Framework of Otsu algorithm application to identify case-specific snow classification threshold. (a) NIRSWIR band image of Franz Josef Glacier; (b) histogram of NIRSWIR image showing threshold ($x$; red); (c) NIRSWIR value with maximum BSS ($x$; red) corresponds to threshold in (b); (d) NIRSWIR pixels exceeding threshold value classified as 'snow'.

### *3.3.3. $SLA_{EOS}$ identification*

Topographic and climatic factors can cause hollows, shadows, avalanche deposits and wind-blown snow to create perforated snow cover in the glacier snowline region, so that the snowline may be non-continuous and span a range of altitudes (Rastner et al., 2019). Consequently, the World Meteorological Organisation (WMO) recommended that $SLA_{EOS}$ be represented as an altitudinal zone rather than a specific altitude, where this zone is characterised by snow cover exceeding 50% of the zonal area (WMO, 1970). As in previous snowline detection methods (Li et al., 2022; Rastner et al., 2019), this study separated the classified glacier image into 20 m elevation bins using the list of contours created in data preparation, and the SCR of each bin was calculated from its 'snow' and 'ice' pixel counts (Equation 2).

$$SCR = \frac{snow\ pixels}{snow\ pixels + ice\ pixels} \quad (2)$$

A function was then applied to identify the lowermost set of 5 consecutive elevation bins which each had SCR > 0.5 (snow coverage > 50%). If a set is identified, $SLA_{EOS}$ is taken as the average elevation of the lowest bin in this set. If unidentified, the required number of bins in a set is reduced by 1, until the condition for SCR is met. If no elevation bin with SCR > 0.5 can be identified, $SLA_{EOS}$ is returned as a null value. In previous studies, this scenario returned $SLA_{EOS}$ as the maximum glacier elevation (Li et al., 2022); however, this was considered an assumption which could potentially lead to overestimations in the overall results, so was not applied here.

When there were multiple usable images for the given glacier in the given year, multiple $SLA_{EOS}$ results were produced. In this case, the non-null values for $SLA_{EOS}$ were filtered to identify the maximum and record this as the definitive result, as $SLA_{EOS}$ is defined as maximum altitude attained by the snowline in the ablation season. When only one $SLA_{EOS}$ result was produced for the given glacier and year, it was not recorded as the definitive result, because the maximum of a sample should not be calculated when the sample size is one. This meant every definitive $SLA_{EOS}$ result retrieved was maximum $SLA_{EOS}$ compared to at least one other $SLA_{EOS}$ result for that glacier and year.

An annotated copy of the GEE script used for snowline analysis is available at: https://code.earthengine.google.com/621c7b9048059ea0c5790bbaf062d617

### 3.4. Accuracy and uncertainty

#### *3.4.1. Snow classification accuracy*

The accuracy (*A*) of snow classifications resolved by Otsu was determined in each of the six regions by random point assessments. For each region, a cluster of glaciers with a range of aspects was selected, and *A* was assessed for two separate years. Images and classification vectors were taken from the date of each glacier's $SLA_{EOS}$ in that year, to ensure they were the data used in $SLA_{EOS}$ retrieval. This meant years being assessed varied between regions, as it depended on availability of an $SLA_{EOS}$ result for each glacier in the cluster. Across the imagery selected, it was ensured that Landsat 7 ETM+ and Landsat 8 OLI were both represented, allowing for accuracy comparisons between sensors. As illustrated in Figure 8, each assessment comprised 100 random validation points classified visually into snow, ice, and N/A (blank image) groups. This was facilitated by interpretation of false-colour images (bands 5, 4, and 3 for Landsat 5TM/ 7ETM+, and bands 6, 5, and 4 for Landsat 8 OLI), and consideration of the likely locations of accumulation and ablation zones. These interpretations were then compared to classifications determined by Otsu, to calculate percentage *A*.

The estimated mean accuracy ($A_{MEAN}$) of snow classification was 87.4 ± 6.2 % across all regions and years assessed. Although Landsat 7 ETM+ images increased the number of N/A validation points due to gaps associated with scan line error, $A_{MEAN}$ did not vary between cases where Landsat 7 ETM+ images

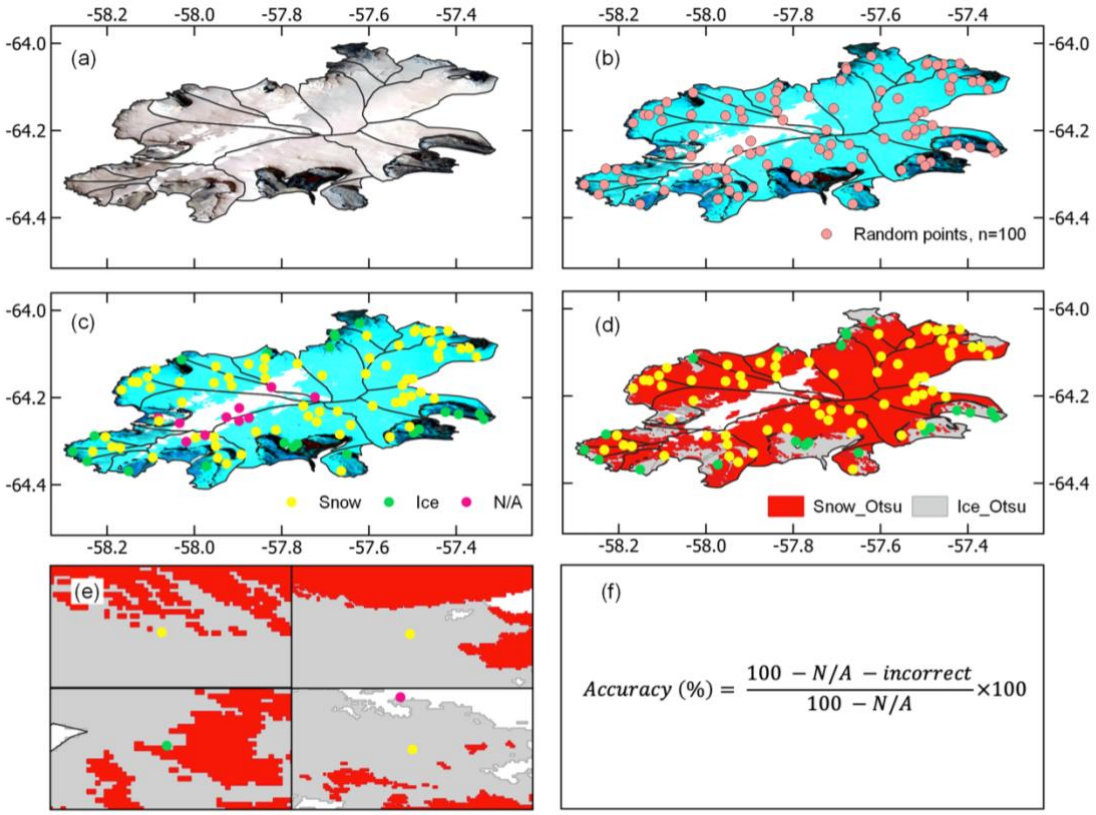


**Figure 8.** Framework of snow classification accuracy assessments using example from a region of James Ross Island, Antarctic Peninsula; (a) true-colour image from end-of-summer period of given year; (b) image converted to false-colour and 100 random sampling points overlaid; (c) using false-colour as guide, points designated into researcher's interpretation of snow, ice, and N/A groups; (d) Otsu 'snow' and 'ice' classifications overlaid; (e) examples of incorrect Otsu classifications to be counted; (f) calculation of percentage accuracy using counts of N/A and incorrectly classified points.

were present (87.5%) and cases where only Landsat 8 OLI images were present (87.2%). $A_{MEAN}$ varied more strongly between regions (Figure 9), particularly across the four Andean groups, with the Central Chilean and Tropical regions displaying highest (93.9%) and lowest (77.8%) snow classification $A_{MEAN}$, respectively. This outcome was expected due to regional differences in cloud cover frequency (Prudente et al., 2020) which made for increased image clarity in the Central Chilean region. On inspection, however, the lower *A* of Tropical region classifications was more so attributed to topographic shading. Shading lowered image saturation in snow covered regions and caused underestimation of snow classification, despite images being topographically corrected at earlier stages. This was a main cause of classification error in previous automated snow cover mapping (Loibl et al., 2022), and has caused misclassification in other regions assessed here; for example, plateau shadow regions of the Antarctic Peninsula (Figure 9b). However, this error should not affect accuracy of automated $SLA_{EOS}$ delineation if the shadow lies outside of the snowline zone.

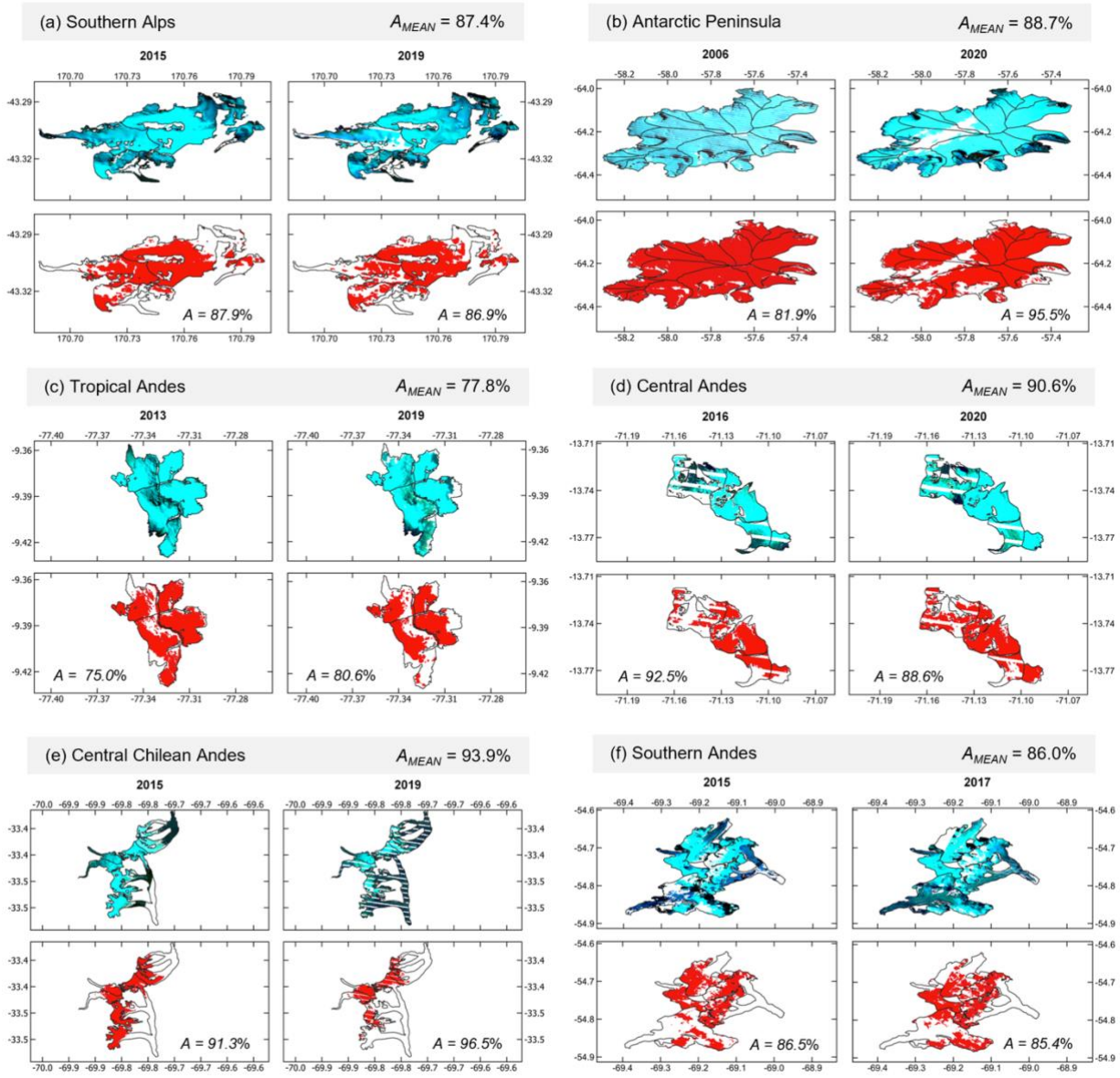


**Figure 9.** Inter-regional variation in mean accuracy ($A_{MEAN}$) of automated snow classification (red), displayed with false-colour composites of images segmented by Otsu algorithm. Images taken from end-of-summer dates of the given year. Accuracy assessment sites were within: (a) Garden of Allah, Southern Alps; (b) James Ross Island, Antarctic Peninsula; (c) Cordillera Blanca, Tropical Andes; (d) Cordillera Vilcanota, Central Andes; (e) Cordillera Principal/Frontal, Central Chilean Andes; (f) Cordillera Darwin, Southern Andes.

### *3.4.2. $SLA_{EOS}$ uncertainty*

Sources of uncertainty in the automated $SLA_{EOS}$ calculation are in accordance with those identified in similar studies (Li et al., 2022; Racoviteanu et al., 2019; Rastner et al., 2019). Uncertainty arises from: (a) vertical accuracy of elevation data, (b) accuracy of satellite images used in glacier outline generation and snowline analysis, and (c) accuracy of the $SLA_{EOS}$ identification method. As glacier outlines were

taken from the GLIMS database, multiple satellite datasets may have been used for outline digitisation; this uncertainty estimate assumes that Landsat images were used throughout, as per Raup et al. (2007) and Pfeffer et al. (2014). It could be reasoned that uncertainty also varies with glacier characteristics, such as slope angle at the snowline (Rabatel et al., 2012; Rastner et al., 2019); though slope is not considered an uncertainty source in several previous snowline studies (Li et al., 2022; Loibl et al., 2022; Racoviteanu et al., 2019) and assessment of uncertainty sources at the glacier scale is unfeasible given this study's hemispheric coverage.

As the uncertainty sources were assumed to be uncorrelated, $SLA_{EOS}$ uncertainty was calculated as RMSE using Equation 3. Terms of the calculation are defined as:

- $u_{DEM}$: vertical uncertainty of AW3D30 DEM. Takaku et al. (2014) states this is ± 5 m.
- $u_{image}$: uncertainty of Landsat satellite images, which Paul et al. (2013) considers as ½ pixel size (± 15 m).
- $u_{zone}$: uncertainty of the zonal method used for $SLA_{EOS}$ identification, where $SLA_{EOS}$ is taken as the average elevation of a 20 m bin and uncertainty is therefore ± 10 m (Li et al., 2022).

$$u_{SLA_{EOS}} = \pm\sqrt{(u_{DEM})^2 + (u_{image})^2 + (u_{zone})^2} \quad (3)$$

The estimated uncertainty in $SLA_{EOS}$ is therefore ± 18.7 m. This is an improvement on the uncertainty of SLA calculations in Li et al. (2022) (± 24 m); the difference mainly arises from the vertical accuracy of DEMs used in each study, with the NASADEM used in Li et al. (2022) comprising much greater uncertainty than AW3D30 (Bettiol et al., 2021).

### 3.5. Methodological limitations

Alongside uncertainty sources identified in *3.4.2.*, additional research limitations involved the quality of input data and the influence of glacier surface characteristics.

Due to the 16-day repeat cycle of Landsat sensors, the temporal resolution of satellite imagery used in this study is limited. This reduces available imagery for the end-of-summer period of a given year and reduces the likelihood that $SLA_{EOS}$ is calculated on the date of maximum altitude. Multiple Landsat sensors with overlapping coverage (e.g., 5 TM and 7 ETM+ overlap from 2000–2011; 7 ETM+ and 8

OLI overlap from 2013–2020) are employed to increase temporal resolution. The use of 20 m elevation zones in $SLA_{EOS}$ delineation also minimises the effect of not attaining maximum $SLA_{EOS}$, as the maximum snowline can vary up to 20 m in the period that lacks imagery before a new elevation bin is designated as $SLA_{EOS}$.

As glacier outlines could not be individually corrected for a study of this scale, there would have been disparities between the date (and therefore geometry) of the used glacier outline and the 'true' glacier outline in different image scenes. Where the used outlines are broader than 'true' outlines, alternative land covers such as vegetation and bedrock may be encompassed in the analysed area. As the Otsu algorithm is designed to segment between just two land covers (here, snow and ice), addition of land covers can distort the snow-ice threshold value, therefore altering the snow classification and $SLA_{EOS}$ calculation. This method used the most recent available GLIMS outline for each glacier to minimise inclusion of exposed land cover types.

Due to cloud masking and subsequent removal of images with VPR < 0.65, $SLA_{EOS}$ results for regions with higher cloud cover probability (Southern Andes, Tropical Andes and Antarctic Peninsula; Figure 10) are largely sparse. Additionally, there were even fewer results from 1993-2000, when image availability was poor because only Landsat 5 TM was operating. Sparse results lead to regional $SLA_{EOS}$ trends which may not be representative, as some annual $SLA_{EOS}$ means were calculated from particularly small sample sizes of results. A minimum sample requirement of 10 glaciers was set for any calculation of regional annual mean $SLA_{EOS}$, standard error (S.E.) bars were calculated to judge validity of $SLA_{EOS}$ means, and clear anomalies in $SLA_{EOS}$ mean were excluded from overall trends.

The CFMask algorithm used in cloud detection has inevitable difficulties over brighter surfaces, such as snow, and a tendency to overlook presence of optically thin clouds (Fog et al., 2017). Consequently, there was potential for undetected cloud cover to exist over glacier images, which may have been classified as ice due to low reflectance of cloud in the NIRSWIR band (Li et al., 2022). If cloud was present in an ablation zone, the effect on $SLA_{EOS}$ calculation would be negligible; however, in a minority of cases, where cloud was present in the accumulation zone, snow cover would be underestimated and $SLA_{EOS}$ overestimated. At glacier level examination, cloud presence could anyway be validated by its high reflectance in the SWIR band.

Finally, the presence of supraglacial debris and shadowing may have also limited the research strategy in some regions, as the typically darker areas would be classified as ice by Otsu. Where debris or shadowing exists in the ablation zone, its classification as ice will have made negligible difference to the snow classification and SLA calculation (Rastner et al., 2019). Darker surfaces existing in the accumulation zone will have instead caused underestimation of snow-covered area. Temporary ash debris cover visible in the snowline region of some Southern Alps glaciers, following the high-impact

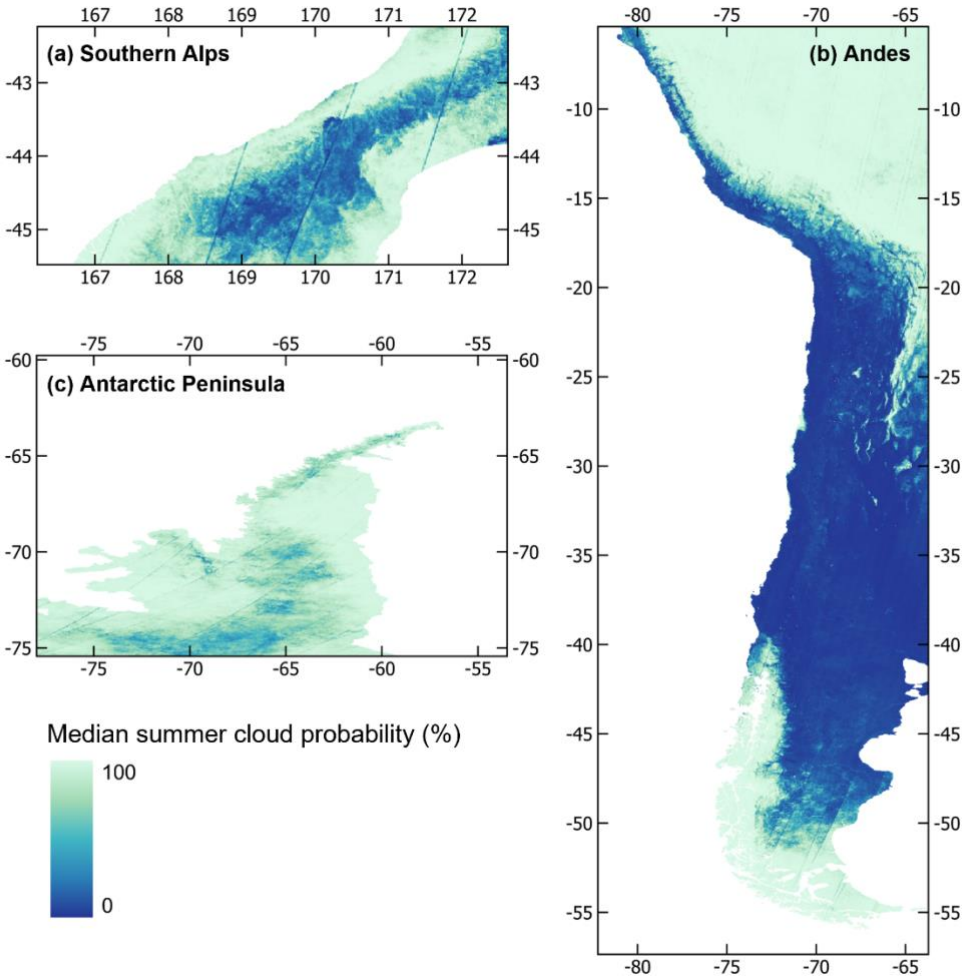


**Figure 10.** Median summer (December-March) cloud probability for the Southern Alps (a), Andes (b) and Antarctic Peninsula (c), derived from Sentinel-2 data (Copernicus Sentinel data, 2020).

bushfire event in the 2020 summer, caused snow cover underestimation and $SLA_{EOS}$ overestimation (Figure 11a), whilst shadowing arising from steep and complex accumulation area terrain caused snow cover underestimation but did not notably affect $SLA_{EOS}$ when shadowing was outside of the snowline zone (Figure 11b). The influence of darker surfaces was assumed to be negligible at hemispheric scale; for instance, debris-covered glaciers only comprise ~4% of global glacier area (Shukla et al., 2022), and the automated approach minimises the impact of anomalous pixels or images from the regionally averaged trends that are presented herein.

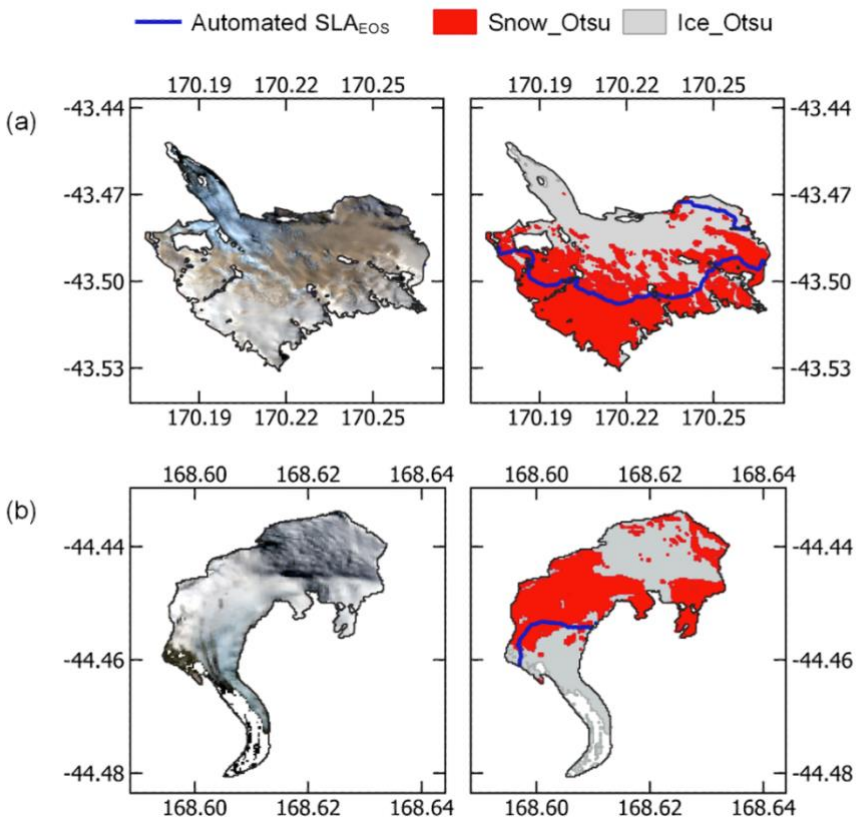


**Figure 11.** Examples of glacier image scenes (left) which are problematic for automated snow classification and $SLA_{EOS}$ delineation (right). (a) Temporary bushfire ash on Franz Josef Glacier, Southern Alps, causes $SLA_{EOS}$ overestimation; (b) topographic shading on upper Dart Glacier, Southern Alps, causes snow/ice misclassification.

# 4. Results

## 4.1. Coverage of $SLA_{EOS}$ results

Of the 6580 glaciers processed, 95 returned no $SLA_{EOS}$ results from 1983-2020. Table 5 describes the regional samples of glaciers following removal of glaciers with no $SLA_{EOS}$ results.

In each region, the number of glaciers for which $SLA_{EOS}$ results were retrieved was inter-annually variable during the period of 1983-2020 (Figure 12). No $SLA_{EOS}$ results were retrieved for the Southern Alps pre-2000 (Figure 12a), and the density of results was very low pre-2000 for the Antarctic Peninsula (Figure 12b) and Southern Andes (Figure 12f). Therefore, for consistency and to enable inter-regional comparisons, subsequent $SLA_{EOS}$ result analysis focuses on the 2000-2020 period. However, the raw $SLA_{EOS}$ results for pre-2000 are available in supplementary material for reference.

For the period of 2000-2020, the count of annual $SLA_{EOS}$ results retrieved per glacier varied spatially across the study regions (Figure 13). Glaciers of the Central Chilean Andes had the highest density of $SLA_{EOS}$ results across the 21 years (mean counts > 19 for majority of tessellation cells; Figure 13b), followed by the Southern Alps (mean counts > 16 for majority of tessellation cells; Figure 13a). The Tropical Andes and Antarctic Peninsula had a lower density of results (mean counts of 3-10 for majority of tessellation cells; Figures 13b and 13c), and the Southern Andes had markedly lower density of results south of 50˚S (mean counts 3-7) compared to north of 50˚S (mean counts 10-21). Similarly, the Central Andes had a greater density of results in the west compared to the east.

**Table 5.** Glacier sample sizes per study region after glaciers which returned no $SLA_{EOS}$ results were removed.

| Region | n | n (east) | n (west) |
|---|---|---|---|
| Southern Alps | 628 | 317 | 311 |
| Antarctic Peninsula | 1627 | 458 | 1169 |
| Tropical Andes | 131 | 45 | 86 |
| Central Andes | 440 | 399 | 41 |
| Central Chilean Andes | 566 | 357 | 209 |
| Southern Andes | 3093 | 1389 | 1704 |

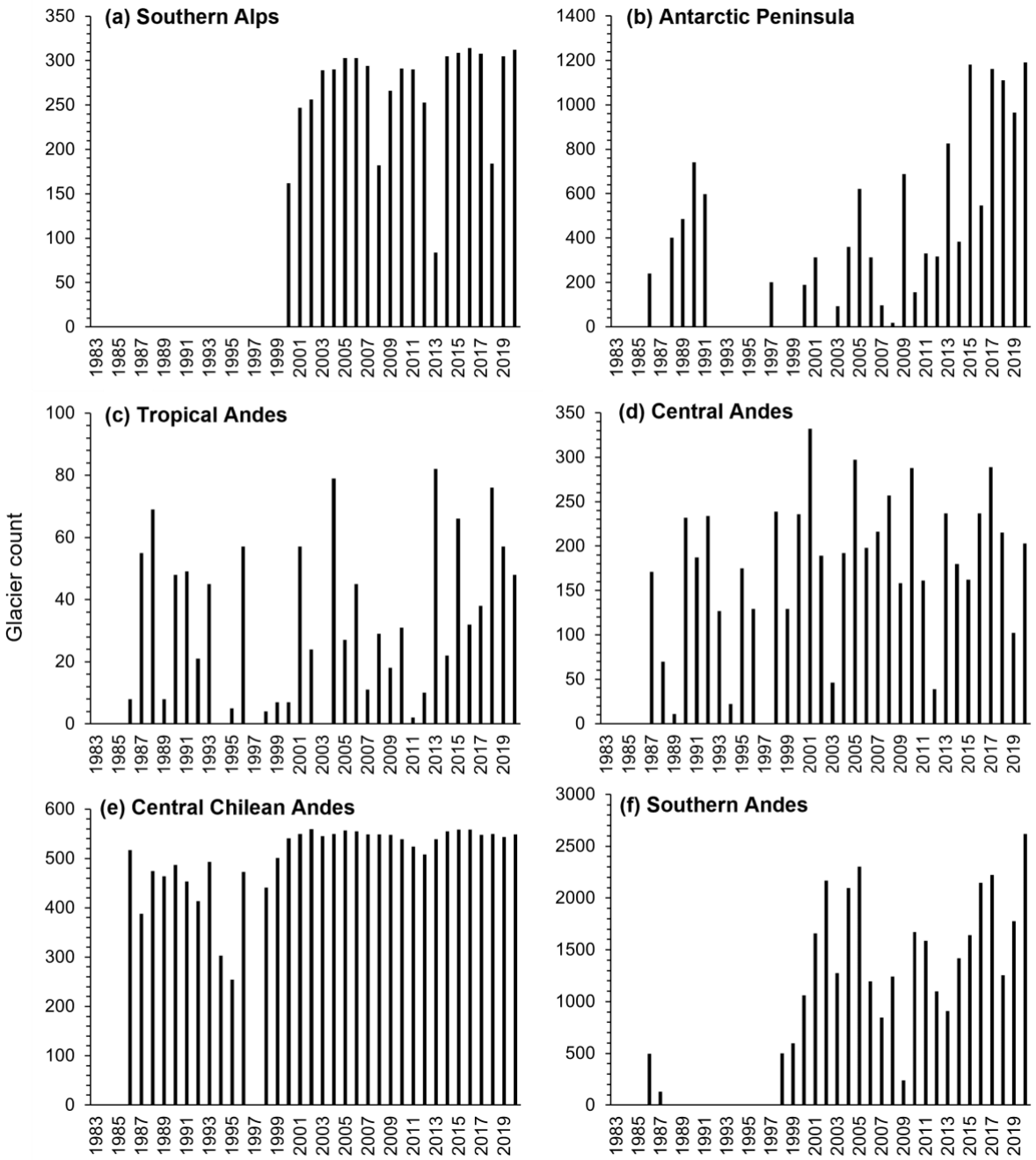


**Figure 12.** Annual counts of glaciers with $SLA_{EOS}$ results retrieved. Density of $SLA_{EOS}$ results is lower pre-2000 for the Southern Alps, Antarctic Peninsula, and Southern Andes.

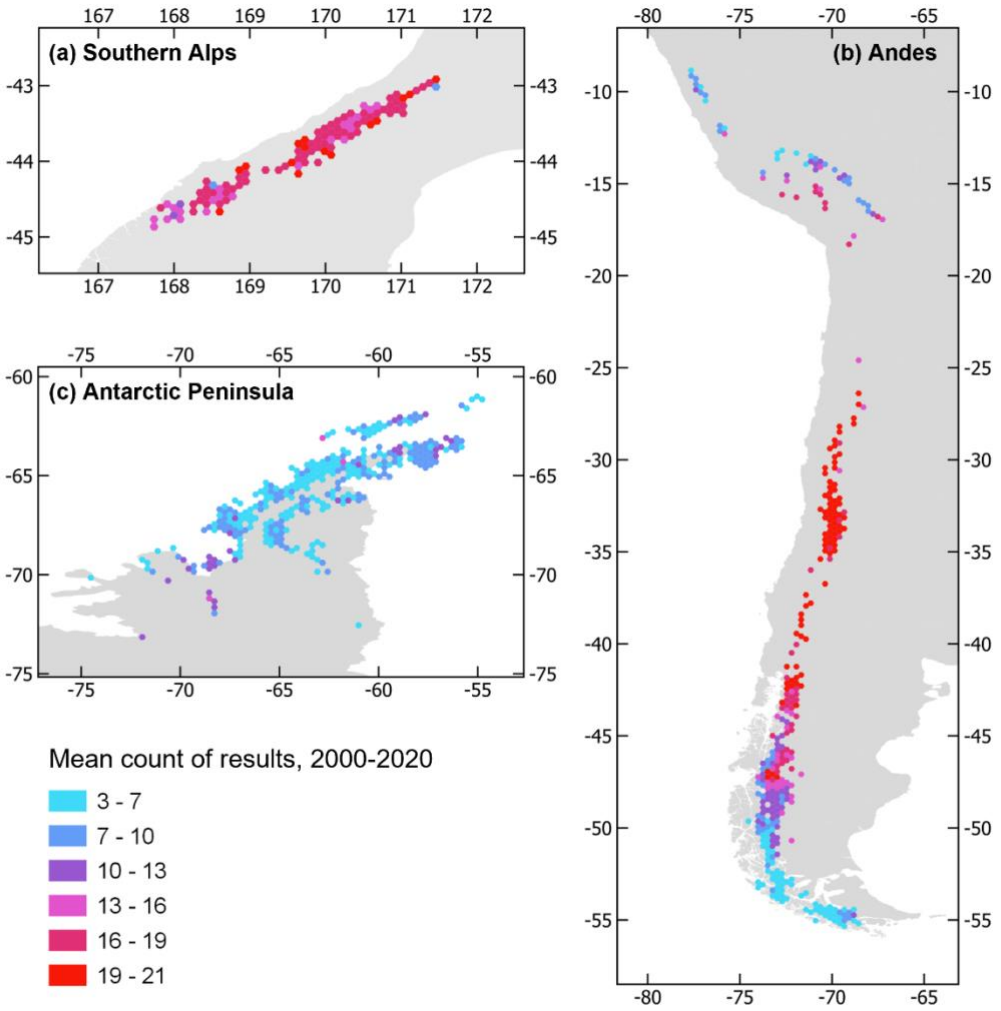


**Figure 13.** Spatial distribution of the $SLA_{EOS}$ result density (count of years from 2000-2020 with results retrieved) across all regions, where each tessellation cell is the mean result count of glacier centroids within it. Highest quantity of results for the Central Chilean Andes and Southern Alps; lowest quantity of results for the Antarctic Peninsula, Tropical Andes, and Southern Andes.

### 4.2. Test glacier $SLA_{EOS}$

Mean $SLA_{EOS}$ for the Southern Alps test glaciers has a rising trend, which is in accordance with results produced by the New Zealand aerial survey (Figure 14), and there is no statistically significant difference in $SLA_{EOS}$ means determined by the two methods (Paired t-Test, $p = 0.062$). However, mean test glacier $SLA_{EOS}$ was found to rise at a rate of 2.54 m $yr^{-1}$ for the 21-year period, which is considerably lower than the 7.04 m $yr^{-1}$ rate of change identified by the aerial survey method (Lorrey et al., 2022). Eastern test glaciers displayed a high rate of $SLA_{EOS}$ rise (4.09 m $yr^{-1}$) compared to the minimal $SLA_{EOS}$ change detected for western test glaciers (0.81 m $yr^{-1}$). This east-west contrast in rate also differs from the aerial survey findings, which indicated that eastern $SLA_{EOS}$ increased at a lower rate (6.31 m $yr^{-1}$) than western $SLA_{EOS}$ (8.21 m $yr^{-1}$) (Lorrey et al., 2022).

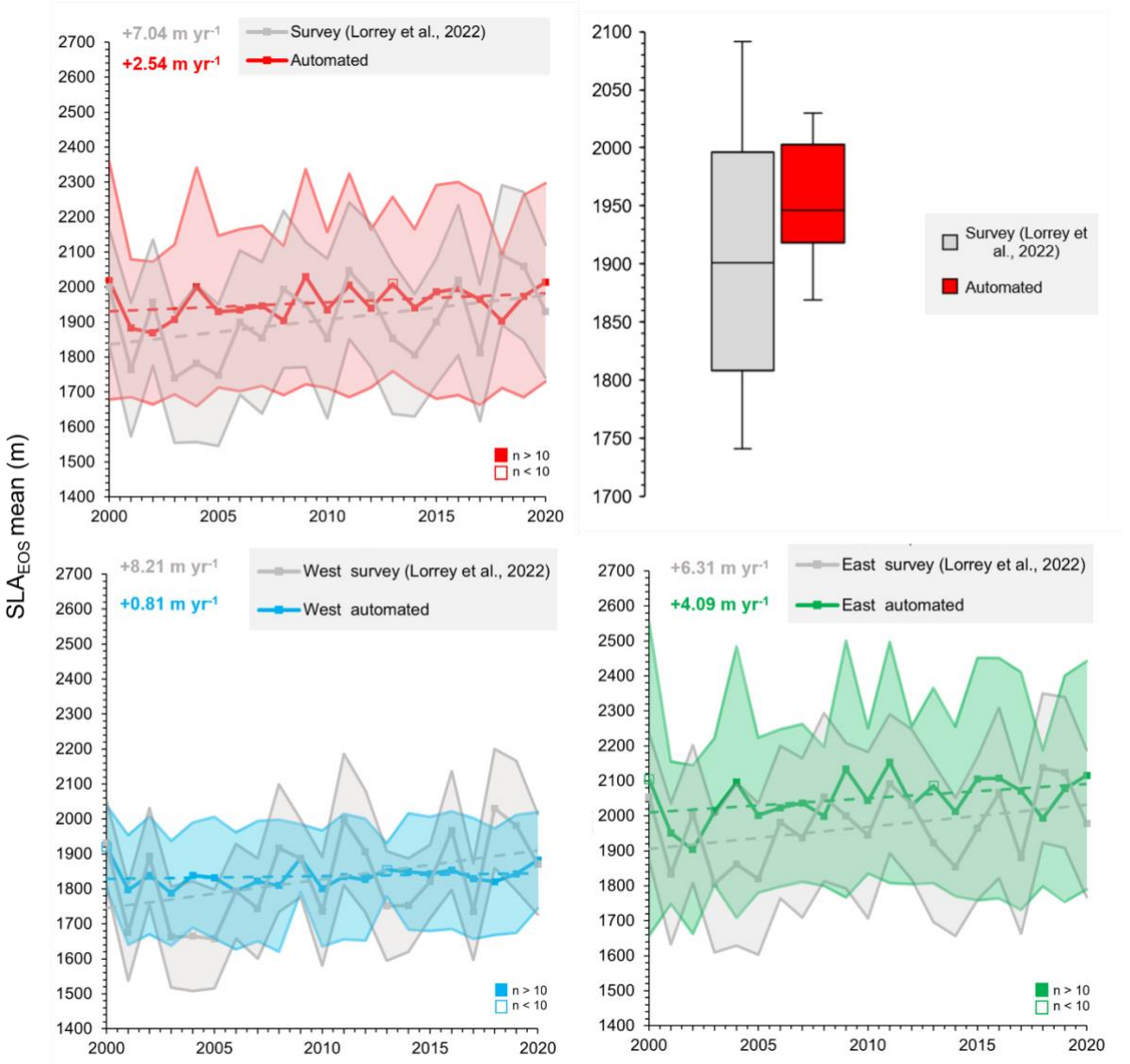


**Figure 14.** Comparison of automated $SLA_{EOS}$ annual means with New Zealand aerial survey $SLA_{EOS}$ annual means (Lorrey et al., 2022) for test glaciers (n =34). Top left: time series and trends of $SLA_{EOS}$ change for all test glaciers. Top right: boxplot of variation in $SLA_{EOS}$ means for all test glaciers. Bottom left: time series and trends of $SLA_{EOS}$ change for west-draining test glaciers (n =15). Bottom right: time series and trends of $SLA_{EOS}$ change for east-draining test glaciers (n =19). Hollow data points used when mean calculated from < 10 glaciers. Shaded areas represent ± 1 S.D..

Despite disparities in rates of $SLA_{EOS}$ change inferred by the two methods, the inter-annual variability in automated $SLA_{EOS}$ remains within ± 1 standard deviation (S.D.) of aerial survey $SLA_{EOS}$, with the exception of years 2004, 2005, and 2018 for western test glaciers (Figure 14). Additionally, there were periods of inter-annual variability in mean $SLA_{EOS}$ which accord with the pattern from aerial survey results: 2003 to 2005, 2009 to 2012, and 2014 to 2017.

Overall, automated $SLA_{EOS}$ means were higher (median = 1947 m a.s.l.) than aerial survey $SLA_{EOS}$ means (median = 1901 m a.s.l.) for the period 2000-2020 (Figure 14). The range in aerial survey $SLA_{EOS}$ was far greater than for automated $SLA_{EOS}$; $SLA_{EOS}$ maximum values were 2091 m a.s.l. (survey method) and 2030 m a.s.l. (automated method), while $SLA_{EOS}$ minimum values were 1741 m a.s.l. (survey method) and 1869 m a.s.l. (automated method). The disparity in $SLA_{EOS}$ variation in the two datasets is also shown in the higher mean S.D. of survey results (± 108 m) compared to automated results (± 48 m).

### 4.3. Temporal variation in $SLA_{EOS}$

#### *4.3.1. Southern Alps*

Over the 2000 to 2020 period, there was a statistically significant ($p = 0.01$) rise in Southern Alps mean $SLA_{EOS}$ of 2.19 m $yr^{-1}$ (Figure 15a). Despite the difference in sample size of the Southern Alps test glaciers (n = 34) and entire Southern Alps region (n = 636), the rates of $SLA_{EOS}$ change identified in each case differed by only 0.35 m $yr^{-1}$ and were not significantly different ($p = 0.976$; Figures 14 and 15a). Compared to other study regions, the Southern Alps displayed least inter-annual variability in $SLA_{EOS}$, ranging from a minimum of 1994 m a.s.l. (2001) to a maximum of 2088 m a.s.l. (2016). Correspondingly, annual anomalies from long-term mean $SLA_{EOS}$ were smallest for this region; however, there was a clear negative-to-positive shift in $SLA_{EOS}$ anomaly in 2011 (Figure 16a), which aligned with the finding of strong statistical significance in this region's overall $SLA_{EOS}$ trend.

#### *4.3.2. Antarctic Peninsula*

The Antarctic Peninsula also displayed a statistically significant ($p = 0.045$) increase in mean $SLA_{EOS}$ between 2000 and 2020 (3.74 m $yr^{-1}$; Figure 15b). During this time, mean $SLA_{EOS}$ varied from a minimum of 293 m a.s.l. in 2001, to a maximum of 489 m a.s.l. in 2018. As with the Southern Alps, there was a notable negative-to-positive shift in the annual anomalies of mean $SLA_{EOS}$ from the long-term mean, though this occurred later in the period, in 2017 (Figure 16b).

#### *4.3.3. Tropical Andes*

There was a statistically significant ($p = 0.044$) increase in Tropical Andes mean $SLA_{EOS}$ from 2000-2020, at a rate exceeding that of other Southern Hemisphere study regions (6.28 m $yr^{-1}$; Figure 15c). However, the Tropical Andes also had the most limited data availability (Figure 12) and glacier sample size of the regions; the mean number of Tropical Andes glaciers used to calculate annual $SLA_{EOS}$ was 36. Strong inter-annual variability was visible in the $SLA_{EOS}$ trend, and values ranged from a minimum of 4933 m a.s.l. in 2006, to maximum of 5217 m a.s.l. in 2014. Accordingly, annual $SLA_{EOS}$ anomalies from long-term mean were variable; nevertheless, due to lack of high positive $SLA_{EOS}$ anomalies pre-2008, an overall trend of increasing $SLA_{EOS}$ anomaly was identified (Figure 16c).

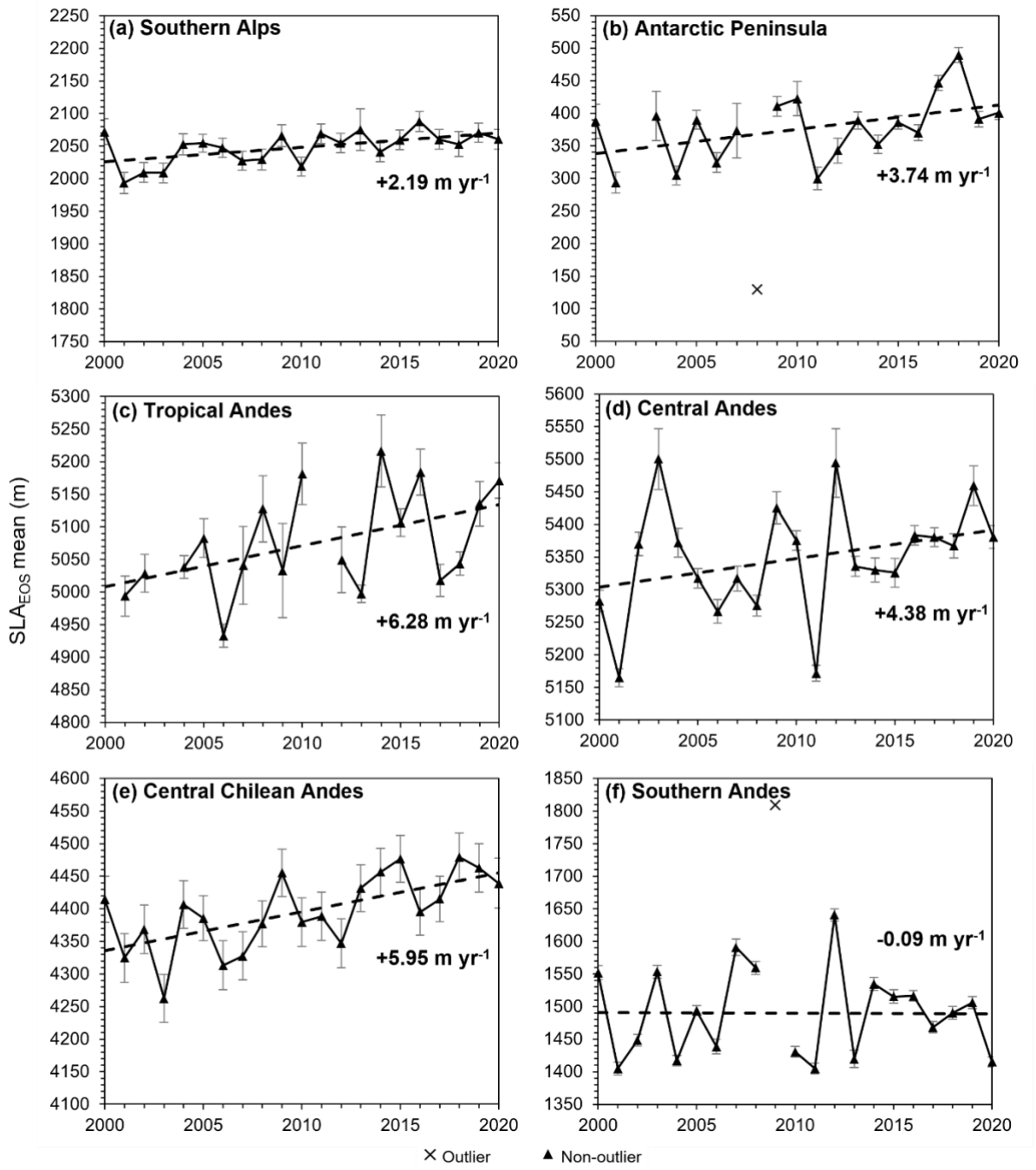


**Figure 15.** Time series and rates of mean $SLA_{EOS}$ change for the six study regions from 2000-2020. Outliers highlighted but excluded from linear regressions (dashed line). Data points were excluded from plots where the sample size of the annual $SLA_{EOS}$ mean was < 10% of the regional sample size. Error bars are ± 1 S.E.

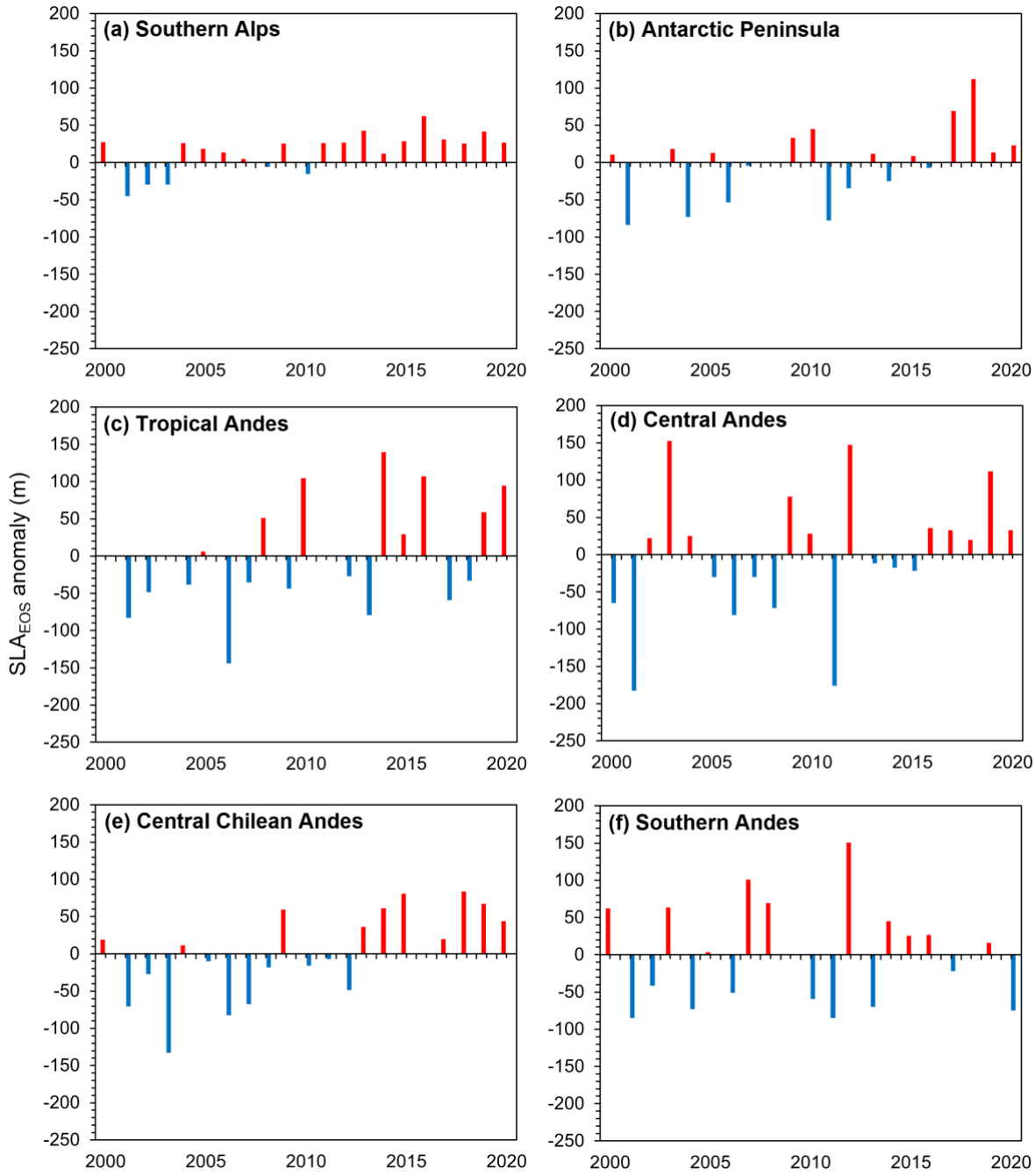


**Figure 16.** Annual $SLA_{EOS}$ anomalies from regional long-term (2000-2020) means. Years with positive $SLA_{EOS}$ anomalies (higher-than-mean snowline) in red, and years with negative $SLA_{EOS}$ anomalies (lower-than-mean snowline) in blue.

### *4.3.4. Central Andes*

Central Andes mean $SLA_{EOS}$ increased between 2000 and 2020 at a rate of 4.38 m $yr^{-1}$ (Figure 15d), though this trend was not statistically significant ($p = 0.169$). This region displayed the largest range in annual $SLA_{EOS}$ means, particularly between the 2001 minimum (5165 m a.s.l.) and 2003 maximum

(5500 m a.s.l.). Correspondingly, the trend had one of the lowest R-squared values of the regions (0.097) and highly varied annual $SLA_{EOS}$ anomalies, which showed no clear trend from 2000-2020 (Figure 16d).

*4.3.5. Central Chilean Andes*

The Central Chilean Andes displayed a statistically significant (p=0.002) increase in mean $SLA_{EOS}$ from 2000-2020, at a rate of 5.95 m $yr^{-1}$ (Figure 15e). Although the second greatest rate of $SLA_{EOS}$ increase among the regions, this trend had the highest R-squared value (0.405), and enhanced result density (Figure 12) meant that the mean number of glaciers used to calculate annual mean $SLA_{EOS}$ was 546. Inter-annual variability was moderate but weaker than for other Andes study regions. Mean $SLA_{EOS}$ ranged from a minimum of 4262 m a.s.l. (2003) to a maximum of 4479 m a.s.l. (2018). There was a clear increasing trend in annual $SLA_{EOS}$ anomalies, with a convincing negative-to-positive shift in $SLA_{EOS}$ anomaly in 2013 (Figure 16e).

*4.3.6. Southern Andes*

The Southern Andes was the only study region which displayed an overall lowering of mean $SLA_{EOS}$ from 2000-2020 (Figure 15f). However, the rate of decrease was slight (-0.09 m $yr^{-1}$) and not statistically significant ($p = 0.972$), presenting an R-squared value < 0.001. The result was therefore regarded as showing no change in mean $SLA_{EOS}$ across the period. Despite no overall trend being identified, Southern Andes mean $SLA_{EOS}$ did increase from a minimum in 2001 (1405 m a.s.l.) to a maximum in 2012 (1641 m a.s.l.). Annual $SLA_{EOS}$ anomalies from long-term mean also showed no overall trend from 2000-2020 and had high inter-annual variability (Figure 16f).

*4.3.7. Andean sub-regions*

Of the five small-scale Andean sub-regions, four displayed increasing mean $SLA_{EOS}$ (between 1.49 and 4.79 m $yr^{-1}$), and one (Cordillera Darwin) displayed decreasing mean $SLA_{EOS}$ (-3.05 m $yr^{-1}$) from 2000-2020 (Figure 17). $SLA_{EOS}$ inter-annual variability was strong at each site, and the overall trends were not statistically significant ($p > 0.05$).

The two sites with highest latitude – Cordillera Darwin and SPI – had the least positive rates of $SLA_{EOS}$ change over the period (Figure 17). The NPI displayed a greater rate of $SLA_{EOS}$ rise (2.78 m $yr^{-1}$) than the neighbouring SPI (1.49 m $yr^{-1}$). The latter presented strongest inter-annual variability of all sub-regions, but it should be noted that SPI maximum mean $SLA_{EOS}$ (1661 m a.s.l. in 2012) was calculated from an annual glacier sample < 10% of the total SPI glacier sample (Figure 17).

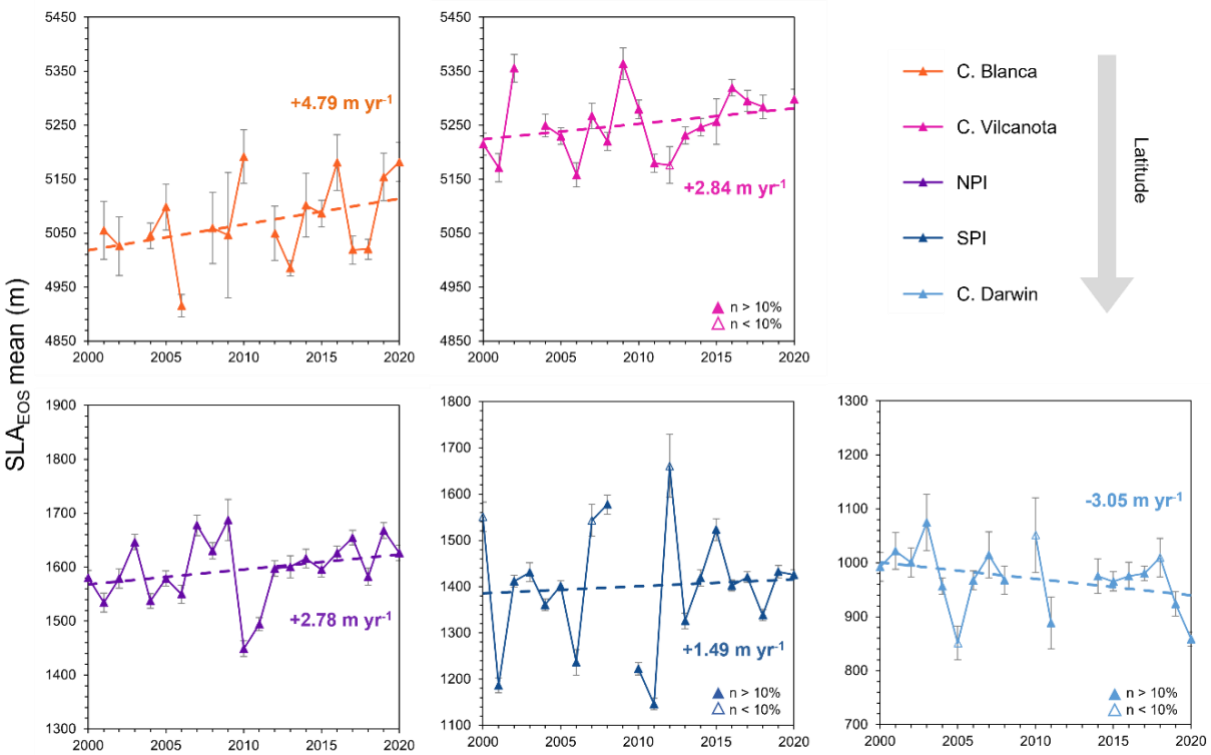


**Figure 17.** Time series and rates of mean $SLA_{EOS}$ change for the five Andean sub-regions from 2000-2020. Hollow data points used when annual sample < 10% of total sub-regional sample. Error bars show ± 1 S.E.

### 4.4. Spatio-temporal variation in $SLA_{EOS}$

*4.4.1. Southern Alps*

Across the 21-year period, $SLA_{EOS}$ maintained consistent spatial variation at the Southern Alps regional scale (Figure 18). $SLA_{EOS}$ follows a general increasing trend from south-west to north-east; it is consistently highest (~2300 to 2700 m a.s.l.) in the region of 43.5˚S, 170.5˚E, but with a smaller region of high $SLA_{EOS}$ (~2200 to 2600 m a.s.l.) existing at approximately 44.6˚S, 168.7˚E.

Smaller changes in $SLA_{EOS}$ through time were difficult to observe at regional scale due to the wide range in $SLA_{EOS}$ observed. However, there were some regions within the Southern Alps which underwent clear $SLA_{EOS}$ changes. Generally, between periods 2000-2005 and 2015-2020, $SLA_{EOS}$ increased and the south-west to north-east contrast was maintained. The north-east region of 43.5˚S, 170.5˚E had a maximum mean $SLA_{EOS}$ of 2400 m a.s.l. in the first time period, and 2700 m a.s.l. in the last; the south-west region of 44.3˚S, 168.5˚E had a minimum mean $SLA_{EOS}$ of 1400 m a.s.l. in the first three time periods, and 1500 m a.s.l. in the last (Figure 18).

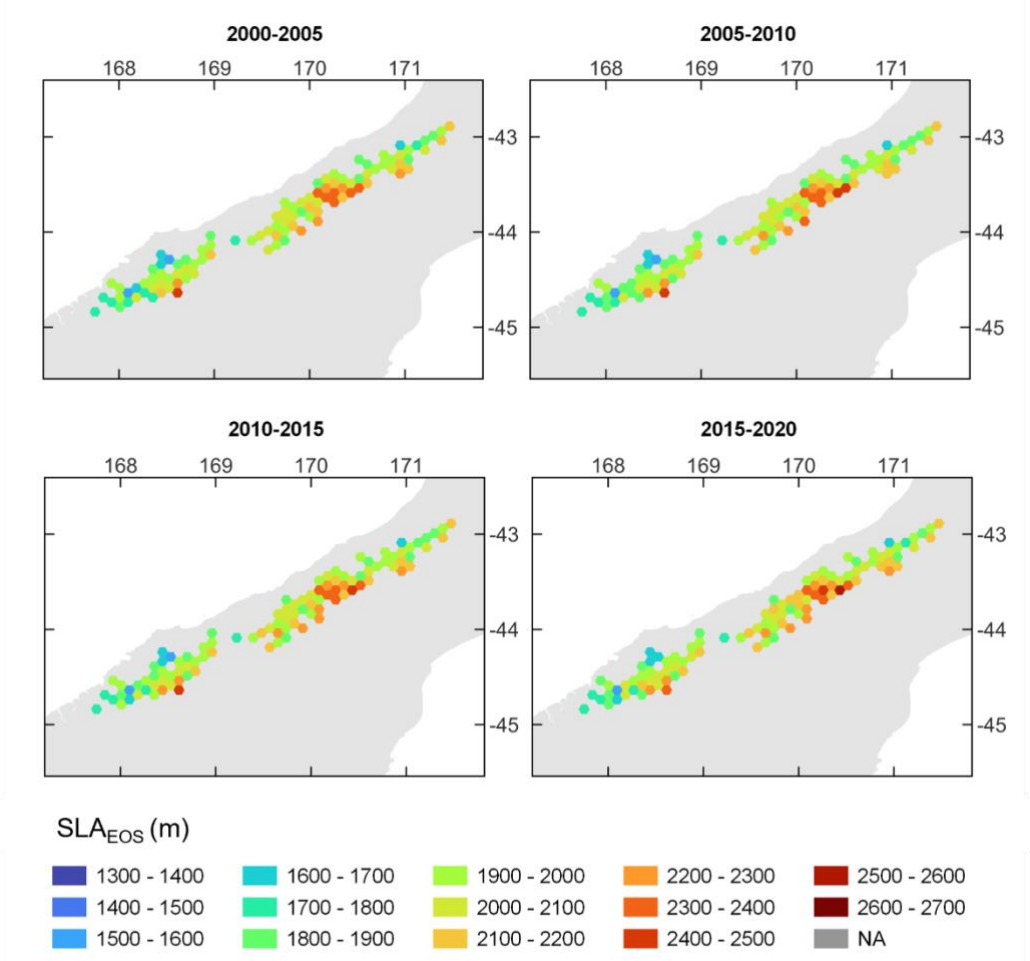


**Figure 18.** Mean spatial variation in Southern Alps $SLA_{EOS}$ for time periods: 2000-2005, 2005-2010, 2010-2015, and 2015-2020. Each 0.1-degree tessellation cell contains the mean $SLA_{EOS}$ value of glacier centroids within it.

### *4.4.2. Antarctic Peninsula*

$SLA_{EOS}$ was highly variable across the Antarctic Peninsula from 2000-2020 (Figure 19). Typically, inland regions displayed higher $SLA_{EOS}$ (> 1100 m a.s.l.) than many coastal regions (< 200 m a.s.l.; including the periphery South Shetland and South Orkney islands). However, the north-east coast of the Antarctic Peninsula, between 65˚W and 60˚W, had noticeably higher $SLA_{EOS}$ (~300 to 800 m a.s.l.) than other coastal regions, particularly from 2000-2010.

As with the Southern Alps, smaller $SLA_{EOS}$ changes were difficult to visualise spatially for the wide range of Antarctic Peninsula $SLA_{EOS}$, but a general rise in $SLA_{EOS}$ could be observed in the west coast region of 67˚S, 68˚W, where minimum mean $SLA_{EOS}$ was < 50 m a.s.l. during 2000-2015 but > 50 m a.s.l. during 2015-2020. Likewise, at the inland region of 68˚S, 65˚W, mean $SLA_{EOS}$ was ~100 to 300 m a.s.l. from 2000-2005 but ~300 to 500 m a.s.l. from 2015-2020 (Figure 19). In the Trinity Peninsula region (64˚S, 58˚W), maximum mean $SLA_{EOS}$ was 400 m a.s.l. during 2000-2005 but 700 m a.s.l. during 2015-2020. Through time, these changes reduced the contrast between coastal and inland $SLA_{EOS}$.

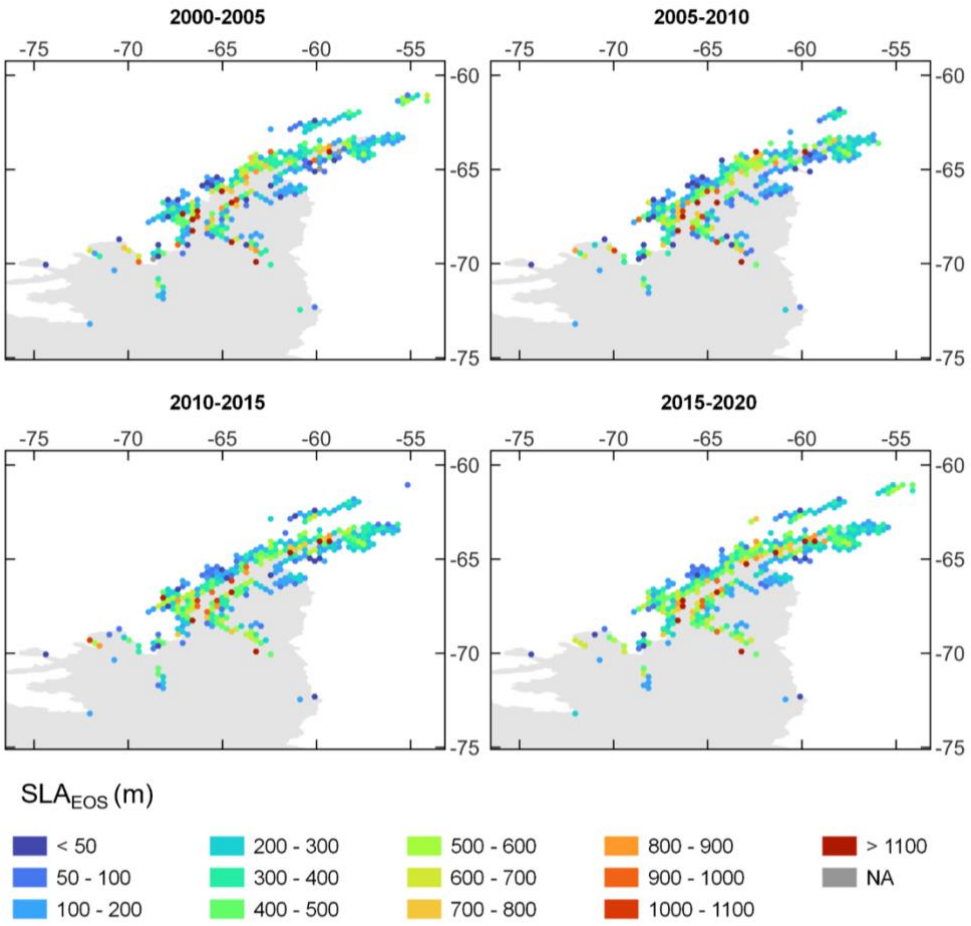


**Figure 19.** Mean spatial variation in Antarctic Peninsula $SLA_{EOS}$ for time periods: 2000-2005, 2005-2010, 2010-2015, and 2015-2020. Each 0.3-degree tessellation cell contains the mean $SLA_{EOS}$ value of glacier centroids within it.

### *4.4.3. Andes*

Across the Andes, there was a striking difference between the high $SLA_{EOS}$ (< 5000 m a.s.l.) of northern regions and low $SLA_{EOS}$ (< 1400 m a.s.l.) of southern regions (Figure 20). For all time periods, there were clear spatial distinctions in $SLA_{EOS}$ at latitudes 37˚S and 52˚S. In the Southern Andes region, between 45˚S and 52˚S, $SLA_{EOS}$ increased from between 600 and 1000 m a.s.l. to between 1400 and 1800 m a.s.l. along a west-east gradient.

Between periods 2005-2010 and 2010-2015, and between periods 2010-2015 and 2015-2020, there was a clear increase in the proportion of high $SLA_{EOS}$ (4600 to 5000 m a.s.l.) zones in the Tropical Andes (Figure 20). Similarly for the Central Andes, maximum and minimum $SLA_{EOS}$ did not change between periods 2000-2005 and 2015-2020, but the proportion of high $SLA_{EOS}$ (> 5000 m a.s.l.) zones increased clearly (Figure 20). $SLA_{EOS}$ changes were less pronounced for the Central Chilean Andes; however, in

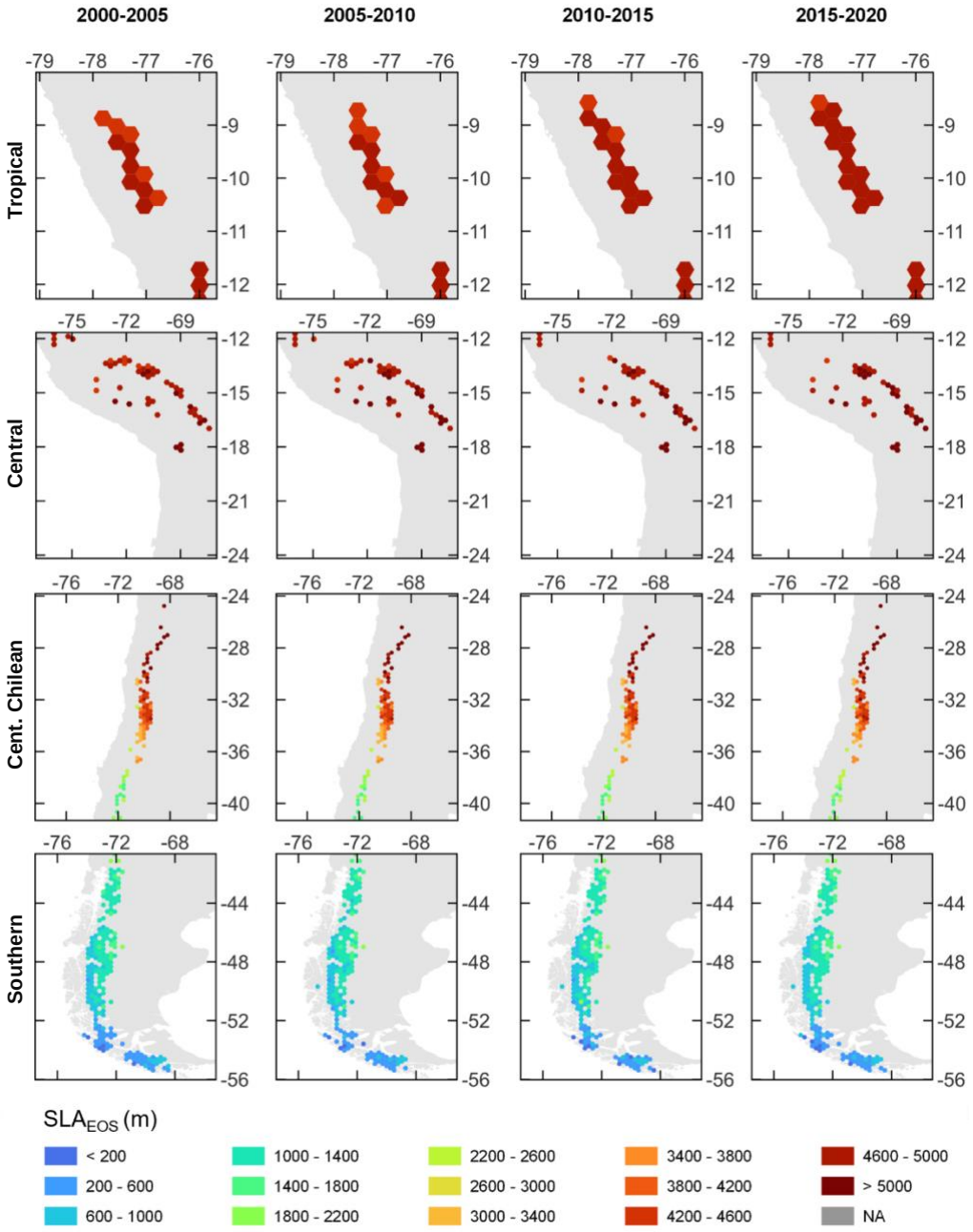


**Figure 20.** Mean spatial variation in Andes $SLA_{EOS}$ for time periods: 2000-2005, 2005-2010, 2010-2015, and 2015-2020. Each 0.3-degree tessellation cell contains the mean $SLA_{EOS}$ value of glacier centroids within it.

the region of 31-35˚S, maximum $SLA_{EOS}$ increased from between 4600 and 5000 m a.s.l. to > 5000 m a.s.l., and in the smaller region of 36-37˚S, minimum $SLA_{EOS}$ increased from between 3000 and 3400 m a.s.l. to between 3400 and 3800 m a.s.l. (Figure 20). The Southern Andes maintained its east-west $SLA_{EOS}$ gradient through the study period, and there was minimal indication of $SLA_{EOS}$ increase compared to other Andes regions. However, from 53-54˚S, there was a small increase in the proportion of low $SLA_{EOS}$ (< 200 m a.s.l.) zones between periods 2000-2005 and 2015-2020 (Figure 20).

### 4.5. Spatio-temporal variation in $SLA_{EOS}$ change

#### *4.5.1. Southern Alps*

The east Southern Alps had consistently higher mean $SLA_{EOS}$ than the west from 2000-2020. There was a statistically significant increase in $SLA_{EOS}$ over the 21-year period for both east (2.70 m $yr^{-1}$; p = 0.002) and west (1.63 m $yr^{-1}$; p = 0.049) zones, though eastern $SLA_{EOS}$ increased at a greater rate (Figure 21). In both the east and west Southern Alps, rates of $SLA_{EOS}$ change were higher during 2010-2020 than 2000-2010, though this difference was greater for western glaciers than eastern glaciers (Figure 22).

On observing finer scale spatial variations between 0.1-degree tessellation cells, most of the Southern Alps region experienced mean $SLA_{EOS}$ increases at rates between 0 and 5 m $yr^{-1}$ (Figure 21a). The south-west region had higher spatial variability in $SLA_{EOS}$ change, displaying maximum rates of > 30 m $yr^{-1}$ and minimum rates of -10 to -5 m $yr^{-1}$; this region also had a greater coverage of tessellation cells showing $SLA_{EOS}$ lowering, mostly between -1 and 0 m $yr^{-1}$ of mean change (Figure 21a).

#### *4.5.2. Antarctic Peninsula*

In the Antarctic Peninsula, western glaciers had higher mean $SLA_{EOS}$ than eastern glaciers for all years except 2010, 2014, 2016 and 2020. The east and west zones experienced opposite $SLA_{EOS}$ trends from 2000-2020; eastern $SLA_{EOS}$ increased significantly (5.24 m $yr^{-1}$; p = 0.013), and west $SLA_{EOS}$ decreased non-significantly (-0.28 m $yr^{-1}$; p = 0.921) (Figure 21b). However, it is also worth noting a reversal of the west $SLA_{EOS}$ trend in 2014, after which $SLA_{EOS}$ began to rise rapidly (21.6 m $yr^{-1}$). As such, the east and west displayed opposite $SLA_{EOS}$ trends between the 2000-2010 and 2010-2020 decades; the rate of $SLA_{EOS}$ change decreased in the second decade for eastern glaciers but increased from a negative to positive rate of change for western glaciers (Figure 22).

Rates of $SLA_{EOS}$ change were highly variable across the Antarctic Peninsula, with minimums of -30 to -15 m $yr^{-1}$ and maximums > 30 m $yr^{-1}$ (Figure 21b). Trinity Peninsula was a less variable region, where mean $SLA_{EOS}$ change ranged from -1 to 5 m $yr^{-1}$. Neighbouring this region, there was a clear north-south contrast (Figure 21b); the south coast (~65˚S, 60˚W) experienced $SLA_{EOS}$ increase (mostly between 5 and 30 m $yr^{-1}$), while the north coast (~64˚S, 60˚W) experienced $SLA_{EOS}$ decrease (mostly between -10 and -5 m $yr^{-1}$). As drainage data designates this north region as ‘west’ and south region as ‘east’, this north-south spatial variation was described in the east-west trends.

#### *4.5.3. Tropical Andes*

In the Tropical Andes, west $SLA_{EOS}$ was generally higher than east $SLA_{EOS}$ from 2000-2020, and east $SLA_{EOS}$ increased at a slightly higher rate (7.55 m $yr^{-1}$) than west $SLA_{EOS}$ (6.10 m $yr^{-1}$) (Figure 21c). Though, both east and west trends were not statistically significant (p = 0.214 and 0.056 respectively),

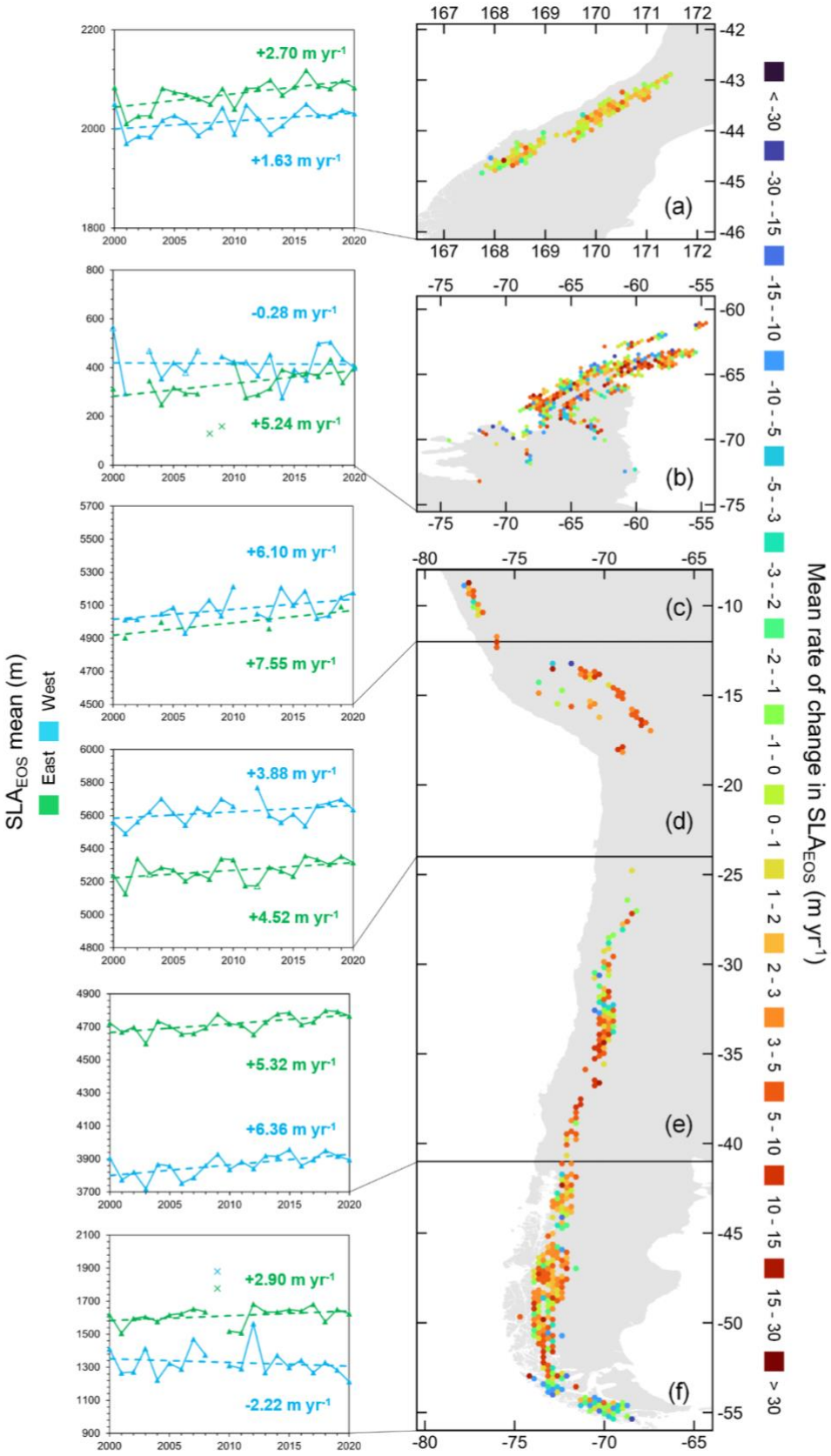


**Figure 21.** Spatial variation in rates of $SLA_{EOS}$ change, 2000-2020. Left: $SLA_{EOS}$ time series for east and west zones; outliers excluded from trends and data points hollow when annual sample < 10% of total sample. Right: tessellation of rates of $SLA_{EOS}$ change; cells display mean rate for glacier centroids within it. (a) Southern Alps; (b) Antarctic Peninsula; (c) Tropical Andes; (d) Central Andes; (e) Central Chilean Andes; (f) Southern Andes.

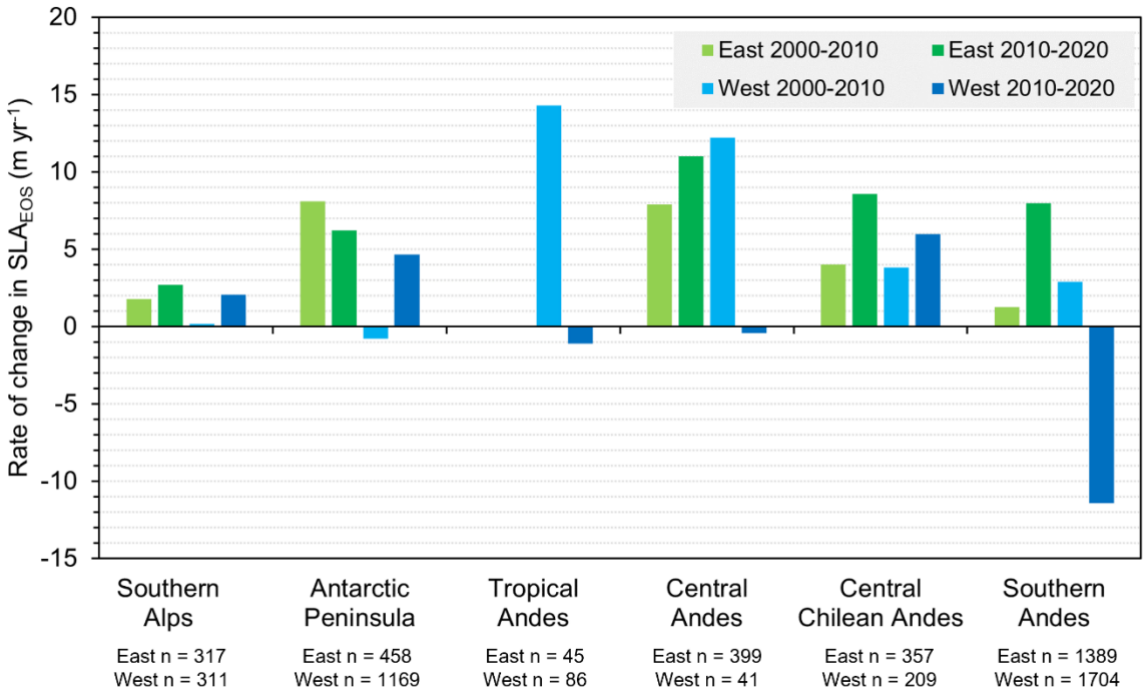


**Figure 22.** Rates of change in mean $SLA_{EOS}$ for studied decades (2000-2010 and 2010-2020) and sub-regions (east and west). Post-filtering sample size (n) of each regional zone displayed along x-axis. Too few years of data in each decade for the eastern Tropical Andes meant results were excluded.

and limited glacier samples (east = 49; west = 87) and missing years of data (east = 17; west = 3) should be noted here. Insufficient data prevented comparison of east $SLA_{EOS}$ change by decade, but the west displayed a dramatic decline in rates of $SLA_{EOS}$ change between periods 2000-2010 and 2010-2020 (Figure 22).

East-west differences were vaguely resolved in finer-scale spatial variation (Figure 21c), with cells presenting negative $SLA_{EOS}$ changes (-10 to 0 m yr$^{-1}$) situated west, and cells presenting the most positive rates of $SLA_{EOS}$ change (10 to 30 m yr$^{-1}$) situated east.

*4.5.4. Central Andes*

Western $SLA_{EOS}$ was consistently higher than eastern $SLA_{EOS}$ in the Central Andes from 2000-2020. Although both east and west zones displayed overall trends in $SLA_{EOS}$ which were not statistically significant ($p = 0.052$ and 0.120 respectively), east $SLA_{EOS}$ increased at a greater rate (4.52 m yr$^{-1}$) than west $SLA_{EOS}$ (3.88 m yr$^{-1}$) over the 21 years (Figure 21d). Overall trends were reversed during 2000-2010, when the rate of $SLA_{EOS}$ change was more positive for western glaciers (Figure 22). During 2010-2020, the eastern Central Andes experienced increased rates of $SLA_{EOS}$ rise, while the west experienced a shift to lowering $SLA_{EOS}$. Relatively small sample size of western Central Andes glaciers (n = 41) should be noted here.

Like the Tropical Andes, finer scale variations showed that higher rates of $SLA_{EOS}$ change were more prominent in the east (generally 1 to 15 m $yr^{1}$) than the west (generally -2 to 15 m $yr^{-1}$) (Figure 21d). There were few outlying high (> 30 m $yr^{-1}$) and low (> -30 m $yr^{-1}$) changes in mean $SLA_{EOS}$ in the northern Central Andes. These cells corresponded to a sparse data region (Figure 13b).

*4.5.5. Central Chilean Andes*

In the Central Chilean Andes, east $SLA_{EOS}$ was consistently higher than west $SLA_{EOS}$ from 2000-2020. During this time, there was a significant increase in east $SLA_{EOS}$ (5.32 m $yr^{-1}$; p = 0.002), which was exceeded by the significant increase in west $SLA_{EOS}$ (6.36 m $yr^{-1}$; p = 0.003) (Figure 21e). Contrary to overall trends, rates of $SLA_{EOS}$ change were higher for eastern glaciers in both decades (Figure 22). Regardless of east and west sub-regions, rates of $SLA_{EOS}$ change were more positive from 2010-2020, than from 2000-2010.

East-west contrast was unclear at finer scale spatial variation, but there was a definitive latitudinal difference in rates of $SLA_{EOS}$ change (Figure 21e); north of ~33˚S, several cells displayed negative $SLA_{EOS}$ changes (-10 to 0 m $yr^{-1}$), but south of ~33˚S, $SLA_{EOS}$ changes were mostly positive (2 to 30 m $yr^{-1}$). Across the entire Andes, 33-38˚S of the Central Chilean range had the highest rates of $SLA_{EOS}$ rise (10 to 30 m $yr^{-1}$) from 2000-2020.

*4.5.6. Southern Andes*

The Southern Andes also displayed higher $SLA_{EOS}$ in the east than the west from 2000-2020. Over this period, east $SLA_{EOS}$ increased non-significantly (2.90 m $yr^{-1}$; p = 0.119) and west $SLA_{EOS}$ decreased non-significantly (-2.22 m $yr^{-1}$; p = 0.486), gradually enhancing the east-west variation in Southern Andes $SLA_{EOS}$ changes (Figure 21f). From 2000-2010, west $SLA_{EOS}$ increased at a slightly higher rate than east $SLA_{EOS}$, contrary to 21-year trends. However, from 2010-2020, the rate of east $SLA_{EOS}$ rise increased, while the rate of west $SLA_{EOS}$ change decreased and showed a lowering $SLA_{EOS}$ trend (Figure 22).

There was notable latitudinal variation in Southern Andes $SLA_{EOS}$ change rates from 2000-2020 (Figure 21f). North of ~53˚S, $SLA_{EOS}$ changes were frequently positive (mostly -1 to 15 m $yr^{-1}$, but some values < 30 m $yr^{-1}$), while south of ~53˚S, there was a shift to negative $SLA_{EOS}$ changes (mostly -10 to -1 m $yr^{-1}$, but some values > -30 m $yr^{-1}$).

**4.6. ERA5-Land climate trends**

*4.6.1. Southern Alps*

ERA5-Land Monthly Aggregated climate data indicated that, throughout the summers of 2000-2020, mean 2 m air temperature was higher for the west Southern Alps, and monthly snowfall sum was higher for the east Southern Alps (Figure 23a). Over this period, monthly snowfall sum lowered at the same rate (-0.0003 m w.e. $yr^{-1}$) in both east and west zones, while warming occurred at a greater rate in the east (0.0569 K $yr^{-1}$) than the west (0.0502 K $yr^{-1}$) (Table 6). Mean monthly summer snowfall was highest in 2003 and lowest in 2016, whilst mean summer temperature was lowest in 2004 and highest in 2019 (Figure 23a).

*4.6.2. Antarctic Peninsula*

Climate data indicated that for 2000-2020 the western Antarctic Peninsula had higher overall summer air temperature, and higher summer monthly snowfall sum for most years (19 of 21) (Figure 23b). In both east and west sub-regions, temperature declined from 2000-2014 (-0.122 K $yr^{-1}$ and -0.070 K $yr^{-1}$ respectively), before increasing rapidly from 2014-2020 (0.244 K $yr^{-1}$ and 0.309 K $yr^{-1}$ respectively); these trends were presented as an overall cooling from 2000-2020 (Table 6). Mean monthly summer snowfall decreased in both east (-0.0004 m w.e. $yr^{-1}$) and west (-0.0011 m w.e. $yr^{-1}$) sub-regions, with the latter exceeding the rates of drying in any other study region (Table 6).

*4.6.3. Tropical Andes*

The west Tropical Andes had higher summer air temperatures than the east throughout the study period, whilst the east had greater monthly summer snowfall than the west in all years but 2019 (Figure 23c). Warming trends were similar between the two regions (0.0363 K $yr^{-1}$ in the east, 0.0390 K $yr^{-1}$ in the west; Table 6) with summer temperatures lowest in 2000 and highest in 2016 (Figure 23c). Decreasing snowfall trends were also similar between the sub-regions, but slightly greater in the west (-0.0004 m w.e. $yr^{-1}$) than the east (-0.0003 m w.e. $yr^{-1}$) (Table 6). Monthly summer snowfall sums were notably higher in 2000 and 2001 than 2020, where they reached minimum for the period (Figure 23c).

*4.6.4. Central Andes*

ERA5-Land presented unambiguously higher summer snowfall in the eastern Central Andes (Figure 23d), indicating that eastern snowfall was increasing (0.0005 m w.e. $yr^{-1}$) in the same magnitude that western snowfall was decreasing (-0.0005 m w.e. $yr^{-1}$) from 2000-2020 (Table 6). Monthly summer snowfall was lowest in 2016 for both regions, and highest in 2000 for the west but 2011 for the east (Figure 23d). Summer air temperature was higher in the western Central Andes, where warming also occurred at a greater rate (0.0332 K $yr^{-1}$) than in the east (0.0252 K $yr^{-1}$) (Table 6). Temperatures increased from minimum in 2000/2001 to maximum in 2016 (Figure 23d), as in the Tropical Andes.

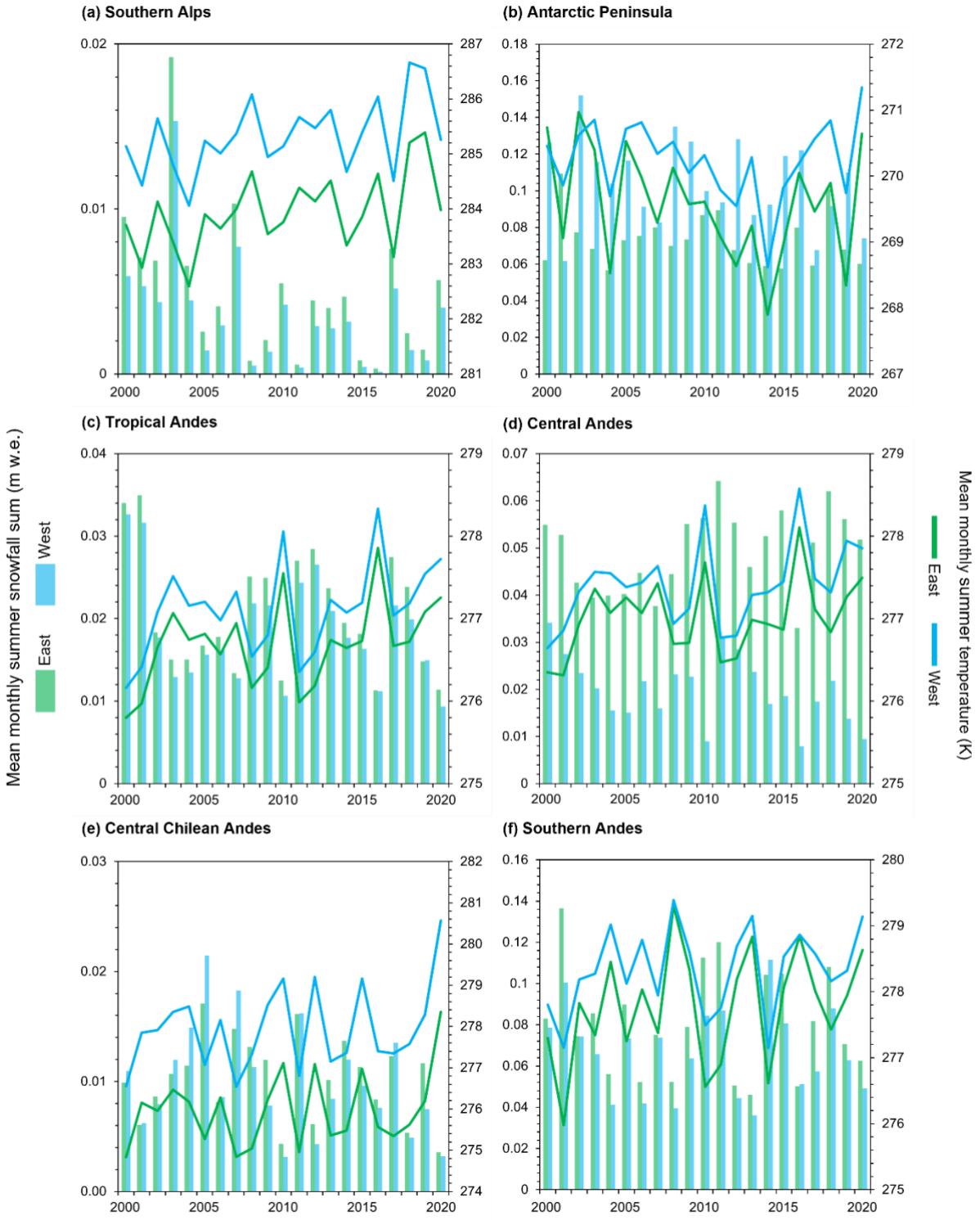


**Figure 23.** Mean summer (December-March) monthly snowfall sum and 2 m air temperature patterns for east and west sub-regions of the six study regions, from 2000-2020. Data derived from ERA5-Land Monthly Aggregated (Muñoz-Sabater, 2019) and available for all 6485 glaciers in the supplementary material.

**Table 6.** ERA5-Land Monthly Aggregated rates of change in mean monthly summer (December-March) 2 m air temperature and snowfall sum, for the east and west sub-regions of the six study regions from 2000-2020.

| Region | Rate of change in mean 2 m air temperature (K $yr^{-1}$) | | Rate of change in mean monthly snowfall sum (m w.e. $yr^{-1}$) | |
|---|---|---|---|---|
| | East | West | East | West |
| Southern Alps | +0.0569 | +0.0502 | -0.0003 | -0.0003 |
| Antarctic Peninsula | -0.0431 | -0.0065 | -0.0004 | -0.0011 |
| Tropical Andes | +0.0363 | +0.0390 | -0.0003 | -0.0004 |
| Central Andes | +0.0252 | +0.0332 | +0.0005 | -0.0005 |
| Central Chilean Andes | +0.0400 | +0.0507 | -0.0001 | -0.0003 |
| Southern Andes | +0.0441 | +0.0281 | -0.0005 | -0.0004 |

*4.6.5. Central Chilean Andes*

The western Central Chilean Andes had higher overall summer temperatures and a greater rate of warming (0.0507 K $yr^{-1}$) than the eastern sub-region (0.04 K $yr^{-1}$) from 2000-2020 (Figure 23e; Table 6). In both sub-regions, temperatures were lowest in 2007 and highest in 2020. Climate data indicated the east to have higher monthly summer snowfall sums in 13 of the 21 years. Snowfall was highest in 2005 and lowest in 2020 (Figure 23e), following drying trends which occurred at a greater rate in the west (-0.0003 m w.e. $yr^{-1}$) than the east (-0.0001 m w.e. $yr^{-1}$) (Table 6).

There were small statistically significant correlations between the rate of change in $SLA_{EOS}$ and the rate of change in ERA5-Land climate variables for eastern Central Chilean Andes glaciers from 2000-2020. More positive rates of change in $SLA_{EOS}$ (rising snowlines) were significantly correlated with more negative rates of change in summer monthly snowfall sum (decreasing snowfall) ($p < 0.001$; $r = -0.274$; Figure 24a), and with more positive rates of change in summer air temperature (increasing temperature) ($p < 0.001$; $r = 0.193$; Figure 24b).

*4.6.6. Southern Andes*

Similar to the other Andean regions, ERA5-Land indicated mean summer air temperature to be higher in the west Southern Andes from 2000-2020 and mean monthly summer snowfall to be higher in the east in most years (Figure 23f). Rates of warming were higher in the east (0.0441 K $yr^{-1}$) than the west (0.0281 K $yr^{-1}$) (Table 6); eastern temperatures varied from a minimum in 2001 to a maximum in 2008 but western temperatures were maximum in 2008 and minimum in 2014 (Figure 23f). Summer snowfall decline occurred at a greater rate in the east (-0.0005 m w.e. $yr^{-1}$) than the west (-0.0004 m w.e. $yr^{-1}$)

(Table 6); mean monthly summer snowfall was lowest in 2013 for both regions, but peaked in 2001 for the east and 2014 for the west (Figure 23f).

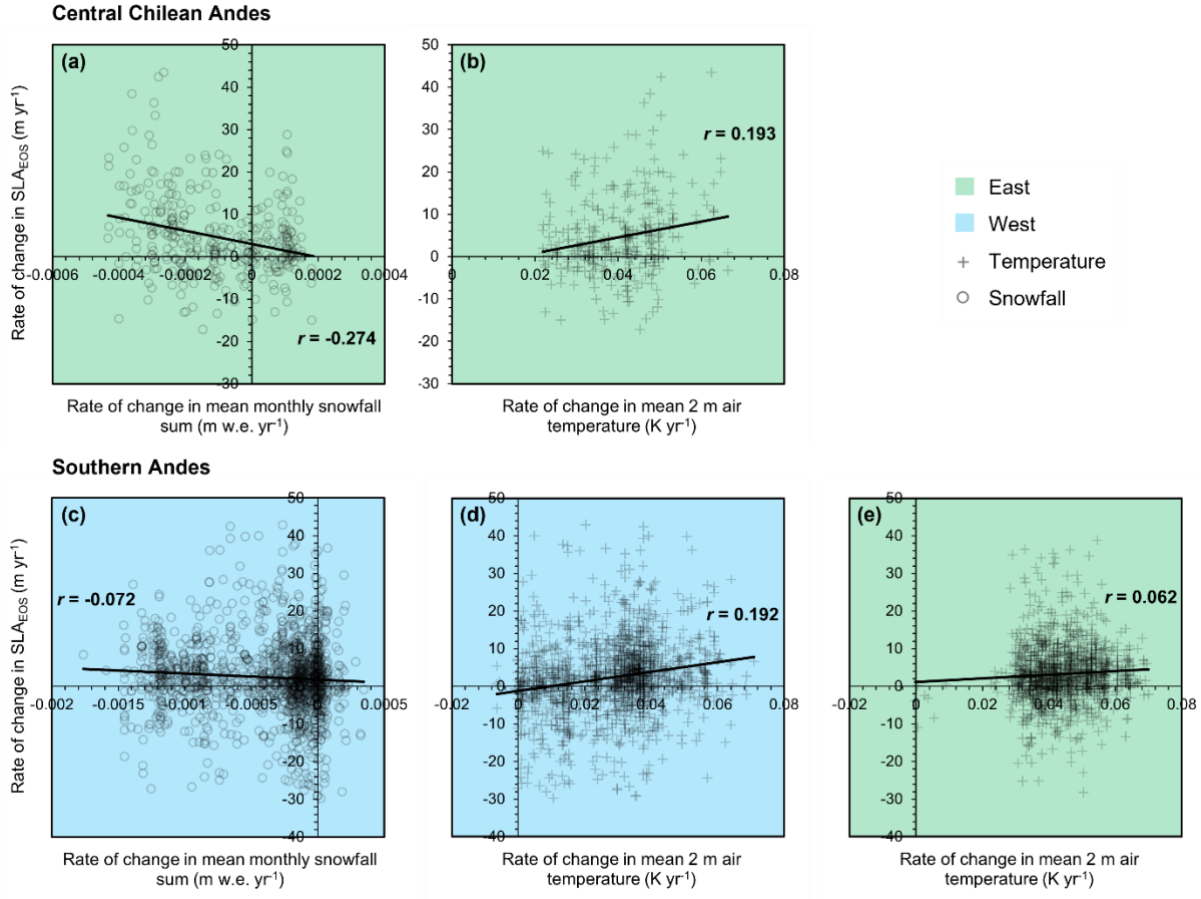


**Figure 24.** Statistically significant ($p < 0.05$) correlations between rates of $SLA_{EOS}$ change and rates of change in summer (December-March) climate variables for glaciers in the east/west sub-regions of the Central Chilean and Southern Andes from 2000-2020. Data derived from ERA5-Land. $SLA_{EOS}$ change outliers were excluded from correlation plots.

There were also small statistically significant correlations between rates of $SLA_{EOS}$ change and rates of change in ERA5-Land climate variables for Southern Andes glaciers from 2000-2020. In the west sub-region, rates of $SLA_{EOS}$ change were negatively correlated with rates of change in monthly summer snowfall ($p = 0.004$; $r = -0.072$; Figure 24c). In both east and west sub-regions, rates of $SLA_{EOS}$ change were positively correlated with rates of change in summer air temperature, and this correlation was stronger for western glaciers ($p < 0.001$; $r = 0.192$; Figure 24d) than for eastern glaciers ($p = 0.023$; $r = 0.062$; Figure 24e).

# 5. Discussion

## 5.1. Spatial variability in $SLA_{EOS}$

### *5.1.1. Southern Alps*

Spatial variability in Southern Alps mean $SLA_{EOS}$ was largely consistent year-on-year, and was shown in an increasing $SLA_{EOS}$ from south-west to north-east (Figure 18). This variability was also consistent between Southern Alps test glaciers and all Southern Alps glaciers, as both samples exhibited higher mean $SLA_{EOS}$ on the inland eastern slopes from 2000-2020 (Figures 14 and 21a); this comparability is likely a result of test glaciers' equal distribution across east-west transects of the region (Chinn, 1995). Comparison with $SLA_{EOS}$ results documented in Lorrey et al. (2022) showed that the New Zealand aerial survey also identified higher mean $SLA_{EOS}$ on eastern glaciers during this time. Aerial survey $SLA_{EOS}$ results were used as a proxy for annual ELA in Carrivick and Chase (2011), which also corroborates the spatial patterns in $SLA_{EOS}$ identified by this study; long-term ELA (1983 to 2009) was documented to increase overall towards the north and east of the range, reaching maximum in the central eastern region. Figure 18 displays this same spatial trend for $SLA_{EOS}$; lowest snowlines were found ~44.5˚S, 168˚E and highest snowlines were found ~43.5˚S, 170.5˚E. As spatial variability is consistent between studies with different timeframes, the similarity exhibits year-on-year consistency of the spatial $SLA_{EOS}$ trend through 1983-2020.

The spatial variability points to the influence of long-term synoptic scale weather systems. The steep elevation increase from sea level at the west coast to > 3000 m a.s.l. at the Main Divide, coupled with prevailing westerly circulation of air masses travelling over the neighbouring Tasman Sea, make for a strong east-west orographic precipitation gradient (Chinn, 1999). This results in greater snowfall on west-draining glaciers (Henderson and Thompson, 1999), which was previously calculated to be a difference of ~30% (Purdie et al., 2011). The synoptic control on snow accumulation explains the lower western $SLA_{EOS}$ identified in this study. There is also a latitudinal air temperature gradient across New Zealand which increases from south to north (MetService, 2023; NIWA, no date). Although this gradient may be smaller across the relatively short latitudinal range of the Southern Alps, it aids explanation of the lower mean $SLA_{EOS}$ in southern regions. The north-south variability in $SLA_{EOS}$ may additionally be explained by the southward aspect and reduced solar radiation receipt of many southern glaciers, which was previously suggested to cause lower ELAs following increased accumulation (Carrivick and Chase, 2011).

### *5.1.2. Antarctic Peninsula*

As expected, regions of higher $SLA_{EOS}$ were consistently found inland of the Antarctic Peninsula from 2000-2020, while coastal regions displayed consistently lower $SLA_{EOS}$ (Figure 19). This difference

reflects spatial variability in minimum glacier elevation, as the coastal Peninsula and surrounding islands host predominantly low-lying marine-terminating glaciers and ice caps (Huber et al., 2017), many with floating or partially floating tongues at sea level (Davies et al., 2012). Similarly, the north-western region of higher $SLA_{EOS}$ (~64-67˚S, 60-66˚W) coincides with abrupt increase in terrain elevation at ~67˚S, 66˚W (Figure 25).

The western sub-region displayed higher mean $SLA_{EOS}$ in most years (Figure 21b). This contrasts to claims that glacier snowlines and ELAs are higher in the east (Carrivick et al., 2019; Davies et al., 2012) and contradicts the west-to-east precipitation decline (González-Herrero et al., 2023; Figure 23b) which arises from orographic influence of the inland plateau on westerly moisture transport (Slonaker and Van Woert, 1999). There are three potential contributors to the finding of higher western $SLA_{EOS}$. Firstly, automatic weather station data and reanalysis data have indicated western air temperature to exceed eastern air temperature (Carrasco et al., 2021; Figure 23b). As high temperature sensitivity is well-documented for glaciers in and around the Antarctic Peninsula (Abram et al., 2013; Davies et al., 2014; Navarro et al., 2013), the influence of temperature gradient may be exceeding the influence of precipitation gradient in the east-west $SLA_{EOS}$ contrast. Secondly, the influence of terrain elevation may also exceed the precipitation influence, with higher snowlines on glaciers of higher base elevation (cf. Fang et al., 2011). Figure 25 displays increased elevation along the west Peninsula and, in the magnified image, shows the far west central plateau to have higher elevation than the far east. Thirdly, the influence of glacier hypsometry on ELA may be apparent in $SLA_{EOS}$ variability and/or may affect precision of satellite-derived $SLA_{EOS}$. In the Trinity Peninsula, western glaciers have top-heavy or equidimensional hypsometric curves, related to higher ELA, while eastern glaciers have bottom-heavy hypsometric curves, related to lower ELA (Davies et al., 2012). An east-west hypsometry difference may therefore explain higher western $SLA_{EOS}$, due to the relationship of ELA and $SLA_{EOS}$ (Paterson, 1994). A steep elevation increase between the terminus and ELA characterises top-heavy hypsometry; this is visible along the west Peninsula mean snowline for 2019 (Figure 26a), supporting east-west hypsometric differences claimed in Davies et al. (2012). On steeper western slopes, 30 m Landsat image pixels cover a wider range of elevations; thus, uncertainty in automated $SLA_{EOS}$ detection may be greater for these glaciers and this added uncertainty may contribute to the contrary higher western $SLA_{EOS}$. However, despite asserting higher snowlines in the east, Davies et al. (2012) also illustrates 2006 ELA for Trinity Peninsula glaciers in a figure (adapted into Figure 26b) which, if mid-point ELAs of each glacier in east/west zones are averaged, yields higher mean ELA in the west (518 m) than the east (376 m), in line with $SLA_{EOS}$ spatial trends presented here.

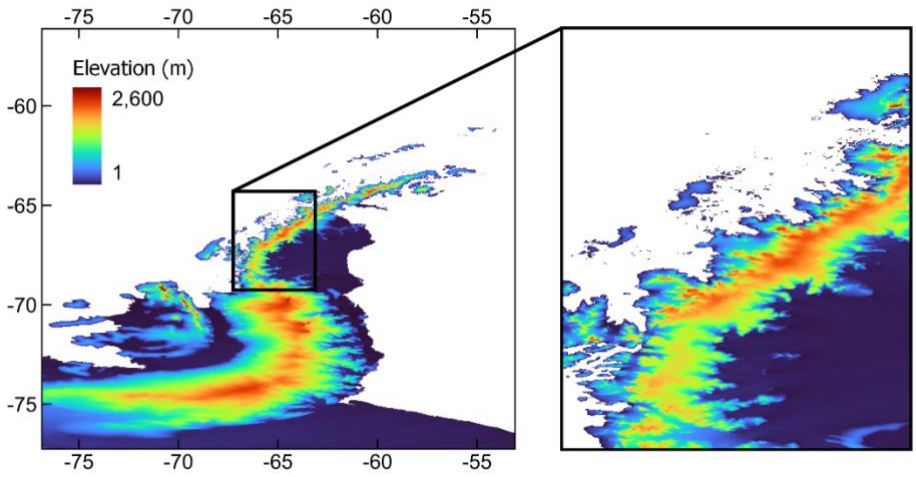


**Figure 25.** Antarctic Peninsula topography derived from AW3D30 (Tadono et al., 2016). Magnified image shows region of elevation increase along inland plateau at ~67˚S, 66˚W; elevation is higher along far west plateau (displayed red) than far east (displayed orange).

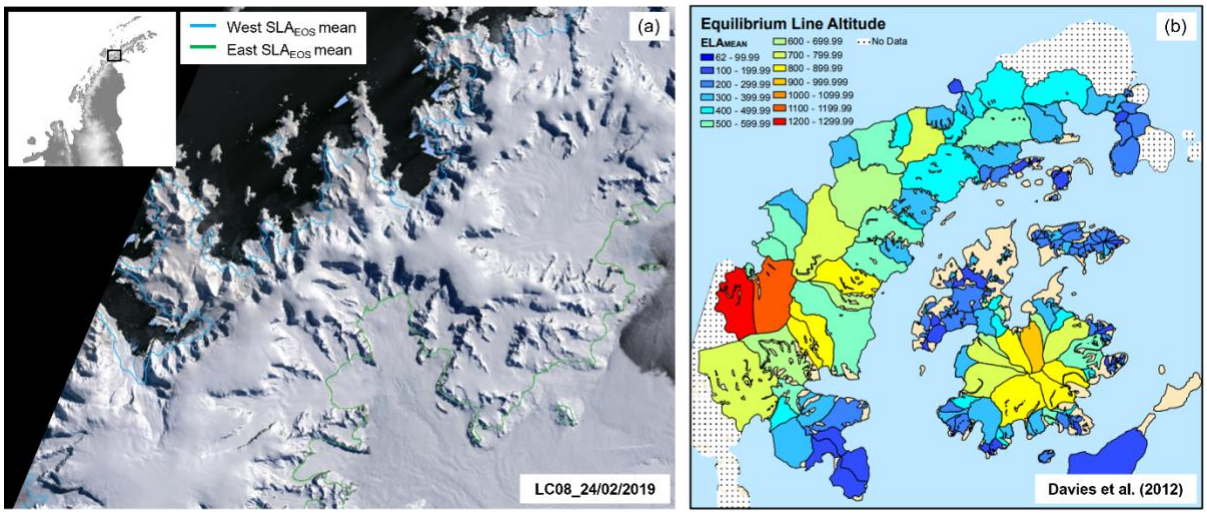


**Figure 26.** East-west comparisons of annual mean SLA$_{EOS}$ and ELA for Antarctic Peninsula sub-regions. (a) Landsat 8 imagery from February 2019 when annual mean SLA$_{EOS}$ was higher in west (blue; 434 m) than east (green; 339 m); western steep slope contrasts with eastern gradual slope here. (b) Davies et al. (2012) figure of 2006 glacier mean ELAs on Trinity Peninsula and James Ross Island; visual interpolation of mid-point ELA yielded higher mean in west (518 m) than east (376 m).

### *5.1.3. Andes*

The overall decline in SLA$_{EOS}$ with increasing Andean latitude (Figure 20), is corroborated by findings of Saavedra et al. (2017). The trend reflects dominant control of terrain elevation on snowline elevation (cf. Fang et al., 2011) and ELA (cf. Carrivick and Chase, 2011), coupled with lowering relief from ~4000 m a.s.l. (Tropical and Central Andes) to ~1000 m a.s.l. (Southern Andes) (Saavedra et al., 2017). Abrupt SLA$_{EOS}$ declines at ~37˚S and ~52˚S align with regions of rapid elevation decline (Figure 27).

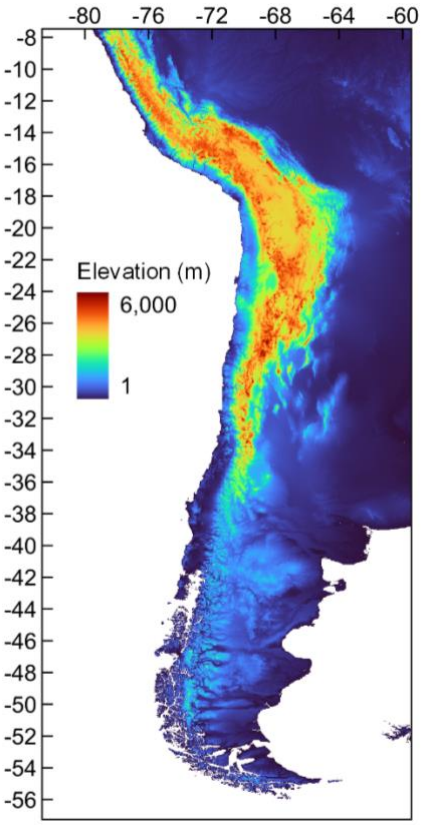


**Figure 27.** Andes topography derived from AW3D30 (Tadono et al., 2016). Elevation declines at 37˚S and 52˚S, corresponding to regions of $SLA_{EOS}$ decline.

In the northernmost Andes (Tropical and Central), annual mean $SLA_{EOS}$ was higher overall for western glaciers than for eastern glaciers; however, this trend was reversed for the southernmost Andes (Central Chilean and Southern) (Figure 21). This spatial variability is ascribed to changing direction of east-west precipitation gradients with increasing latitude. For the Tropical and Central regions, north of ~23-29˚S, moisture transport primarily originates in the Atlantic and circulates easterly towards the Andes, where the topographic barrier prevents moisture transport to western glaciers (Garreaud, 2009; Masiokas et al., 2020). Simultaneous circulation of cool, dry air from the Pacific maintains western aridity, resulting in the east-west precipitation gradient which contrasts greatest between the Atacama Desert and Chaco wetlands, Central Andes (Garreaud, 2009); this trend is upheld in ERA5-Land data (Figure 23). South of 29˚S, Pacific moisture transport becomes more prominent (Masiokas et al., 2020), though from 29-35˚S the east-west precipitation contrast is reduced (Viale et al., 2019; Figure 23), as easterly circulation becomes more dominant in summer (Viale and Garreaud, 2014). South of 35˚S, strong westerly circulation delivers high quantities of precipitation to western glaciers, enhanced by orographic effects which minimise precipitation delivery to the east (Garreaud, 2009; Viale et al., 2019). However, despite being well-documented in research, this trend was not presented by reanalysis snowfall data (Figure

23). As $SLA_{EOS}$ lowers with increased snowfall, reduced eastern $SLA_{EOS}$ in the Tropical and Central Andes, and reduced western $SLA_{EOS}$ in the Southern Andes, is as expected. Substantially increased eastern $SLA_{EOS}$ in the Central Chilean region contradicts precipitation trends; the variability may instead reflect considerably higher minimum elevation of eastern glaciers (mean = 4099 m a.s.l.) compared to western glaciers (mean = 3219 m a.s.l.) here.

## 5.2. Temporal variability in $SLA_{EOS}$

### *5.2.1. Southern Alps*

The mean rate of $SLA_{EOS}$ rise for the entire Southern Alps region from 2000-2020 (2.19 m $yr^{-1}$; Figure 15a) was not statistically distinct from the mean rate of $SLA_{EOS}$ rise calculated for the smaller sample of Southern Alps test glaciers (2.54 m $yr^{-1}$; Figure 14), which are index glaciers in the New Zealand aerial snowline survey. This comparison evidences that index glaciers used in the aerial survey are suitably representative of the entire Southern Alps, due to their distribution along north-south and east-west transects of the range (Chinn, 1995).

In each sample, rates of $SLA_{EOS}$ rise are aligned with findings of global mountain glacier and snow cover deterioration (Hock et al., 2019) along with anthropogenically-driven warming (Fitzharris, 2007) which is identifiable in reanalysis data for the Southern Alps (Figure 23a). Despite the trend direction being as expected, the magnitude of Southern Alps $SLA_{EOS}$ rise calculated here is less than a third of the magnitude of $SLA_{EOS}$ rise calculated by the aerial survey (7.04 m $yr^{-1}$; Figure 14). Due to the similarity of automated results in Figures 14 and 15, this discrepancy is highly unlikely to be related to the different glacier samples used. Rather, it may be associated with timings of $SLA_{EOS}$ retrieval in each method because, due to strong spatial variability in climate over New Zealand (Ackerley et al., 2012), the summer date at which annual maximum snowline is reached is likely to differ for glaciers across the region. Although the automated method is restricted to identifying $SLA_{EOS}$ on dates of satellite image availability, it offers the opportunity of filtering through multiple images to find the date at which SLA was maximal for a specific glacier. In contrast, the aerial survey identifies $SLA_{EOS}$ on the same date for all glaciers, and this date is restricted to days with suitable flight conditions (Chinn, 1995). Premature $SLA_{EOS}$ identification – thus, mean $SLA_{EOS}$ underestimation – is possible under both methods; however, survey-derived $SLA_{EOS}$ was lower than automated $SLA_{EOS}$ in most (14 of 21) years, particularly early in the study period (Figure 14). If these results are underestimations of mean $SLA_{EOS}$ caused by surveying earlier than the true 'end-of-summer' date for multiple glaciers, the true magnitude of Southern Alps $SLA_{EOS}$ rise is likely closer to the value of 2.19 m $yr^{-1}$ presented here.

Temporal variability of Southern Alps $SLA_{EOS}$ (Figure 15a) and $SLA_{EOS}$ anomaly (Figure 16a) corresponds well with previously documented variations in Southern Alps glacier advancement and

retreat. Mackintosh et al. (2017) reported that many Southern Alps glaciers were advancing between 1983 and 2008 during a period of reduced air and sea surface temperature (SST), and that recent glacier mass loss likely began with rapid retreat of Fox and Franz Josef glaciers from 2011. In parallel, this study identifies that Southern Alps mean $SLA_{EOS}$ generally declined from 2000-2008 and increased thereafter (Figure 15a), and that $SLA_{EOS}$ anomaly was consistently positive since 2011 (Figure 16a). Averaging of these retreat and advance phases across the 21-year period explains the yielding of a relatively small overall rate of $SLA_{EOS}$ rise regionally. Further, this comparison of $SLA_{EOS}$ and terminus position trends highlights the short lag time (between 2008 and 2011) in glacier retreat, during which glacier dynamics adjust to the change in mass balance and prompt a response at the terminus (Leysinger Vieli and Gudmundsson, 2004). In turn, this fast response time demonstrates high sensitivity of Southern Alps glaciers to climate change, which is expected in a maritime climate (Kirkbride and Winkler, 2012).

On an inter-annual scale, Southern Alps mean $SLA_{EOS}$ was maximum in year 2000, before it was exceeded in 2013 and further in 2016 (Figure 15a). Correspondingly, previous simulation demonstrated that year 2000 had the most negative Southern Alps mean mass balance on record from 1972-2011, with such patterns attributed to positive temperature anomalies (Mackintosh et al., 2017) enhancing ablation in the 1999/2000 summer; similarity in these findings supports the surrogacy of glacier $SLA_{EOS}$ for mass balance. The 2016 peak in $SLA_{EOS}$ can also be explained climatically. A strong El Niño is widely reported for the Southern Hemisphere 2015/2016 summer (Cai et al., 2020; Bodart and Bingham, 2019; Vera and Osman, 2018). Over New Zealand, air temperatures > 1.2˚C above summer average were recorded (NIWA, 2016) and the neighbouring Tasman Sea experienced an extreme and prolonged marine heatwave (Oliver et al., 2017). Southern Alps mean $SLA_{EOS}$ is likely to have risen in parallel with increased SSTs, as previous studies report strong association between these variables in this region (Clare et al., 2002; Lorrey et al., 2022), likely arising from the maritime setting (Oerlemans and Reichert, 2000). The 2015/2016 El Niño also brought excessive precipitation to the West Coast and Tasman zones (NIWA, 2016), but due to warm temperatures this may have fallen as rain, as ERA5-Land simulations corroborate low summer snowfall for 2016 (Figure 23a). Alongside increased temperatures, increased rainfall could have aided ablation by delivering a heat flux which increased energy available for melt (Gillett and Cullen, 2010). This combination of climatic factors aids justification of the maximum Southern Alps $SLA_{EOS}$ anomaly in 2016 (Figure 16a). Contrastingly, the 2013 peak in $SLA_{EOS}$ is likely a consequence of the limited glacier sample, illustrated by the larger S.E. (Figure 15a). There were no cloud-free Landsat images available for the Mount Aspiring region (south-west) in the 2013 end-of-summer period, resulting in an elevation bias in the glacier sample used to calculate mean $SLA_{EOS}$, which consisted mainly of glaciers in the higher altitude Mount Cook region. Therefore, peak $SLA_{EOS}$ in 2013 should be regarded as a probable overestimation.

*5.2.2. Antarctic Peninsula*

Antarctic Peninsula mean $SLA_{EOS}$ increased significantly at 3.74 m $yr^{-1}$ from 2000-2020 (Figure 15b). Alongside consistency with findings of global snow cover decline (Hock et al., 2019), this value is aligned with overall trends of terminus retreat (Davies et al., 2012; Seehaus et al., 2018; Silva et al., 2020) and negative mass balance (Marinsek and Ermolin, 2015; Rott et al., 2018) displayed by Antarctic Peninsula glaciers during this period. As shown in ERA5-Land data (Figure 23b), the Antarctic Peninsula experienced overall cooling from the late 1990s to mid-2010s (Oliva et al., 2017; Turner et al., 2016), followed by warming to 2020 (Carrasco et al., 2021). It was anticipated that the well-reported temperature sensitivity of these glaciers (Abram et al., 2013; Davies et al., 2014; Navarro et al., 2013) would be highlighted in $SLA_{EOS}$ results, however temporal variability in regional mean $SLA_{EOS}$ does not bear strong resemblance to documented cooling and warming trends; a breakpoint in the $SLA_{EOS}$ trend may be expected in the mid-2010s, but this is not visible. Instead, results imply that $SLA_{EOS}$ rise accelerated from 2011 (Figure 15b), with consistently positive $SLA_{EOS}$ anomaly from 2017 (Figure 16b). Disparity between patterns in regional $SLA_{EOS}$ and temperature trends could indicate the slower glacier response times that might be expected in a cold sub-polar climate (Raper and Braithwaite, 2009), or the averaging of $SLA_{EOS}$ over a wide sample of both physically and climatically diverse glaciers.

Antarctic Peninsula mean $SLA_{EOS}$ and $SLA_{EOS}$ anomalies were particularly high in 2018, and particularly low in 2001 and 2011 (Figures 15b and 16b). Although dry snowline altitude differs to $SLA_{EOS}$ by marking the minimum perennial snow cover elevation, there may be similarities in the temporal variability of these parameters in the Antarctic Peninsula, as dry snowlines were also especially low in the 2010/2011 summer (Zhou et al., 2022). Falk et al. (2016) reported ELA of 250 m a.s.l. on King George Island for the 2010/2011 summer, which is also aligned with the finding of lower mean $SLA_{EOS}$ (300 ± 17 m a.s.l.) for the Antarctic Peninsula this year. The lower dry snowline and ELA are both attributed to a wide-spread positive precipitation anomaly and lack of suitable snow ablation temperatures in the 2010/2011 summer (Falk et al., 2016; Zhou et al., 2022); thus, the simultaneously low $SLA_{EOS}$ was likely driven by the same increase in net accumulation. Correspondingly, weather station data display a decline in median precipitation and precipitation anomaly for the region in 2018 (Carrasco and Cordero, 2020), aligning with the peak $SLA_{EOS}$ and $SLA_{EOS}$ anomaly in 2018 (Figures 15b and 16b), which was unlikely a reflection of temperature variability as summer temperature anomaly was below average this year (González-Herrero et al., 2022). As years of higher and lower Antarctic Peninsula $SLA_{EOS}$ are comparable to periods of above or below average precipitation, there is a possibility that these glaciers are more sensitive to precipitation variability than previously acknowledged. However, this theory requires further $SLA_{EOS}$ evidence at the scale of ground-based weather data, which cannot be provided by regional-average $SLA_{EOS}$ results presented with this method.

*5.2.3. Tropical Andes*

The Tropical Andes experienced the greatest overall $SLA_{EOS}$ change from 2000-2020, at a significant rate of 6.28 m $yr^{-1}$ (Figure 15c). This result supports multiple findings of rising snowlines in the Peruvian Andes (Hanshaw and Bookhagen, 2014; López-Moreno et al., 2014; McFadden et al., 2011; Rabatel et al., 2012; Veettil and Simões, 2019; Veettil et al., 2016a; Veettil et al., 2017), as well as recent findings of declining snow cover area in this region (Calizaya et al., 2023). This change is attributed to significant warming of the Tropical Andes in recent decades (Russell et al., 2017; Vuille et al., 2015), as inter-annual variability in Tropical Andes SLA was previously linked to inter-annual variability in air temperature (Masiokas et al., 2020).

Despite this finding, the high cloud probability (Figure 10) and small mean sample size (36) of this region means there is greater opportunity for annual $SLA_{EOS}$ results to be influenced by the average topography of glaciers within the annual sample, and this is reflected in relatively large S.E. of annual $SLA_{EOS}$ results for this region (Figure 15c). As the larger S.E. influences our confidence in results, doubt could be placed on the overall $SLA_{EOS}$ trend and finding of maximum rate of $SLA_{EOS}$ rise in this region. However, the rate of 6.28 m $yr^{-1}$ $SLA_{EOS}$ change is within previous estimates of SLA change for Tropical Andes glaciers; for instance, Nevado Champara snowline rose by ~39 m from 2002-2017 (2.6 m $yr^{-1}$) and by ~48 m from 2011-2016 (9.6 m $yr^{-1}$) (Veettil and Simões, 2019), and Artesonraju Glacier snowline rose by ~200 m from 2000-2010 (20 m $yr^{-1}$) (Rabatel et al., 2012).

The rate of mean $SLA_{EOS}$ change for the Cordillera Blanca (within the Tropical Andes) was calculated as 4.79 m $yr^{-1}$ from 2000-2020 (Figure 17), which is closer to the rate of southern Cordillera Blanca snowline rise identified in Veettil et al. (2017) (~98 m from 1984-2015, or 3.2 m $yr^{-1}$). The increased rate of $SLA_{EOS}$ rise identified in this study is partly credited to the more recent period observed, as rates of Tropical Andes glacier change are thought to have increased with time (Rabatel et al., 2013). The variance is also credited to the different glacier samples used; Veettil et al. (2017) studied snowline changes for eight glaciers in one southern site of the cordillera, but here $SLA_{EOS}$ of a given year was calculated from an average of 29 glaciers spread across the cordillera. This difference implies that $SLA_{EOS}$ change is reduced in the southern Cordillera Blanca, contrary to glacier area change reports in Burns and Nolin (2014).

The inter-annual variability in Tropical Andes $SLA_{EOS}$ anomaly corresponds with previous estimations of snow cover variation and ENSO phase variation for this region. The most positive $SLA_{EOS}$ anomalies occurred in 2010, 2014 and 2016 (Figure 16c); Calizaya et al. (2023) similarly found that the time series trend of maximum snow cover area for glaciers in the Alto Santa basin of Peru declined in each of these years. Previous research has identified ENSO anomalies as the most reliable predictor of snow persistence in the Andes north of 31˚S (Saavedra et al., 2018). As such, it is likely that ENSO influence is reflected in $SLA_{EOS}$ anomalies, as the especially warm and dry conditions of a Tropical Andes El

Niño event (Masiokas et al., 2020; Vuille et al., 2018) were present in the strong El Niño years of 2010 and 2016 (Imfeld et al., 2020). Temperatures were sufficient to enhance ablation and, coupled with reduced snowfall (Figure 23c), higher mean snowlines were attained. Year 2014 was an exception to this trend, as it was a wet La Niña summer for the Peruvian Andes (Poveda et al., 2020). Although ERA5-Land data does not show abnormally high summer air temperatures in 2014 (Figure 23c), Vicente-Serrano et al. (2018) showed that March average air temperature over Peru peaked in 2014 similarly to its peak during the 2010 El Niño. As temperature is likely the primary control on SLA variability in this region (Masiokas et al., 2020), where glaciers undergo prolonged exposure to strong solar irradiance (Calizaya et al., 2023), the high $SLA_{EOS}$ of 2014 supports the idea that ablation drivers exceeded accumulation drivers in this case. As expected, several other La Niña events instead aligned with years of negative $SLA_{EOS}$ anomaly – namely, 2001, 2002, 2006, 2009, 2012 and 2013 (Veettil et al., 2014). Correspondingly, annual precipitation at Recuay station, Cordillera Blanca, peaked in 2001, 2006 and 2009 (Schuawecker et al., 2014), supporting findings of lower mean $SLA_{EOS}$ in these years (Figures 15c and 16c).

*5.2.4. Central Andes*

Compared to the Tropical Andes, Central Andes $SLA_{EOS}$ increased at a lower and insignificant rate (4.38 m $yr^{-1}$; Figure 15d) from 2000-2020. There was no clear overall trend in $SLA_{EOS}$ anomaly, but anomalies were consistently positive from 2016-2020 (Figure 16d). The overall $SLA_{EOS}$ trend is consistent with previous findings of SLA rise for individual glaciers and cordilleras within this region (Hanshaw and Bookhagen, 2014; López-Moreno et al., 2014; Veettil and Simões, 2019; Veettil et al., 2016a; Veettil et al., 2016b). This is aligned with reported warming of this outer-tropical zone at high altitudes (Russell et al., 2017; Vuille et al., 2015) which is reproduced in ERA5-Land reanalysis (Figure 23d). The reduced rate of $SLA_{EOS}$ rise in the Central Andes compared to lower latitudes also aligns with the increased rate across the Cordillera Blanca compared to the higher latitude Cordillera Vilcanota (2.84 m $yr^{-1}$; Figure 17).

The rising mean $SLA_{EOS}$ of the Cordillera Vilcanota was of similar magnitude to the rising median glacier elevation within the cordillera from 2000-2020. Taylor et al. (2022) calculated median glacier elevation, used as a proxy for ELA, for glaciers in the north, central, east, and southeast of Cordillera Vilcanota from 1975-2020; the mean rate of ELA change from 2000-2020 was 2.49 m $yr^{-1}$ according to these values – only 0.35 m $yr^{-1}$ smaller than the estimated rate of $SLA_{EOS}$ rise for this sub-region (Figure 17). Despite lack of significant correlation between either $SLA_{EOS}$ or ELA and precipitation variability (Taylor et al., 2022), the three years displaying minimum mean $SLA_{EOS}$ for Vilcanota (2001, 2006, and 2012) were also years with maximum summer precipitation (Imfeld et al., 2020). To concur, Favier et al. (2004) and Veettil et al. (2016b) document high dependence of inter-annual variability in outer-tropical mass balance and ablation on the inter-annual variability of summer precipitation caused by

atmospheric circulation anomalies (Vuille et al., 2000). However, minimum peaks in $SLA_{EOS}$ could also be explained by negative maximum summer air temperature anomalies during these years (Imfeld et al., 2020), supporting the view that temperature predominantly drives inter-annual ELA variability in this region (Taylor et al., 2022). Contrary to this view, higher mean $SLA_{EOS}$ only corresponds with positive maximum summer air temperature anomalies in 2006 and 2016 (Imfeld et al., 2020). In 2009, Cordillera Vilcanota climate was within average, apart from marginally negative temperature anomalies (Imfeld et al., 2020) with which lower $SLA_{EOS}$ was anticipated; the larger S.E. of $SLA_{EOS}$ in this year (Figure 17), due to small glacier sample size, supports likely overestimation of the 2009 result.

There is also high inter-annual variability in the overall Central Andes $SLA_{EOS}$ trend. Multiple short periods of snowline lowering (particularly 2004-2006, but also 2013-2015 and 2016-2018; Figure 15d) partly correspond with the negative SLA trend at Zongo Glacier, Bolivia, from 1996-2006 (Rabatel et al., 2012). As with the Tropical Andes, $SLA_{EOS}$ variability is seemingly linked with ENSO fluctuations; for instance, Central Andes mean $SLA_{EOS}$ was minimal in 2001, indicating the La Niña event which brought the lowest maximum and minimum summer air temperatures and third-highest summer precipitation quantity of the period 2000-2017 (Imfeld et al., 2020). Conditions were similar during the 2011 La Niña year (Imfeld et al., 2020; Figure 23d), when $SLA_{EOS}$ reached a second minimum peak (Figure 15d). Confidence in these results arises from their smaller S.E., and from similarity to snowline trends identified in Veettil et al. (2016b), which demonstrated SLA of two Central Andean study sites to fall in 2001 and 2011. This study also found that SLA at one site rose rapidly in 2003, similar to the trend in Figure 15d. In 2003, ENSO was in a warm and dry phase; simultaneously, the Pacific Decadal Oscillation (PDO) was in its most positive phase of the period 2000-2015 (Veettil et al., 2016b). As previous studies have suggested that in-phase combination of these modes (i.e., El Niño/positive PDO and La Niña/negative PDO) lead to increased magnitude of ENSO effects on climate (cf. Kim et al., 2014) and snowlines (Veettil et al., 2016b), the finding of maximum Central Andes $SLA_{EOS}$ during a relatively extreme positive phase of PDO is supported.

*5.2.5. Central Chilean Andes*

The rise in Central Chilean Andes mean $SLA_{EOS}$ was significant over the period 2000-2020 at a rate of 5.95 m $yr^{-1}$ (Figure 15e), displaying a strong positive trend in $SLA_{EOS}$ anomaly compared to other Andean regions (Figure 16). This is aligned with documented snowline rise for the Chilean Andes in Saavedra et al. (2018), as well as findings of glacier minimum elevation rise (Malmros et al., 2016), summer snow cover decline (Cordero et al., 2019), and glacier mass loss (Dussaillant et al., 2019) in recent decades. Additionally, Saavedra et al. (2018) reported snowline rise at 10-30 m $yr^{-1}$ south of 29-30˚S; although the calculated Central Chilean mean $SLA_{EOS}$ rate of rise was lower, the rates defined in Saavedra et al. (2018) approximately correspond to $75^{th}$ and $99^{th}$ percentiles of our data for this region (9.75 and 39.8 m $yr^{-1}$, respectively). The increased rate of mean $SLA_{EOS}$ rise in the Central Chilean

region compared to the Central region (Figure 15) also corresponds to the increased rate of precipitation decline in the mid-latitude Andes compared to the lower-latitude Andes (Saavedra et al., 2018). An extreme drying trend, termed 'mega-drought' in Garreaud et al. (2020), has persisted across the Central Chilean region since 2010, causing accelerated glacier thinning (Farías-Barahona et al., 2020), declined snow persistence (Masiokas et al., 2020), and early-summer snowline rise (Garreaud et al., 2017). The precipitation reduction is visible in ERA5-Land summer snowfall estimates (Figure 23e). This study finds that rate of Central Chilean mean $SLA_{EOS}$ rise more than doubles between periods 2000-2010 (3.74 m $yr^{-1}$) and 2010-2020 (8.13 m $yr^{-1}$) which, like previous studies, is assigned to reduced snow accumulation brought about by recent and ongoing drought (Garreaud et al., 2020).

Central Chilean mean $SLA_{EOS}$ and $SLA_{EOS}$ anomaly were high in 2009, 2015, and 2018, and lowest in 2003 (Figures 15e and 16e). Concurrently, for a study across the mid-latitude Andes from 2000-2015, summer snow extent was maximum in 2003, while 2009 and 2015 were in the top four years of minimum snow extent for the 34-40˚S region (Cordero et al., 2019). The low $SLA_{EOS}$ and maximum snow extent of 2003 corresponds to an El Niño period (Cordero et al., 2019) which, unlike in the Tropical and Central regions at lower latitude, is associated with anomalously warm temperatures and high snowfall south of 29˚S (Masiokas et al., 2006; Rivera et al., 2017). As 2003 $SLA_{EOS}$ was minimum despite warm El Niño, it is suggested that precipitation variability had a greater influence over $SLA_{EOS}$ variability. This corroborates the view that precipitation is the primary forcing on snow persistence variability (Saavedra et al., 2018) and glacier mass balance variability (Masiokas et al., 2016) in the mid-latitude Andes.

As precipitation variability within 18-40˚S is determined by the SAM as well as ENSO (Cordero et al., 2019), there is uncertainty surrounding relative influence of these large-scale modes on Central Chilean Andes $SLA_{EOS}$ change. SAM is exhibited in latitudinal wavering of maximum westerly winds, and therefore precipitation, over the southeastern Pacific (Garreaud et al., 2013), and has a stronger forcing than ENSO over snow persistence trends south of 35˚S (Saavedra et al., 2018). The Central Chilean $SLA_{EOS}$ highs of 2009 and 2015 are aligned with strongly positive SAM (Cordero et al., 2019), therefore weaker mid-latitude westerlies (Thompson et al., 2011), whilst minimum $SLA_{EOS}$ in 2003 corresponds to strongly negative SAM, therefore stronger westerlies. Contrastingly, inter-annual variability in Central Chilean $SLA_{EOS}$ has less overall comparability to variations in ENSO phase from 2000-2015 (Cordero et al., 2019). Therefore, contrary to high correlation of summer snow cover and ENSO from 23-34˚S (Cordero et al., 2019), findings concur increased influence of SAM on glacier change in the Central Chilean region (Saavedra et al., 2018). This suggests that Central Chilean glaciers south of 34˚S dominate the averaged glacier-climate interactions of this region.

*5.2.6. Southern Andes*

This study identified no significant trend in Southern Andes mean $SLA_{EOS}$ (-0.09 m $yr^{-1}$) or $SLA_{EOS}$ anomaly from 2000-2020 (Figures 15f and 16f). However, mean $SLA_{EOS}$ trends were visible for Southern Andes sub-regions; $SLA_{EOS}$ exhibited small increasing trends for the NPI and SPI (2.78 and 1.49 m $yr^{-1}$, respectively) and a decreasing trend for Cordillera Darwin (-3.05 m $yr^{-1}$; Figure 17). These findings demonstrate that ambiguity of the overall Southern Andes $SLA_{EOS}$ trend is an outcome of averaging over regions of $SLA_{EOS}$ rise (e.g., NPI/SPI) and $SLA_{EOS}$ decline (e.g., Cordillera Darwin).

It is understood that there are no works to which NPI, SPI, and Cordillera Darwin $SLA_{EOS}$ change can be directly compared. However, trends are aligned with reports of recent decline in glacier and snow cover extent in the Patagonian icefields (Barcaza et al., 2017; Masiokas et al, 2020; Pérez et al., 2018), and the contrast of ELA lowering in the Punta Arenas region (neighbouring Cordillera Darwin) to ELA rise in Patagonia (Carrasco et al., 2008). Rising mean $SLA_{EOS}$ of Patagonian icefields also concurs accelerated shrinkage of mountain glaciers north of 52˚S from 2001 (Davies and Glasser, 2012). Likewise, lowering of Cordillera Darwin mean $SLA_{EOS}$ concurs decelerated shrinkage of outlet glaciers and ice caps south of 54˚S over recent decades, with the portion of shrinking glaciers decreasing from 77.5% (1870-1986) to 31.8% (2001-2011) (Davies and Glasser, 2012). The indication that stable and growing glaciers dominated over shrinking glaciers at high Andean latitudes from 2001-2011 supports the overall $SLA_{EOS}$ lowering at Cordillera Darwin from 2000-2020. Rates of $SLA_{EOS}$ change across the NPI, SPI, and Cordillera Darwin decline with increased latitude, in line with the pattern across all five Andean sub-regions (Figure 17). The reduced rate of $SLA_{EOS}$ rise in the SPI compared to the NPI corresponds to reports of SPI glaciers displaying neutral or positive mass balance, and/or stable or advancing extents in recent years (Bravo et al., 2019; Masiokas et al., 2020; Minowa et al., 2021; Wilson et al., 2016). Additionally, several studies document increased positivity of SPI surface mass balance compared to the NPI (Mernild et al., 2017; Minowa et al., 2021; Schaefer et al., 2013, 2015). Snowlines are increasingly stable in the higher-latitude Cordillera Darwin, where rate of mean $SLA_{EOS}$ change becomes negative. These trends coincide with growing evidence of increasing precipitation in the high-latitude Southern Andes (Carrasco et al., 2008). This has arisen from southward displacement and intensification of westerlies at ~60˚S following increased SAM index and formation of anomalous low pressure near Drake Passage (Aguirre et al., 2018; Carrasco-Escaff et al., 2023; Thompson et al., 2011). As the Southern Andes has also been experiencing general warming in recent decades (Figure 23f; Aguirre et al., 2018; Carrasco-Escaff et al., 2023; Falaschi et al., 2021; Minowa et al., 2018), findings of minimal rise in NPI and SPI $SLA_{EOS}$ compared to further north, and decreasing $SLA_{EOS}$ in the southernmost Andes (Cordillera Darwin), show that the enhancement of westerlies and snow accumulation at higher latitudes is weakening responses of these glaciers to warming.

Much of the inter-annual variability in overall Southern Andes $SLA_{EOS}$ is consistent with reported variability in glacier change and is concurred in climatic variability. Low $SLA_{EOS}$ mean and negative $SLA_{EOS}$ anomaly of the Southern region (Figures 15f and 16f) and SPI (Figure 17) in 2001 coincides with positive summer precipitation anomaly and negative summer temperature anomaly in the Aysén basin, 45-46˚S (Pérez et al., 2018); these anomalies are also visible in ERA5-Land summer snowfall and temperature trends (Figure 23f). Concurrently, Pérez et al. (2018) documents 2001 as the year of maximum summer snow extent in a Patagonian study region from 2000-2016. Abrupt $SLA_{EOS}$ decline is also identified for NPI, SPI, and Southern Andes trends in 2010/2011 (Figures 15f and 17). This coincides with sudden decrease in frontal ablation rates of SPI glaciers, Upsala and Jorge Montt, in 2010/2011 (Minowa et al., 2018) and is likely explained by positive summer precipitation anomalies during 2009-2011, and coincident negative summer air temperature anomaly in 2010 (Pérez et al., 2018). However, years of highest mean $SLA_{EOS}$ have not always coincided with years of positive (negative) air temperature (precipitation) anomalies. It was anticipated that maximum Southern Andes $SLA_{EOS}$ would be displayed for 2008 and 2016, as ERA5-Land data (Figure 23f) and climate anomaly trends (Pérez et al., 2018) suggest. Instead, these years had positive $SLA_{EOS}$ anomaly, but year 2012 displayed maximum $SLA_{EOS}$ anomaly (Figure 16f). As the 2012 result aligns with relatively high SST anomaly in southernmost South America (Allega et al., 2021; Risaro et al., 2022), the documented relationship between regional warm SST and high $SLA_{EOS}$ (cf. Clare et al., 2002) may have contributed to divergence of $SLA_{EOS}$ findings from air temperature and precipitation trends. Additionally, sensible heat energy flux was greater in 2012 than in 2008 and 2016 for southern Patagonia, and had leading influence over surface mass balance variability from 1996-2020 (Minowa et al., 2022). Altogether, the inter-annual variability in $SLA_{EOS}$ does not solely coincide with air temperature and precipitation anomalies.

### 5.3. Spatio-temporal variability in $SLA_{EOS}$

#### *5.3.1. Southern Alps*

In both the test sample and complete sample of Southern Alps glaciers, the automated method identified increased rates of $SLA_{EOS}$ rise to the east of the Main Divide (Figures 14 and 21a). This supports the claim in Carrivick and Chase (2011) that some of the most negative departures of annual ELA from steady-state ELA (1983-2009) (i.e., greatest ELA lowering) are along the Southern Alps west coast. In contrast, results presented here contradict the New Zealand aerial survey data (Lorrey et al., 2022), which showed increased rates of $SLA_{EOS}$ rise on western index glaciers (Figure 14). Spatio-temporal variability in warming trends (Table 6) supports this study's identification of increased eastern $SLA_{EOS}$ rise, as the mean rate of summer warming over eastern glaciers (0.0569 K $yr^{-1}$) exceeded that over western glaciers (0.0502 K $yr^{-1}$) for the period of 2000-2020. It is conceived that high temperature

sensitivity of Southern Alps glaciers (Lorrey et al., 2022; Mackintosh et al., 2017) is therefore exhibited in $SLA_{EOS}$ spatio-temporal variation identified here. As eastern glaciers are situated in warmer conditions, their response time is expected to be shorter (cf. Raper and Braithwaite, 2009); hence, their increased rates of $SLA_{EOS}$ rise.

The response of Southern Alps $SLA_{EOS}$ to temperature variability was also displayed in Figure 22. Both east and west sub-regions exhibited increased rates of $SLA_{EOS}$ rise during 2010-2020 compared to during 2000-2010, and the magnitude of this increase was elevated for western glaciers. The reduced $SLA_{EOS}$ rise during the earlier decade is concurred by the finding in Mackintosh et al. (2017) that Southern Alps glaciers were generally advancing and gaining mass during a period of SST and air temperature cooling that lasted until 2008. Mackintosh et al. (2017) also highlighted disparity in continuous advancement of west coast glaciers, Fox and Franz Josef, and continuous thinning of the eastern Tasman Glacier. Assuming these localised trends are indicative of the wider east-west contrast, they support the east-west disparity in $SLA_{EOS}$ change rates for 2000-2010 (Figure 22). The increased $SLA_{EOS}$ rise in both sub-regions for 2010-2020 reflects accelerated warming trends associated with increasing positivity of the SAM in recent years (Salinger et al., 2020). Additionally, the greater magnitude of increase in western $SLA_{EOS}$ change rate is attributed to increased frequency of anticyclonic blocking regimes with increasing SAM index (Renwick, 2011). Blocking regimes are associated with reversal of prevailing westerly circulation, causing increased snow accumulation on eastern glaciers and increased snow ablation, via strong downslope winds, on western glaciers (NIWA, 2012; Purdie et al., 2011). Hence, it is proposed that increased SAM index between periods 2000-2010 and 2010-2020 is identifiable in Southern Alps $SLA_{EOS}$ spatio-temporal variation.

Spatial variability in mean $SLA_{EOS}$ change rates may also be explained by spatial variability in Southern Alps glacier topography (Carrivick and Chase, 2011). For instance, results suggested that rates of $SLA_{EOS}$ change were more consistently positive in the northern Southern Alps (Figure 21a), where predominantly north-facing glacier aspects favour increased solar radiation receipt compared to south-facing glacier aspects of the southernmost Southern Alps (Carrivick and Chase, 2011). It may be assumed that solar radiation receipt has increased in the region over recent years as the frequency of summer blocking regimes, linked to increased solar irradiance via cloud cover reduction (cf. Hofer et al., 2017), is dependent on positive SAM (Renwick, 2011), and SAM was increasingly positive from 2000-2019 (Salinger et al., 2020). Thus, $SLA_{EOS}$ spatio-temporal variability suggests glaciers in the northern Southern Alps may be more responsive to effects of positive SAM than southern glaciers, due to aspect differences.

### *5.3.2. Antarctic Peninsula*

The rise in Antarctic Peninsula mean $SLA_{EOS}$ consisted of marginal $SLA_{EOS}$ lowering in the western Peninsula (-0.28 m $yr^{-1}$) and pronounced $SLA_{EOS}$ rise in the eastern Peninsula (5.24 m $yr^{-1}$; Figure 21b).

This increased overall stability of western glaciers is concurred in the Davies et al. (2012) study for Trinity Peninsula, with stability attributed to increased precipitation and the role of equidimensional and top-heavy glacier hypsometries in weakening glacier susceptibility to warming-induced change, whilst cold and dry conditions for steep eastern glaciers enhances susceptibility to change. ERA5-Land presents overall reductions in summer snowfall for both east and west sub-regions (Table 6); however, this trend is not reflected in the literature for the west. Ding et al. (2020) reported that total summer snow days at King George Island, western Antarctic Peninsula, increased by ~14 days per decade from 2001-2014, and Carrasco and Cordero (2020) claimed that westward displacement of the Amundsen Sea Low created southerly winds that favoured increased summer snow over the west post-2001. Hence, it is considered that snowfall trends were likely positive for the west over most of the time period, contrary to ERA5-Land estimates, whilst eastern glaciers remained precipitation-starved. This precipitation variability supports explanation in Davies et al. (2012) for east-west disparities in glacier behaviour, which are also presented here.

It is plausible that east-west contrast is also related to the action of foehn winds in recent years. Foehn wind involves downslope transport of warm and dry air over the lee side of mountains, raising surface temperature and encouraging increased ablation (Turton et al., 2018; Zou et al., 2023). Intensification and southward displacement of westerlies over the Antarctic Peninsula have assisted increased foehn-induced melting in the east (Marshall et al., 2006; Wille et al., 2022). Summer foehn occurrence was also increased from 1999-2018 compared to from 1979-1998 (Laffin et al., 2021), related to strengthening SAM (Cape et al., 2015; Fogt and Marshall, 2020). Thus, as strong westerlies increase western precipitation, and frequency of downslope wind-induced ablation over eastern glaciers increases, the least stable $SLA_{EOS}$ trend is observed in the east (Figure 21b).

However, it should be considered that summer air temperature trends over both east and west sub-regions were negative on average from 2000-2020 (Table 6), with a cooling period from 2000-2014, and rapid warming to present (Carrasco et al., 2021; Figure 23b). This raises questions as to the rising $SLA_{EOS}$ trend in the theoretically temperature-sensitive eastern sub-region, implying that (if temperature has primary control) the eastern $SLA_{EOS}$ signal was either dominated by the post-2014 warming (Figure 23b), or occurred in response to longer-term warming not identifiable in the 2000-2020 timeframe (e.g., Mulvaney et al., 2012). Comparatively, the weakly negative western $SLA_{EOS}$ signal was aligned with overall cooling and, most notably, was declining pre-2014 and rising post-2014 in accordance with temperature variability (Figure 21b). This indicates that the cooling reversal was not reflected in regional $SLA_{EOS}$ (Figure 15b) because the response was spatially diverse (i.e., felt more strongly in the west). Studies have previously asserted that shortened glacier response times, thus heightened glacier sensitivity, exist for relatively warmer, wetter and maritime glacier environments (cf. Kirkbride and Winkler, 2012; Raper and Braithwaite, 2009). These conditions are characteristic of the western Antarctic Peninsula (Figure 23b), especially because maritime periphery islands (e.g., South Shetlands)

constitute a considerable fraction of western glaciers (Figure 4). Therefore, it is possible that $SLA_{EOS}$ results reveal a hyper-sensitive response of western Peninsula glaciers to temperature variability.

Correspondingly, the west displayed a change from negative $SLA_{EOS}$ trend during 2000-2010, to positive $SLA_{EOS}$ trend during 2010-2020 (Figure 22), which is similarly attributed to the mid-2010s cooling reversal (Carrasco et al., 2021; Figure 23b). The change could also reflect reduced frequency of precipitation events during 2010-2020, but the paralleled increasing extremity of precipitation events (Carrasco and Cordero, 2020) makes precipitation variability a less likely driver of the $SLA_{EOS}$ trend. In comparison, the east showed a less positive $SLA_{EOS}$ trend during 2010-2020 than during 2000-2010 (Figure 22). This finding does not support available climate data; summer temperatures rose post-2014 (Figure 23b) and foehn occurrence was likely increasing with positive SAM (Laffin et al., 2021), so an accelerated eastern $SLA_{EOS}$ trend was anticipated. There was a shortage of valid eastern $SLA_{EOS}$ annual means during 2000-2010 (Figure 21b), placing doubt on the accuracy of the 2000-2010 rate of $SLA_{EOS}$ change. This highlights the importance of chosen timeframes in calculation of $SLA_{EOS}$ change rates; for instance, comparing trends of east $SLA_{EOS}$ change from periods 2000-2009 and 2010-2020 would likely yield different results (Figure 21b). The present study maintained equal division of the 2000-2020 timeframe into two time periods, but consideration should be taken herein for interpreting the wider context of these trends.

Spatio-temporal variability in mapped rates of $SLA_{EOS}$ change was particularly strong over the Antarctic Peninsula compared to other Southern Hemisphere regions (Figure 21b). However, there is some resemblance to overall east-west trends. In the north (~64˚S, 60˚W), for instance, northern glaciers displayed $SLA_{EOS}$ lowering and southern glaciers displayed $SLA_{EOS}$ rise (Figure 21b). This was likely also a result of aforementioned variability in temperature, precipitation and wind-induced melt. In the south, an east-west difference was less visible; spatial variability in $SLA_{EOS}$ change rates arises from sparse distribution of sampled glaciers, meaning tessellation bins in the figure presented the average of fewer glaciers or, in many cases, a singular glacier (Figure 21b).

### *5.3.3. Tropical Andes*

The rise in Tropical Andean $SLA_{EOS}$ from 2000-2020 occurred at similar rates for east and west sub-regions – 7.55 and 6.10 m $yr^{-1}$, respectively (Figure 21c). This similarity corresponded to similarity in warming rates over east and west glaciers for the period (Table 6). The marginally stronger signal in eastern $SLA_{EOS}$ rise could also be resolved in the mapped spatio-temporal variability of $SLA_{EOS}$, which presented a positive west-to-east gradient in $SLA_{EOS}$ change over central Peru (Figure 21c). As eastern glaciers are of lower elevation (Kaser and Georges, 1997) and have lower snowlines (Figure 21c, McFadden et al., 2011), the spatio-temporal trend may have resulted from the more pronounced response of low-altitude glaciers and snow cover to regional warming (Hock et al., 2019; Vuille and

Bradley, 2000). For instance, Seehaus et al. (2019) demonstrated that low-altitude Peruvian glaciers experienced increased surface lowering.

Aside from this explanation, the variability identified here is not well supported across the limited literature. McFadden et al. (2011) identified accelerated snowline rise on western slopes of Cordillera Huayhuash and Cordillera Raura, central Peru, whilst Seehaus et al. (2019) also identified accelerated glacier surface lowering on western slopes of Cordillera Blanca. Snow accumulation is typically greater in the east Tropical region, as prevailing easterly circulation encourages orographically enhanced precipitation to the east and limits precipitation delivery in the west (Kaser and Osmaston, 2002; Garreaud, 2009). Together with the ERA5-Land estimate of increased rates of snowfall reduction over western glaciers (Table 6), reported precipitation variability places doubt on the contradictory finding of increased eastern $SLA_{EOS}$ rise.

Three possible contributors to this contradiction are proposed. Firstly, insufficient data to calculate 17 of the annual $SLA_{EOS}$ means for eastern glaciers likely reduced accuracy of the overall $SLA_{EOS}$ change rate, potentially resulting in its overestimation. The eastern Tropical Andes had a notably small sample size, and increased cloud probability (Figure 10) restricted end-of-summer image availability for this limited sample. Secondly, the contradiction to previous findings could be attributed to different observation periods used; periods were 1986-2005 in McFadden et al. (2011) and 2013-2016 in Seehaus et al. (2019). Although a direct comparison to Seehaus et al. (2019) results cannot be made due to this study's lack of data for the eastern Tropical Andes, Figure 21c suggests that western $SLA_{EOS}$ increased rapidly compared to the eastern $SLA_{EOS}$ trend, when only the period 2013-2016 is considered. Hence, the importance of chosen timeframes is again stressed, for their ability to alter overall findings. Thirdly, it is possible the contradiction is related to the reversal of prevailing precipitation variability during El Niño events. El Niño is associated with a tropical Pacific SST anomaly which induces strong westerly flow over the Tropical Andes, increasing (decreasing) western (eastern) precipitation delivery (Vuille et al., 2008); hence, its potential to hamper the rising mean $SLA_{EOS}$ of western glaciers.

The rate of western $SLA_{EOS}$ rise also declined between periods 2000-2010 and 2010-2020 (Figure 22). This supports research in López-Moreno et al. (2017) which identified a reduction in rate of ice loss in a west-draining catchment of Cordillera Blanca, from 0.05 $km^2\ yr^{-1}$ (1985-1998) to 0.02 $km^2\ yr^{-1}$ (2004-2013); though, difference in observation periods limits suitable comparison. For the time period 2010-2019, which is similar to that in which western $SLA_{EOS}$ rise decelerated, the rate of ice loss in a Columbian catchment (~6.5˚S) was halved compared to the period 1994-2010 (López-Moreno et al., 2022). In the former study, deceleration of glacier change was attributed to increasing precipitation and decreasing temperature trends for the region throughout the 21$^{st}$ century (López-Moreno et al., 2017). ERA5-Land does not identify enhanced precipitation reduction between the studied decades, but it does concur a decrease in the rate of warming from 0.08 K $yr^{-1}$ to 0.05 K $yr^{-1}$ (Figure 23c), which likely

reduced total energy available for ablation and caused lower $SLA_{EOS}$. López-Moreno et al. (2022) alternatively attribute part of the deceleration in glacier change to glaciers' gradual restriction to high elevations, where it is assumed climatic conditions are more favourable for temporary equilibrium-state conditions. Although this study considers glacier snowline changes rather than ice loss, and although neither previous study is both spatially and temporally comparable, both explanations offered in these works support the finding of declining rates of $SLA_{EOS}$ rise in the western Tropical Andes.

*5.3.4. Central Andes*

The rise in Central Andes mean $SLA_{EOS}$ from 2000-2020 occurred at an increased rate for eastern glaciers (4.52 m $yr^{-1}$) compared to western glaciers (3.88 m $yr^{-1}$; Figure 21d). Although these rates were not vastly dissimilar, there was a clear east-west variation in the mapped rates of $SLA_{EOS}$ rise across the region (Figure 21d). This finding was surprising, due to prevailing easterly direction of moisture transport to the region (Garreaud, 2009), which makes for a stark east-to-west decline in precipitation sums in most years (Figure 23d). Despite this, the spatio-temporal variability in $SLA_{EOS}$ is in agreement with previous research over the Central Andes. Veettil et al. (2018) found eastern glaciers of Cordillera Urubamba (~13˚S) to have retreated faster than those in the west from 1985-2015. Similarly, northeastern Cordillera Vilcanota glaciers had been shrinking faster than those in the southwest from 1975-2015 (Veettil and de Souza, 2017).

The increased rate of eastern $SLA_{EOS}$ rise may be explained by both topographic and climatic factors. It is thought that elevation dependency of ablation may have influenced the relative stability of western $SLA_{EOS}$, as was previously considered for the western Tropical Andes. Rabatel et al. (2013) identified that glaciers in this region with maximum elevation < 5400 m a.s.l. had a mass loss rate which was double that of glaciers > 5400 m a.s.l.. Concurrently, Hanshaw and Bookhagen (2014) found that Cordillera Vilcanota glaciers with median elevation ~5200 m a.s.l. were retreating ~0.96 m $yr^{-1}$ faster than glaciers with median elevation ~5400 m a.s.l.. Comparably, $SLA_{EOS}$ at eastern Central Andes glaciers (mean elevation: 5265 m a.s.l.) rose 0.64 m $yr^{-1}$ faster than higher western Central Andes glaciers (mean elevation: 5633 m a.s.l.).

Additionally, it is likely that changing precipitation variability is influencing spatio-temporal $SLA_{EOS}$ variability. Despite continued easterly moisture transport, monitoring of southern Peruvian Andes summer precipitation trends from 1965/66 to 2017/18 has shown that precipitation is increasing for the west and decreasing for the east (Imfeld et al., 2020). These trends are related to strengthening westerly flow (Neukom et al., 2015), and would explain increased stability of western $SLA_{EOS}$ from 2000-2020 (Figure 21d). ERA5-Land estimates contradict these climate trends in Table 6; however, under inter-decadal analysis, ERA5-Land shows western glaciers were both drying and warming at a faster rate during 2000-2010, whilst eastern glaciers were warming at a faster rate during 2000-2010 and drying at a faster rate during 2010-2020. This variability supports the positive-to-negative shift in rate of

$SLA_{EOS}$ change for western glaciers between periods 2000-2010 and 2010-2020, along with the simultaneous increase in rate of $SLA_{EOS}$ rise for eastern glaciers (Figure 22). These findings suggest the action of easterly trade winds is more prominent in the earlier decade, when orographically increased (reduced) precipitation delivery to eastern (western) glaciers increased the stability of eastern $SLA_{EOS}$ relative to western $SLA_{EOS}$ (Figure 22). This supplies evidence to the hypothesis of reducing summertime frequency of easterly wind anomalies over the region (Thibeault et al., 2012). Additionally, the coincidence of increased rate of eastern $SLA_{EOS}$ rise with reduced rate of warming in the period 2010-2020, suggests that precipitation variability was a primary factor in eastern glacier changes, in line with views in previous works for this outer-tropical region (Francou et al., 2003; Kaser, 2001; Wagnon et al., 2001). The governance of $SLA_{EOS}$ change by precipitation variability may have also been enhanced by its influence over the interaction of cloud and solar irradiance. As solar radiation is the primary energy source for ablation here, and cloud cover reduces solar irradiance (Sicart et al., 2005), relative precipitation deficit over eastern glaciers may have increased solar irradiance, thus increasing glacier ablation.

*5.3.5. Central Chilean Andes*

In the Central Chilean Andes, the rate of $SLA_{EOS}$ rise was over 1 m $yr^{-1}$ greater in the west (6.36 m $yr^{-1}$) than the east (5.32 m $yr^{-1}$; Figure 21e). This result is aligned with the finding of increased summer snow cover loss in the western mid-latitude Andes from 1986-2018 (Cordero et al., 2019). These trends are attributable to changing climatic variability over the region from 2000-2020, as ERA5-Land data asserted an increased summer warming trend and more negative summer snowfall trend for the western glaciers (Table 6), and Saavedra et al. (2018) stated that regional precipitation decline from 2000-2016 was more pronounced on western Andean slopes from 30-36˚S. Most notably, the increased drying over the west sub-region corresponds to recent poleward migration of westerlies from the central-southern Andes, which has reduced orographically enhanced western precipitation (Cordero et al., 2019) and is related to the strengthening SAM (Jones et al., 2016). For eastern glaciers, the importance of these climatic controls on Central Chilean Andes $SLA_{EOS}$ is confirmed in the significant negative correlation of rates of $SLA_{EOS}$ change with rates of change in summer snowfall sum (Figure 24a) and significant positive correlation of rates of $SLA_{EOS}$ change with rates of change in summer air temperature (Figure 24b). Quite simply, the former correlation is explained by increased glacier accumulation lowering $SLA_{EOS}$, while the latter is explained by increased energy available for glacier ablation rising $SLA_{EOS}$. The relative influence of a host of other variables – such as glacier area (cf. Kaser, 1995; Rabatel et al., 2013), slope (cf. Deng et al., 2021; Oerlemans et al., 2012), curvature (cf. Carrivick and Chase, 2011; López-Moreno et al., 2006), and aspect (e.g., Malmros et al., 2016; cf. Veettil et al., 2018) – on accumulation and ablation (thus, rates of $SLA_{EOS}$ change) may explain the lack of significant correlation with tested temperature and snowfall variables for the western sub-region. Identified correlations support the association of decreased Andes snow persistence with negative precipitation and positive

temperature trends, south of 29˚S (Saavedra et al., 2018). It should also be noted that, likewise to the Tropical and Central Andes, greatest rates of $SLA_{EOS}$ rise were occurring on low-elevation slopes of the Central Chilean region, demonstrated in western snowlines being consistently lower than their eastern counterparts (Figure 21e). It may therefore be hypothesised that the pattern of increased warming felt by lower altitude regions of the tropics (Vuille and Bradley, 2000) can also be applied to mid-latitudes, contributing to observed east-west differences in warming rates (Table 6), thus rates of $SLA_{EOS}$ change (Figure 21e).

In both east and west sub-regions, rates of $SLA_{EOS}$ rise were increased for the period 2010-2020 (Figure 22). This corresponds to accelerated glacier thinning (Farías-Barahona et al., 2020) and reduced snow persistence (Masiokas et al., 2020) associated with extreme drought conditions over the mid-latitude Andes which persist since 2010 (Garreaud et al., 2020). Recent precipitation deficit was spurred by the role of greenhouse gas forcing and Antarctic stratospheric ozone depletion in the SAM strengthening and subsequent displacement of Southern Hemisphere westerlies (Boisier et al., 2018). Spatial coherence of the $SLA_{EOS}$ response to drought conditions across east and west sub-regions demonstrates the impact of this event.

In the mapped spatio-temporal variation of Central Chilean Andes $SLA_{EOS}$ (Figure 21e), the identified east-west trend in $SLA_{EOS}$ changes is unclear compared to an evident north-south trend in which rates of $SLA_{EOS}$ rise increase south of ~33˚S. Additionally, north of ~33˚S, a weak east-west trend in $SLA_{EOS}$ change is identifiable; however, the trend is reversed, with more positive changes in $SLA_{EOS}$ to the east (Figure 21e). The observed trends suggest that the more positive response of western $SLA_{EOS}$ is concentrated in the region south of 33˚S; this concurs previous suggestion (in *5.2.5.*) that averaged glacier-climate interactions in the Central Chilean region are dominated by glaciers south of 34˚S. As Cordero et al. (2019) also found that the positive east-west gradient in summer snow cover losses was pronounced south of 34˚S, this trend was to be expected. The north-south contrast is ascribed to latitudinal variation in the influence of climatic modes – principally, SAM and ENSO. Studies assert that SAM is dominant over latitudes south of 35˚S (Boisier et al., 2018; Saavedra et al., 2018) and that ENSO is either dominant over latitudes north of 31˚S (Saavedra et al., 2018), 34˚S (Cordero et al., 2019), or 35˚S (Boisier et al., 2018). Due to aforementioned strengthening of SAM (Jones et al. 2016), poleward shift in westerlies (Cordero et al., 2019) and weakening of westerlies at ~40˚S (Thompson et al., 2011), recent precipitation reductions have been more pronounced south of 31˚S (Saavedra et al., 2018), contributing to severe $SLA_{EOS}$ signals in the south. Simultaneously, recent warm ENSO phases have driven increased precipitation from 25-35˚S (Boisier et al., 2018), which contributed to relatively less severe $SLA_{EOS}$ signals in the north. These trends are also supported by the declining snow cover extent between 23-34˚S and 34-40˚S, measured from 1986-2018 (Cordero et al., 2019). From 25-35˚S, summer precipitation variability is parallel to that of the Tropical Andes, with enhanced precipitation on eastern slopes (Viale and Garreaud, 2014). Therefore, observed stability of western glaciers in this

region is unlikely to be related to orographic effects of westerly winds, as declared in Cordero et al. (2019), though ENSO phase transitions would have made this possible in some years (Boisier et al., 2018; Garreaud, 2009). Instead, it could be argued that trends are explained by declining frequency of easterly circulation anomalies further north (Thibeault et al., 2012), which reduce precipitation delivery to, thus stability of, eastern glacier snow cover.

*5.3.6. Southern Andes*

From 2000-2020, eastern Southern Andes $SLA_{EOS}$ was rising at a non-significant rate of 2.90 m $yr^{-1}$ whilst western Southern Andes $SLA_{EOS}$ was lowering at a non-significant rate of -2.22 m $yr^{-1}$ (Figure 21f), confirming that the lack of trend in Southern Andes mean $SLA_{EOS}$ is explained by contrasting signals for east and west glaciers. This spatio-temporal variation corroborates findings of highly positive surface mass balance in the western SPI compared to the eastern SPI from 1975-2011 (Schaefer et al., 2015), as well as findings showing average ablation sums to be greater on eastern NPI outlet glaciers than their western counterparts (Schaefer et al., 2013). Though less comparable, these results are also aligned with rates of Southern Andes glacier area change; Aravena and Luckman (2009) have identified accelerated shrinkage to the east, while stability or advancement of western glaciers has been recorded in multiple studies (Aniya, 1997; Minowa et al., 2021). The observed east-west variability is reasoned with climatic variability identified in ERA5-Land estimates. It was established that climate over eastern glaciers had been warming and drying at faster rates than over western glaciers (Table 6). Concurrently, previous works acknowledge prevailing westerly winds and orographic enhancement of precipitation over the windward western Southern Andes (Davies and Glasser, 2012; Masiokas et al., 2020; Mernild et al., 2017), contributing to relatively cold and wet conditions (Mernild et al., 2016) favourable for glacier accumulation, whilst continuation of strong downslope winds over the leeward eastern glaciers increases aridity (Garreaud et al., 2013; Schneider and Gies, 2004) in favour of glacier ablation. As this gradient is reduced under weakened westerlies (Garreaud et al., 2013), $SLA_{EOS}$ variability is likely related to intensification of westerlies over southernmost South America (Garreaud et al., 2013; Thompson et al., 2011) which reflects increasing SAM index in recent decades (Aguirre et al., 2018; Fogt and Marshall, 2020). Additionally, persistent orographic clouds associated with increasing western precipitation may have enhanced the east-west $SLA_{EOS}$ variability, as they can considerably lower receipt of incoming solar radiation over western Patagonia, reducing glacier ablation (Bravo et al., 2022; Schaefer et al., 2013). Supporting hypotheses of climatic control, there was a significant negative correlation of $SLA_{EOS}$ change rates with summer snowfall change rates for the west sub-region (Figure 24c), and significant positive correlations of $SLA_{EOS}$ change rates with summer air temperature change rates for both east and west sub-regions (Figures 24d and 24e).

Decadal comparisons of the east-west variability in Southern Andes $SLA_{EOS}$ revealed that the observed contrast was amplified for the most recent period. There was minimal difference in east and west rates

of $SLA_{EOS}$ rise during 2000-2010 but, for 2010-2020, eastern $SLA_{EOS}$ change was strongly positive and western $SLA_{EOS}$ change was strongly negative (Figure 22). Aligned with the minimal east-west difference from 2000-2010, Davies and Glasser (2012) identified that rates of area change were similar for glaciers east and west of the SPI from 2001-2011. Similarly, aligned with increasing rates of eastern $SLA_{EOS}$ rise between decades, Dussaillant et al. (2019) identified that two eastern Patagonian catchments had increased river runoff contribution and greater negative mass balance from 2009-2018 compared to from 2000-2009. Explanation for the decadal variability most likely stems from explanations for the overall $SLA_{EOS}$ trends of east and west sub-regions, and the stark contrast between decades highlights that trends for the 21-year period (Figure 21f) are dominated by glacier responses in the most recent decade.

Rates of Southern Andes $SLA_{EOS}$ change also had north-south variability, with generally positive rates of change (snowlines rising) north of ~53˚S, and generally negative rates of change (snowlines lowering) south of ~53˚S (Figure 21f). This variability was seen previously in the increasing stability of sub-regional $SLA_{EOS}$ trends (NPI, SPI, and Cordillera Darwin) with increasing latitude (Figure 17), signalling that these small-scale analyses were representative of the wider trend. A similar north-south variability in Southern Andes glacier behaviour was considered in Davies and Glasser (2012), which reported decelerated glacier shrinkage rates south of 54˚S, and in Carrasco et al. (2008), which reported ELA rise in Patagonia (~41.5˚S) but ELA lowering in Punta Arenas (~53˚S). These results imply that the well-reported poleward displacement of SAM-driven westerlies (Aguirre et al., 2018; Cordero et al., 2019; Moreno et al., 2010) is causing increased aridity in the northern region (i.e., Patagonian icefields) and increased snowfall in the southernmost region (i.e., Tierra del Fuego). Correspondingly, Garreaud et al. (2013) documented long-term decline in westerlies over northern Patagonia and increase in westerlies south of 50˚S, while Thompson et al. (2011) related positive SAM to weakened westerlies at ~40˚S and strengthened westerlies at ~60˚S. This precipitation variability, and associated variability in cloud cover and solar irradiance, would explain relative instability of $SLA_{EOS}$ north of ~53˚S via the relative dominance of net ablation in this region. This also indicates why an east-west trend is not visible in mapped spatio-temporal variability (Figure 21f). As glaciers in the southernmost region were designated ‘west’ by drainage basin data, eastern Southern Andes glaciers are confined to the Patagonian region, north of 52˚S (Figure 4). This meant that the lowering trend in western $SLA_{EOS}$ was amplified by glacier stability in the southernmost region, while the rising trend in eastern $SLA_{EOS}$ was amplified by glacier instability in the northern region. This may explain why the finding of increased ablation over western slopes of the SPI in 2015/2016 (Bravo et al., 2022) was not identifiable in the east-west variation presented here.

### 5.4. Synthesis, outlook, and implications

Overall, the majority of Southern Hemisphere glacier snowlines have been rising over recent decades (Figures 15 and 21), with an accelerating rate of rise in many regions (Figure 22). Exceptions are (a) the non-significant trend of snowline lowering in the west Antarctic Peninsula, but this trend displayed signs of reversal since 2014, and (b) the non-significant trend of snowline lowering in the west Southern Andes, but this trend was governed by glaciers in the southernmost region and did not represent changes at the Patagonian icefields. Across the Southern Hemisphere, snowlines in this southernmost Andes region (south of ~53˚S) were most stable (Figure 21f), interpreted to reflect high precipitation inputs, whilst snowlines in the southern Central Chilean Andes (~33-40˚S) were least stable (Figure 21e), interpreted to reflect drought conditions post-2010. Areas of the Antarctic Peninsula have exhibited snowline instability in the same order of magnitude as the southern Central Chilean Andes (Figure 21b and 19e), reflecting high sensitivities to rapid warming, but Antarctic Peninsula instability was not so spatially consistent. The Southern Alps displayed comparatively less spatial variability in rates of snowline change, and snowline retreat rates were generally an order of magnitude lower than for the majority of the Andes and Antarctic Peninsula (Figure 21); this may have resulted from relative spatial consistency of a high-precipitation maritime climate across this region (Anderson et al, 2010; Chinn, 1995).

Synthesis of the east-west disparities in rates of $SLA_{EOS}$ change across the Southern Hemisphere (Figure 21) provides coherent evidence for the hemispheric variability in wind trends over recent decades, as (a) increased rates of snowline rise to the east of the Southern Alps, Antarctic Peninsula, and Southern Andes has pointed to well-documented prevailing westerlies in these regions (Carrivick et al., 2019; Fitzharris et al., 2007), (b) increased rates of snowline rise to the east of both the Tropical and Central Andes has supported hypotheses of strengthening westerlies and weakening easterlies at low latitudes (Thibeault et al., 2012), and (c) increased rates of snowline rise in the west Central Chilean Andes has supported hypothesised weakening of westerlies at ~40˚S (Thompson et al., 2011). Additionally, inter-regional comparison of these eastern $SLA_{EOS}$ trends signals the teleconnections between Andean and Southern Alps glaciers. Fitzharris et al. (2007) asserted an in-phase relation of the Southern Alps and Patagonia, and out-of-phase relation of the Southern Alps and Tropical Andes; concurrently, mean eastern $SLA_{EOS}$ rise occurred at 2.70 and 2.90 m $yr^{-1}$ for Southern Alps and Patagonia glaciers respectively, but 7.55 m $yr^{-1}$ for Tropical Andes glaciers. Evidenced teleconnections point to lee side impacts of mid-latitude reduction in westerlies and low-latitude enhancement of westerlies, mentioned above. Similarly, synthesis of the north-south disparities in rates of $SLA_{EOS}$ change for the Andean study regions (Figures 21c-f) has also evidenced latitudinal variation in westerly wind strength. As such, presented $SLA_{EOS}$ variability could be used for updated interpretation of Andes climatic zones; the suggested interpretation (based on Figures 21c-f) is separation of the northern and southern Central Chilean Andes at 33˚S, and separation of the northern and southern Southern Andes at 53˚S.

If the prevailing rising trends in $SLA_{EOS}$ continue, severe consequences for the longevity of Southern Hemisphere glaciers are to be expected. As transient glacier snow cover increases albedo, increasing $SLA_{EOS}$ is associated with increasing exposure of darker lower glacier surfaces to ablation processes. Albedo reduction in the absence of snow cover was liable for increased Andean glacier melt under recent drought conditions (Shaw et al., 2020), for instance. However, the extent of this ablation is dependent on glacier hypsometry and slope, with enhanced effects on bottom-heavy and low-slope glaciers (De Angelis, 2014; Oerlemans et al., 2012); this dependency will therefore affect the severity of the identified regional and sub-regional $SLA_{EOS}$ sensitivity at glacier level. Following increased ablation, melt can be accelerated through feedback processes; for example, via formation of supraglacial melt ponds which lower surface albedo further to increase local absorption of shortwave radiation (Kingslake et al., 2017). Under temperate glacier conditions, such as those observed for Patagonia and the Southern Alps, the increased meltwater is also associated with glacier wastage via increased basal sliding (Purdie et al., 2008; Collao-Barrios et al., 2018). Thus, progressive losses in glacier mass balance via ablation and subsequent dynamic changes are expected to result from trends of rising $SLA_{EOS}$ identified here. In the case of average lowering of $SLA_{EOS}$ in the southernmost Andes (Figure 21f), there is opportunity for reversed albedo feedback to enhance snow persistence, though this requires regional cooling (Fox-Kemper et al., 2021) which is currently not projected.

As this analysis has identified multiple potential linkages between $SLA_{EOS}$ trends and climate, it is important to consider how climate change will manifest itself in the Southern Hemisphere in near decades, in order to estimate the wider outlook. Projected strengthening of the SAM is controlled by greenhouse gas forcing and, to a lesser extent, ozone depletion (Boisier et al., 2018; Goyal et al., 2021; Lim et al., 2016; Mao et al., 2021). If the SAM continues its positive trajectory, as $SLA_{EOS}$ spatio-temporal variability suggests it has been in recent decades, westerlies are forecast to intensify (Deng et al., 2022; Thibeault et al., 2012) and continue displacement (Cordero et al., 2019), enhancing the precipitation trend at high latitudes and summer drying trend at mid-latitudes (Bodeker et al., 2022; Bozkurt et al., 2018, 2021; Garreaud et al., 2020; Lim et al., 2016; Thompson et al., 2011; Zazuile et al., 2017). At lower latitudes, future precipitation variability is debated, though even projected increases in precipitation could not alleviate glacier instability (Neukom et al., 2015; Potter et al., 2023; Thibeault et al., 2012). Simultaneously, warming is projected for all study regions (Mao et al., 2021; Mullan et al., 2018; Pabón-Caicedo et al., 2020), with near doubling of marine heatwave intensity anticipated for the New Zealand region by 2100 (Bodeker et al., 2022). The frequency and intensity of ENSO phase transitions is also expected to amplify over coming decades (Cai et al., 2020), which will affect the variability of drought conditions (Rivera et al., 2017; Sulca et al., 2016) and blocking episodes (Patterson et al., 2019).

With these projections in mind, the presently negative overall outlook for Southern Hemisphere glacier snowlines shows little sign of reversal, as there is reason to anticipate continued $SLA_{EOS}$ rise in every

region. In synthesis, the areas this study perceives as most vulnerable to ongoing change against the generalised trend of rising snowlines are, (a) eastern flanks of high and low-latitude ranges, where the previously mentioned effects of downslope wind (e.g., foehn) will likely increase from westerly wind intensification (e.g., Mao et al., 2021), (b) the southern Central Chilean Andes, where both SAM and La Niña effects will bring increased drought to a region which currently presents the most significant response to drying trends (Figure 24a), and (c) the maritime Southern Alps, where effects of marine heatwaves, set to intensify, have previously produced peak $SLA_{EOS}$ (Figure 15a; Lorrey et al., 2022).

Generally, the wider outcome of continued glacier ablation ensuing the identified $SLA_{EOS}$ changes will be temporary enhancement of meltwater runoff as glaciers shrink, followed by long-term relative drought conditions as glaciers disappear (Huss and Hock, 2018). Increased runoff and glacier mass loss will have global-scale implications via increased sea level contributions (Zemp et al., 2019), particularly for marine-terminating glaciers of the Antarctic Peninsula and Southern Andes (e.g., Bravo et al., 2021). At a regional level, increased runoff may precede increased frequency of flood hazards (Bodeker et al., 2022; Bozkurt et al., 2018), including glacial lake outburst floods (Drenkhan et al., 2018), and water infrastructure needs to be equipped to handle increased inflows (Purdie et al., 2022). Eventual water scarcity will create issues of allocation to hydropower, agriculture and human consumption in New Zealand and South America (Buytaert et al., 2017; Milner et al., 2017), and policies will be needed to avoid associated conflict (Lynch, 2012). Local environmental impacts may follow drought in the form of fires (González et al., 2018) and ecological losses (Garreaud et al., 2018), and local economic impacts may be felt in the deterioration of glacier tourism (Stewart et al., 2016).

### 5.5. Priorities for future research

This study has demonstrated application of automated $SLA_{EOS}$ calculation at regional and intra-regional scales across the Southern Hemisphere, with which glacier and climate variability can be inferred. To build upon results presented here, future studies should expand this research to global coverage. This would allow for hemisphere level comparisons in snowline evolution, climate trends, and their interaction, and may reveal potential teleconnections (cf. Fitzharris et al., 2007) between different world regions.

As a majority of east/west sub-regions exhibited accelerating rates of mean $SLA_{EOS}$ rise (Figure 22), it is proposed that $SLA_{EOS}$ trends be updated with regional mean results more frequently (e.g., annually), to ensure close monitoring of this acceleration and its potential wider impacts. For the 21-year period studied here, strong inter-annual variability in many regional $SLA_{EOS}$ patterns meant that timeframes chosen to calculate trends affected overall findings. As additional annual $SLA_{EOS}$ means are calculated, and wider timeframes can be used for trend calculation and comparison, the impact of inter-annual variability on overall trends will plausibly be reduced.

Under projected climate change and accelerated instability of many Southern Hemisphere glacier regions (Figure 22), it is important that researchers keep updated estimates of glacier response times for prediction of future glacier mass loss and longevity. An inflection point in the Southern Alps $SLA_{EOS}$ trend was here linked to a lagged inflection point in the terminus extent trend of glaciers in this region (Mackintosh et al., 2017), demonstrating short response time (see *5.2.1.*). It is hypothesised that further statistical comparison of the presented $SLA_{EOS}$ data to recorded variability in glacier areas and extents may yield estimates of glacier response times. Estimates could be extended globally in line with extension of $SLA_{EOS}$ calculations, to gain a world view of glacier vulnerability.

Concerned primarily with quantifying $SLA_{EOS}$ variability across the Southern Hemisphere, this study's investigation of causal factors in $SLA_{EOS}$ change was constrained to use of mean summer air temperature and snowfall sum data. Spatio-temporal analysis revealed potential control of topographic factors on rates of $SLA_{EOS}$ change – for instance, (a) the east/west sub-region with lower terrain elevation displayed increased rates of $SLA_{EOS}$ change in four of the six regions, and (b) glaciers in areas where general aspect was favourable for increased solar radiation receipt often had relatively increased rates of $SLA_{EOS}$ change (e.g., northern Southern Alps). Spatio-temporal analysis also implied the control of wind strength and direction (i.e., Southern westerlies and foehn wind) on $SLA_{EOS}$ change via its effect on ablation rates. A next step in snowline research should be to quantify the correlation of these factors – along with others previously suggested, such as glacier area (e.g., Kaser, 1995), slope (e.g., Oerlemans et al., 2012), curvature (e.g., Carrivick and Chase, 2011), sensible heat flux (e.g., Minowa et al., 2022), and solar irradiance (e.g., Sicart et al., 2005) – with spatio-temporal $SLA_{EOS}$ variability across the Southern Hemisphere. This will also aid explanation of the relative influence of summer air temperature and snowfall, and why significant correlations of these factors with $SLA_{EOS}$ change were only identified in two regions.

## 6. Conclusions

This study has been the first to quantify multi-decadal glacier $SLA_{EOS}$ trends across the Southern Hemisphere under one consistent automated approach. Glacier snow cover was classified in end-of-summer Landsat scenes using Otsu, and $SLA_{EOS}$ was delineated at lowest altitude from which SCR was continuously > 0.5. $SLA_{EOS}$ results were retrieved for 6485 glaciers from 1983-2020, and $SLA_{EOS}$ trends for 2000-2020 were analysed in six distinct regions: Southern Alps, Antarctic Peninsula, Tropical Andes, Central Andes, Central Chilean Andes, and Southern Andes. Identified spatio-temporal variability in $SLA_{EOS}$ has, in turn, built supporting information for the spatio-temporal variability in recent Southern Hemisphere climate. Compared to the Northern Hemisphere, there is disproportionately sparse coverage of meteorological observations in Southern Hemisphere high-altitude mountain regions. Therefore, these regions have been historically underrepresented in climate change trends, and $SLA_{EOS}$ observations at high spatio-temporal detail have demonstrated utility in addressing this issue.

Spatially, snowlines aligned with regional variability in terrain elevation; $SLA_{EOS}$ reduced decidedly with latitude in the Andes, moderately with latitude in the Southern Alps, and toward the coastal Antarctic Peninsula. The study has also supported association of $SLA_{EOS}$ spatial variability and glacier aspect, as Southern Alps glaciers with lower $SLA_{EOS}$ backed onto the direction of solar irradiance. However, relations of $SLA_{EOS}$ to topographic characteristics were not explored statistically in this study, and it was proposed that future analyses utilise $SLA_{EOS}$ data presented here to do so. For the Southern Alps, Central Chilean Andes, and Southern Andes, eastern $SLA_{EOS}$ clearly exceeded western $SLA_{EOS}$, and this trend was reversed for the Central Andes. East-west contrast was less obvious for the Antarctic Peninsula and Tropical Andes, where missing years of data hindered comparison; however, trends implied western $SLA_{EOS}$ was higher on average. Mostly, higher $SLA_{EOS}$ existed on leeward slopes of prevailing moisture transport, meaning trends could partially be explained by east-west differences in accumulation. However, differences in terrain elevation and hypsometry were also likely to play a role.

From 2000-2020, $SLA_{EOS}$ rose in every region except the Southern Andes, which displayed no overall change, and rising trends were statistically significant ($p < 0.05$) in all regions except the Central Andes. Rising trends in mean $SLA_{EOS}$ ranged from 2.19 to 6.28 m $yr^{-1}$; the Tropical Andes had the greatest rate of $SLA_{EOS}$ rise, though considerable shortage of satellite imagery meant results were associated with larger S.E. than for other regions. Rates of $SLA_{EOS}$ change were also much higher (> 30 m $yr^{-1}$) and lower (< -30 m $yr^{-1}$) for many individual glaciers; however, there was no way of validating these figures for the 6485 glaciers studied, hence this study's primary concern with mean $SLA_{EOS}$ trends. The range and variability in regional mean $SLA_{EOS}$ over the period was large in the Tropical and Central Andes, and considerably smaller in the Southern Alps. All regions displayed minimum $SLA_{EOS}$ early in the period (pre-2006) – most of which in 2001, during cool episodes of snow accumulation – and almost all regions went on to display maximum $SLA_{EOS}$ later in the period (post-2012). Inter-annual variability

was often linked to ENSO phases; for instance, 2015/16 El Niño was proposed as a driver for strong positive $SLA_{EOS}$ anomaly in the Southern Alps and Tropical Andes in 2016. Meanwhile, overall $SLA_{EOS}$ changes were primarily linked to prevailing summer warming and drying trends for each region. However, where regional $SLA_{EOS}$ trends were weak (Southern Andes), or where regional response to temperature trends was not shown (Antarctic Peninsula), it reflected an east-west or north-south disparity in the $SLA_{EOS}$ signal which was revealed in subsequent spatio-temporal analysis.

Intra-regional spatio-temporal analysis revealed the southern Central Chilean Andes as the region of most considerable $SLA_{EOS}$ rise (between 10 and 30 m $yr^{-1}$), and the southernmost Andes as the region of most considerable $SLA_{EOS}$ decline (between -30 and -1 m $yr^{-1}$). Across the Southern Alps, rates of $SLA_{EOS}$ rise were more consistently positive towards the northeast, and across the Antarctic Peninsula, rates of $SLA_{EOS}$ rise were highly variable. Within east/west sub-regions, $SLA_{EOS}$ exhibited a rising trend (between 1.63 and 7.55 m $yr^{-1}$) in every instance except the west Antarctic Peninsula (-0.28 m $yr^{-1}$) and west Southern Andes (-2.22 m $yr^{-1}$). Correspondingly, rates of eastern $SLA_{EOS}$ rise exceeded those of the west in every region except the Central Chilean Andes. Most concerningly, $SLA_{EOS}$ rise was accelerating in the majority of cases, with increased rates of change from 2010-2020, compared to from 2000-2010. However, there was considerable deceleration of $SLA_{EOS}$ changes for western sub-regions of the Tropical and Central Andes, and $SLA_{EOS}$ decline was foremost in the western Southern Andes from 2010-2020. This study proposed that east-west disparities in $SLA_{EOS}$ change demonstrated (a) the action of prevailing winds in enhancing snow accumulation on windward slopes and enhancing downslope winds (e.g., foehn) which induce snow ablation on leeward slopes, and/or (b) differences in terrain elevation, with increased ablation on low-lying glaciers which are more exposed to warming trends. Simultaneously, north-south disparities in $SLA_{EOS}$ change within the Central Chilean Andes and Southern Andes were linked to latitudinal variation in the strengthening and weakening of westerlies.

Presented $SLA_{EOS}$ trends have strongly underlined the impact of large-scale climatic modes on Southern Hemisphere glaciers and climate. Particularly evident is the recent SAM strengthening and related westerly flow increase (decrease) at higher latitudes (mid-latitudes), exhibited in prominent $SLA_{EOS}$ lowering (rise) in the southernmost (southern Central Chilean) Andes, dominating the regional trend. Results also support hypotheses of easterly flow reduction and/or westerly flow intensification in the Tropical and Central Andes.

Altogether, Southern Hemisphere glacier snowlines were predominantly retreating from 2000-2020, but rates of change were spatially and temporally variable. The southernmost Andes and western slopes demonstrated greatest stability, the southern Central Chilean Andes and eastern slopes demonstrated greatest instability, and snowline rise generally accelerated with time. As continued anthropogenic forcing disturbs climatic variability, the observed snowline trends will likely amplify. This will have critical implications for glacier mass loss and hydrological change on local to global scales.

## 7. References


Abrahim, B., Cullen, N., Conway, J., and Sirguey, P. (2023) Applying a distributed mass-balance model to identify uncertainties in glaciological mass balance on Brewster Glacier, New Zealand. *Journal of Glaciology*, 1-17.

Abram, N.J., Mulvaney, R., Wolff, E.W., Triest, J., Kipfstuhl, S., Trusel, L.D., Vimeux, F., Fleet, L., and Arrowsmith, C. (2013) Acceleration of snow melt in an Antarctic Peninsula ice core during the twentieth century. *Nature Geoscience*, **6**(5), 404-411.

Ackerley, D., Dean, S., Sood, A., and Mullan, A. B. (2012). Regional climate modelling in New Zealand: Comparison to gridded and satellite observations. *Weather and Climate*, **32**(1), 3-22.

Adler, C., Wester, P., Bhatt, I., Huggel, C., Insarov, G.E., Morecroft, M.D., Muccione, V., and Prakash, A. (2022) *Cross-Chapter Paper 5: Mountains. In: Climate Change 2022: Impacts, Adaptation and Vulnerability. Contribution of Working Group II to the Sixth Assessment Report of the Intergovernmental Panel on Climate Change.* Cambridge: Cambridge University Press.

Aguirre, F., Carrasco, J., Sauter, T., Schneider, C., Gaete, K., Garín, E., et al. (2018). Snow cover change as a climate indicator in Brunswick Peninsula, Patagonia. *Frontiers in Earth Science*, **6**, 130.

AL-Doski, J., Mansor, S.B., San, H.P., and Khuzaimah, Z. (2020) No. 7 SCS+C Topographic Correction to Enhance SVM Classification Accuracy. *Journal of Engineering Technology and Applied Physics*, Special Issue 1.

Alisov, B.P. (1954) *Die Klimate der Erde (ohne das Gebiet der UdSSR).* Deutscher Verlag der Wissenschaften: Berlin. 277

Allega, L., Pisoni, J. P., Cozzolino, E., Maenza, R. A. and Piccolo, M. C. (2021). The variability of sea surface temperature in the Patagonian Shelf Argentina, from 35 years of satellite information. *International Journal of Remote Sensing*, **42**(16), 6090-6106.

Anderson, B., and Mackintosh, A. (2012) Controls on mass balance sensitivity of maritime glaciers in the Southern Alps, New Zealand: The role of debris cover. *Journal of Geophysical Research: Earth Surface*, **117**(F1).

Anderson, B., Mackintosh, A., Stumm, D., George, L., Kerr, T., Winter-Billington, A. and Fitzsimons, S. (2010) Climate sensitivity of a high-precipitation glacier in New Zealand. *Journal of Glaciology*, **56**, 195.

Aniya, M., Sato, H., Naruse, R., Skvarca, P. and Casassa, G. (1997). Recent glacier variations in the Southern Patagonia icefield, South America. *Arctic and Alpine Research*, **29**(1), 1-12.

Aravena, J. C. and Luckman, B. H. (2009). Spatio-temporal rainfall patterns in southern South America. *International Journal of Climatology: A Journal of the Royal Meteorological Society*, **29**(14), 2106-2120.

Ayala, Á., Schauwecker, S., and MacDonell, S. (2023). Spatial distribution and controls of snowmelt runoff in a sublimation-dominated environment in the semiarid Andes of Chile. *Hydrology and Earth System Sciences Discussions*, 1-32.

Barcaza, G., Nussbaumer, S. U., Tapia, G., Valdés, J., García, J. L., Videla, Y., et al. (2017). Glacier inventory and recent glacier variations in the Andes of Chile, South America. *Annals of Glaciology*, **58**(75), 166-180.

Barrell, S., Riishojgaard, L.P., and Dibbern, J. (2013) The Global Observing System. *Bulletin*, **6**(1). Available online: https://public.wmo.int/en/resources/bulletin/global-observing-system [accessed 02/06/23].

Benn, D.I., and Lehmkuhl, F. (2000) Mass balance and equilibrium-line altitudes of glaciers in high-mountain environments. *Quaternary International*, **65-66**, 15-29.

Bettiol, G. M., Ferreira, M. E., Motta, L. P., Cremon, É. H., and Sano, E. E. (2021) Conformity of the NASADEM_HGT and ALOS AW3D30 DEM with the altitude from the Brazilian geodetic reference stations: A case study from Brazilian Cerrado. *Sensors*, **21**(9), 2935.

Bliss, A., Hock, R. and Radić, V. (2014) Global response of glacier runoff to twenty-first century climate change. *Journal of Geophysical Research: Earth Surface*, **119**(4), 717–730.

Bodart, J. A., and Bingham, R. J. (2019). The impact of the extreme 2015–2016 El Niño on the mass balance of the Antarctic ice sheet. *Geophysical Research Letters*, **46**(23), 13862-13871.

Bodeker, G., Cullen, N., Katurji, M., McDonald, A., Morgenstern, O., Noone, D., Renwick, J., Revell, L. and Tait, A. (2022). Aotearoa New Zealand climate change projections guidance: Interpreting the latest IPCC WG1 report findings. Prepared for the Ministry for the Environment, Report number CR 501, 51p.

Boisier, J. P., Alvarez-Garreton, C., Cordero, R. R., Damiani, A., Gallardo, L., Garreaud, R. D., et al. (2018). Anthropogenic drying in central-southern Chile evidenced by long-term observations and climate model simulations. *Elementa: Science of the Anthropocene*, **6**, 74.

Bojinski, S., Verstraete, M., Peterson, T.C., Richter, C., Simmons, A. and Zemp, M. (2014) The concept of essential climate variables in support of climate research, applications, and policy. *Bulletin of the American Meteorological Society*, **95**(9), 1431-1443.

Bown, F., Rivera, A., Pętlicki, M., Bravo, C., Oberreuter, J., and Moffat, C. (2019). Recent ice dynamics and mass balance of Jorge Montt Glacier, Southern Patagonia Icefield. *Journal of Glaciology*, **65**(253), 732-744.

Bozkurt, D., Bromwich, D. H., Carrasco, J. and Rondanelli, R. (2021). Temperature and precipitation projections for the Antarctic Peninsula over the next two decades: contrasting global and regional climate model simulations. *Climate Dynamics*, **56**(11-12), 3853-3874.

Bozkurt, D., Rojas, M., Boisier, J. P. and Valdivieso, J. (2018). Projected hydroclimate changes over Andean basins in central Chile from downscaled CMIP5 models under the low and high emission scenarios. *Climatic Change*, **150**, 131-147.

Braithwaite, R.J. (1984) Can the Mass Balance of a Glacier Be Estimated from Its Equilibrium-Line Altitude. *Journal of Glaciology*, **30**(106), 364–368.

Bravo, C., Bozkurt, D., Gonzalez-Reyes, Á., Quincey, D. J., Ross, A. N., Farías-Barahona, D. and Rojas, M. (2019). Assessing snow accumulation patterns and changes on the Patagonian Icefields. *Frontiers in Environmental Science*, **30**.

Bravo, C., Bozkurt, D., Ross, A. N., and Quincey, D. J. (2021). Projected increases in surface melt and ice loss for the Northern and Southern Patagonian Icefields. *Scientific Reports*, **11**(1), 16847.

Bravo, C., Ross, A. N., Quincey, D. J., Cisternas, S. and Rivera, A. (2022). Surface ablation and its drivers along a west–east transect of the Southern Patagonia Icefield. *Journal of Glaciology*, **68**(268), 305-318.

Burns, P. and Nolin, A. (2014). Using atmospherically-corrected Landsat imagery to measure glacier area change in the Cordillera Blanca, Peru from 1987 to 2010. *Remote Sensing of Environment*, **140**, 165-178.

Buytaert, W., Moulds, S., Acosta, L., De Bièvre, B., Olmos, C., Villacis, M., et al. (2017). Glacial melt content of water use in the tropical Andes. *Environmental Research Letters*, **12**(11), 114014.

Cai, W., McPhaden, M. J., Grimm, A. M., Rodrigues, R. R., Taschetto, A. S., Garreaud, R. D., Dewitte, B., Poveda, G., Ham, Y., Santoso, A., Ng, B., Anderson, W., Wang, G., Geng, T., Jo, H., Marengo, J.A., Alves, L.M., Osman, M., Li, S., Wu, L., Karamperidou, C., Takahashi, K. and Vera, C. (2020). Climate impacts of the El Niño–southern oscillation on South America. *Nature Reviews Earth & Environment*, **1**(4), 215-231.

Calizaya, E., Laqui, W., Sardón, S., Calizaya, F., Cuentas, O., Cahuana, J., Mindani, C. and Huacani, W. (2023). Snow Cover Temporal Dynamic Using MODIS Product, and Its Relationship with Precipitation and Temperature in the Tropical Andean Glaciers in the Alto Santa Sub-Basin (Peru). *Sustainability*, **15**(9), 7610.

Cape, M. R., Vernet, M., Skvarca, P., Marinsek, S., Scambos, T. and Domack, E. (2015). Foehn winds link climate-driven warming to ice shelf evolution in Antarctica. *Journal of Geophysical Research: Atmospheres*, **120**(21), 11-037.

Carrasco-Escaff, T., Rojas, M., Garreaud, R. D., Bozkurt, D. and Schaefer, M. (2023). Climatic control of the surface mass balance of the Patagonian Icefields. *The Cryosphere*, **17**(3), 1127-1149.

Carrasco, J. F., and Cordero, R. R. (2020). Analyzing precipitation changes in the northern tip of the Antarctic peninsula during the 1970–2019 period. *Atmosphere*, **11**(12), 1270.

Carrasco, J. F., Bozkurt, D., and Cordero, R. R. (2021). A review of the observed air temperature in the Antarctic Peninsula. Did the warming trend come back after the early 21st hiatus?. *Polar Science*, **28**, 100653.

Carrasco, J. F., Osorio, R. and Casassa, G. (2008). Secular trend of the equilibrium-line altitude on the western side of the southern Andes, derived from radiosonde and surface observations. *Journal of Glaciology*, **54**(186), 538-550.

Carrivick, J. L., Davies, B. J., James, W. H., McMillan, M., and Glasser, N. F. (2019). A comparison of modelled ice thickness and volume across the entire Antarctic Peninsula region. *Geografiska Annaler: Series A, Physical Geography*, **101**(1), 45-67.

Carrivick, J.L., and Chase, S.E. (2011) Spatial and temporal variability of annual glacier equilibrium line altitudes in the Southern Alps, New Zealand. *New Zealand Journal of Geology and Geophysics*, **54**(4), 415-429.

Casteller, A., Villalba, R., Araneo, D., and Stöckli, V. (2011). Reconstructing temporal patterns of snow avalanches at Lago del Desierto, southern Patagonian Andes. *Cold Regions Science and Technology*, **67**(1-2), 68-78.

Charton, J., Jomelli, V., Schimmelpfennig, I., Verfaillie, D., Favier, V., Mokadem, F., Gilbert, A., Brun, F., Aumaître, G., Bourlès, D.L., and Keddadouche, K. (2021) A debris-covered glacier at Kerguelen (49°S, 69°E) over the past 15 000 years. *Antarctic Science*, **33**(1), 103-115.

Chevallier, P., Pouyaud, B., and Suarez, W. (2011). Climate change threats to environment in the tropical Andes: glaciers and water resources. *Reg Environ Change*, **11,** 179–187

Chinn, T. J. (1999). New Zealand glacier response to climate change of the past 2 decades. *Global and Planetary Change*, **22**(1-4), 155-168.

Chinn, T. J. H. (1995). Glacier fluctuations in the Southern Alps of New Zealand determined from snowline elevations. *Arctic and alpine research*, **27**(2), 187-198.

Chinn, T.J.H. (1995) Glacier Fluctuations in the Southern Alps of New Zealand Determined from Snowline Elevations. *Arctic and Alpine Research*, **27**(2), 187-198.

Clare, G.R., Fitzharris, B.B., Chinn, T.J.H., Salinger, M.J. (2002) Interannual variation in end-of-summer snowlines of the Southern Alps of New Zealand, and relationships with Southern Hemisphere atmospheric and sea surface temperature patterns. *International Journal of Climatology*, **22**, 107-120.

Cogley, J.G., Hock, R., Rasmussen, L.A., Arendt, A.A., Bauder, A., Braithwaite, R.J., Jansson, P., Kaser, G., Möller, M., Nicholson, L., and Zemp, M. (2011). *Glossary of glacier mass balance and related terms*, IHP-VII technical documents in hydrology No. 86, IACS Contribution No. 2: UNESCO-IHP, Paris

Collao-Barrios, G., Gillet-Chaulet, F., Favier, V., Casassa, G., Berthier, E., Dussaillant, I., et al. (2018). Ice flow modelling to constrain the surface mass balance and ice discharge of San Rafael Glacier, Northern Patagonia Icefield. *Journal of Glaciology*, **64**(246), 568-582.

Condom, T., Coudrain, A., Sicart, J.E. and Théry, S. (2007) Computation of the space and time evolution of equilibrium-line altitudes on Andean glaciers (10 N–55 S). *Global and Planetary change*, **59**(1-4),189-202.

Constable, A.J., Harper, S., Dawson, J., Holsman, K., Mustonen, T., Piepenburg, D., and Rost, B. (2022) *Cross-Chapter Paper 6: Polar Regions. In: Climate Change 2022: Impacts, Adaptation and Vulnerability.*

*Contribution of Working Group II to the Sixth Assessment Report of the Intergovernmental Panel on Climate Change*. Cambridge: Cambridge University Press.

Copernicus Sentinel data (2020), processed by ESA [accessed 19/07/23].

Cordero, R R., Asencio, V., Feron, S., Damiani, A., Llanillo, P.J., Sepulveda, E., Jorquera, J., Carrasco, J. and Casassa, G. (2019) Dry-season snow cover losses in the andes (18°–40°S) driven by changes in large-scale climate modes. *Scientific Reports*, **9**, 16945.

Crane, R.G. and Anderson, M.R. (1984) Satellite discrimination of snow/cloud surfaces. *International Journal of Remote Sensing*, **5**(1), 213-223.

Cuffey, K.M., and Paterson, W.S.B. (2010). *The physics of glaciers*. Academic Press.

Davies, B. J., and Glasser, N. F. (2012). Accelerating shrinkage of Patagonian glaciers from the Little Ice Age (~ AD 1870) to 2011. *Journal of Glaciology*, **58**(212), 1063-1084.

Davies, B. J., Carrivick, J. L., Glasser, N. F., Hambrey, M. J., and Smellie, J. L. (2012) Variable glacier response to atmospheric warming, northern Antarctic Peninsula, 1988–2009. *The Cryosphere*, **6**, 1031–1048.

Davies, B.J., Carrivick, J.L., Glasser, N.F., Hambrey, M.J., and Smellie, J.L. (2011) A new glacier inventory for 2009 reveals spatial and temporal variability in glacier response to atmospheric warming in the Northern Antarctic Peninsula, 1988–2009**.** *The Cryosphere Discussions*, **5**, 3541-3594.

Davies, B.J., Golledge, N.R., Glasser N.F., Carrivick, J.L., Lightenberg, S.R.M., Barrand, N.E., Van den Broeke, M.R., Hambrey, M.J., and Smellie, J.L. (2014) Modelled glacier response to centennial temperature and precipitation trends on the Antarctic Peninsula. *Nature Climate Change*, **4**, 993-998.

De Angelis, H. (2014). Hypsometry and sensitivity of the mass balance to changes in equilibrium-line altitude: the case of the Southern Patagonia Icefield. *Journal of Glaciology*, **60**(219), 14-28.

Deng, G., Tang, Z., Hu, G., Wang, J., Sang, G. and Li, J. (2021). Spatiotemporal dynamics of snowline altitude and their responses to climate change in the Tienshan Mountains, Central Asia, During 2001–2019. *Sustainability*, **13**(7), 3992.

Deng, K., Azorin-Molina, C., Yang, S., Hu, C., Zhang, G., Minola, L. and Chen, D. (2022). Changes of Southern Hemisphere westerlies in the future warming climate. *Atmospheric Research*, **270**, 106040.

Ding, M., Han, W., Zhang, T., Yue, X., Fyke, J., Liu, G. and Xiao, C. (2020). Towards more snow days in summer since 2001 at the Great Wall Station, Antarctic Peninsula: The role of the Amundsen Sea low. *Advances in Atmospheric Sciences*, **37**, 494-504.

Dong, Y., Zhao, J., Floricioiu, D., Krieger, L., Fritz, T., and Eineder, M. (2021). High-resolution topography of the Antarctic Peninsula combining the TanDEM-X DEM and Reference Elevation Model of Antarctica (REMA) mosaic. *The Cryosphere*, **15**, 4421–4443.

Dozier, J. (1989) Spectral Signature of Alpine Snow Cover from the Landsat Thematic Mapper. *Remote Sensing of Environment*, **28**, 9–22.

Drenkhan, F., Guardamino, L., Huggel, C. and Frey, H. (2018). Current and future glacier and lake assessment in the deglaciating Vilcanota-Urubamba basin, Peruvian Andes. *Global and Planetary Change*, **169**, 105-118.

Dussaillant, I., Berthier, E., Brun, F., Masiokas, M., Hugonnet, R., Favier, V. and Ruiz, L. (2019). Two decades of glacier mass loss along the Andes. *Nature Geoscience*, **12**(10), 802-808.

Engel, Z., Láska, K., Kavan, J., and Smolíková, J. (2023) Persistent mass loss of Triangular Glacier, James Ross Island, north-eastern Antarctic Peninsula. *Journal of Glaciology*, **69**(273), 27-39.

Engel, Z., Láska, K., Nývlt, D., and Stachoň, Z. (2018). Surface mass balance of small glaciers on James Ross Island, north-eastern Antarctic Peninsula, during 2009–2015. *Journal of Glaciology*, **64**(245), 349-361.

Falaschi, D., Bravo, C., Masiokas, M., Villalba, R., and Rivera, A. (2013). First glacier inventory and recent changes in glacier area in the Monte San Lorenzo Region (47 S), Southern Patagonian Andes, South America. *Arctic, Antarctic, and Alpine Research*, **45**(1), 19-28.

Falaschi, D., Rivera, A., Lo Vecchio Repetto, A., Moragues, S., Villalba, R., Rastner, P., et al. (2021). Evolution of surface characteristics of three debris-covered glaciers in the Patagonian Andes From 1958 to 2020. *Frontiers in Earth Science*, **9**, 671854.

Falk, U., Gieseke, H., Kotzur, F., and Braun, M. (2016) Monitoring snow and ice surfaces on King George Island, Antarctic Peninsula, with high-resolution TerraSAR-X time series. *Antarctic Science*, **28**(2), 135-149.

Fang, H., Baiping, Z., Yonghui, Y., Yunhai, Z., and Yu, P. (2011). Mass elevation effect and its contribution to the altitude of snowline in the Tibetan Plateau and surrounding areas. *Arctic, Antarctic, and Alpine Research*, **43**(2), 207-212.

Farías-Barahona, D., Ayala, Á., Bravo, C., Vivero, S., Seehaus, T., Vijay, S., et al. (2020). 60 years of glacier elevation and mass changes in the Maipo River Basin, central Andes of Chile. *Remote Sensing*, **12**(10), 1658.

Favier, V., Wagnon, P., Chazarin, J. P., Maisincho, L., and Coudrain, A. (2004). One-year measurements of surface heat budget on the ablation zone of Antizana Glacier 15, Ecuadorian Andes. *Journal of Geophysical Research: Atmospheres*, **109**(D18).

Fitzharris, B. (2007). How vulnerable is New Zealand to the impacts of climate change?. *New Zealand Geographer*, **63**(3), 160-168.

Fitzharris, B., Lawson, W., and Owens, I. (1999) Research on glaciers and snow in New Zealand. *Progress in Physical Geography: Earth and Environment*, **23**(4), 469–500.

Fitzharris, B.B., Clare, G.R. and Renwick, J. (2007) Teleconnections between Andean and New Zealand glaciers. *Global and Planetary Change*, **59**(1-4), 159-174.

Fogt, R. L. and Marshall, G. J. (2020). The Southern Annular Mode: variability, trends, and climate impacts across the Southern Hemisphere. *Wiley Interdisciplinary Reviews: Climate Change*, **11**(4), e652.

Fox-Kemper, B., Hewitt, H.T., Xiao, C., Aðalgeirsdóttir, G., Drijfhout, S.S., Edwards, T.L., et al. (2021). Ocean, Cryosphere and Sea Level Change. *Climate Change 2021: The Physical Science Basis. Contribution of Working Group I to the Sixth Assessment Report of the Intergovernmental Panel on Climate Change.* Cambridge University Press: Cambridge, UK, 1211–1362.

Francou, B., Vuille, M., Favier, V., and Cáceres, B. (2004) New evidence for an ENSO impact on low-latitude glaciers: Antizana 15, Andes of Ecuador, 0°28′ S. *Journal of Geophysical. Research,* **109**, D18106.

Francou, B., Vuille, M., Wagnon, P., Mendoza, J. and Sicart, J. E. (2003). Tropical climate change recorded by a glacier in the central Andes during the last decades of the twentieth century: Chacaltaya, Bolivia, 16 S. *Journal of Geophysical Research: Atmospheres*, **108**(D5).

Fu, W., Li, X., Wang, M. and Liang, L. (2020) Delineation of radar glacier zones in the Antarctic Peninsula using polarimetric SAR. *Water*, **12**(9), 2620.

Fyffe, C. L., Potter, E., Fugger, S., Orr, A., Fatichi, S., Loarte, E., Medina, K., Hellström, R., Bernat, M., Aubry-Wake, C., Gurgiser, W., Perry, B., Suarez, W., Quincey, D.J., and Pellicciotti, F. (2021). The energy and mass balance of Peruvian glaciers. *Journal of Geophysical Research: Atmospheres*, **126**(23), e2021JD034911.

Fyffe, C.L., Potter, E., Fugger, S., Orr, A., Fatichi, S., and Loarte, E. (2021) The Energy and Mass Balance of Peruvian Glaciers. *Journal of Geophyical Research: Atmospheres,* **126**(23), e2021JD034911.

Gaddam, V.K., Boddapati, R., Kumar, T., Kulkarni, A.V., and Bjornsson, H. (2022) Application of "OTSU"—an image segmentation method for differentiation of snow and ice regions of glaciers and assessment of mass

budget in Chandra basin, Western Himalaya using Remote Sensing and GIS techniques. *Environmental Monitoring and Assessment,* **194**, 337.

Gallée, H., Guyomarc'h, G., and Brun, E. (2001). Impact of snow drift on the Antarctic ice sheet surface mass balance: possible sensitivity to snow-surface properties. *Boundary-Layer Meteorology*, **99**, 1-19.

Gardner, A.S., Moholdt, G., Cogley, J.G., Wouters, B., Arendt, A.A., Wahr, J., Berthier, E., Hock, R., Pfeffer, W.T., Kaser, G. and Ligtenberg, S.R. (2013) A reconciled estimate of glacier contributions to sea level rise: 2003 to 2009. *Science*, **340**(6134), 852-857.

Garreaud, R. D., Alvarez-Garreton, C., Barichivich, J., Boisier, J. P., Christie, D., Galleguillos, M., et al. (2017). The 2010–2015 megadrought in central Chile: Impacts on regional hydroclimate and vegetation. *Hydrology and earth system sciences*, **21**(12), 6307-6327.

Garreaud, R. D., Boisier, J. P., Rondanelli, R., Montecinos, A., Sepúlveda, H. H. and Veloso-Aguila, D. (2020). The central Chile mega drought (2010–2018): a climate dynamics perspective. *International Journal of Climatology*, **40**(1), 421-439.

Garreaud, R., Lopez, P., Minvielle, M. and Rojas, M. (2013). Large-scale control on the Patagonian climate. *Journal of Climate*, **26**(1), 215-230.

Garreaud, R.D. (2009) The Andes climate and weather. *Advances in Geosciences*, **22**, 3–11.

Garreaud, R.D., Alvarez-Garreton, C., Barichivich, J., Boisier, J.P., Christie, D., Galleguillos, M., LeQuesne, C., McPhee, J. and Zambrano-Bigiarini. M. (2017) The 2010–2015 megadrought in central Chile: impacts on regional hydroclimate and vegetation. *Hydrology and Earth System Sciences,* **21**, 6307–6327.

Gillett, S., and Cullen, N. J. (2011). Atmospheric controls on summer ablation over Brewster Glacier, New Zealand. *International Journal of Climatology*, **31**(13), 2033-2048.

Girona-Mata, M., Miles, E.S., Ragettli, S. and Pellicciotti, F. (2019) High-resolution snowline delineation from Landsat imagery to infer snow cover controls in a Himalayan catchment. *Water Resources Research*, **55**(8), 6754-6772.

GLIMS and NSIDC (2005, updated 2018) Global Land Ice Measurements from Space glacier database (GLIMS). Available at: http://glims.colorado.edu/glacierdata/ [accessed 01/10/22].

González-Herrero, S., Barriopedro, D., Trigo, R. M., López-Bustins, J. A., and Oliva, M. (2022). Climate warming amplified the 2020 record-breaking heatwave in the Antarctic Peninsula. *Communications Earth and Environment*, **3**(1), 122.

González-Herrero, S., Vasallo, F., Bech, J., Gorodetskaya, I., Elvira, B., and Justel, A. (2023). Extreme precipitation records in Antarctica. *International Journal of Climatology*, **43**(7), 3125-3138.

Gonzalez, S., Vasallo, F., Recio-Blitz, C., Guijarro, J. A. and Riesco, J. (2018). Atmospheric patterns over the Antarctic Peninsula. *Journal of Climate*, **31**(9), 3597-3608.

Goyal, R., Sen Gupta, A., Jucker, M. and England, M. H. (2021). Historical and projected changes in the Southern Hemisphere surface westerlies. *Geophysical Research Letters*, **48**(4), e2020GL090849.

Guo, Z., Wang, N., Shen, B., Gu, Z., Wu, Y. and Chen, A. (2021) Recent spatiotemporal trends in glacier snowline altitude at the end of the melt season in the Qilian Mountains, China. *Remote Sensing*, **13**(23), 4935.

Gurgiser, W., Marzeion, B., Nicholson, L., Ortner, M., and Kaser, G. (2013). Modeling energy and mass balance of Shallap Glacier, Peru. *The Cryosphere*, **7**(6), 1787-1802.

Hall, D.K., Ormsby, J.P., Bindschadler, R.A., and Siddalingaiah, H. (1987) Characterization of Snow and Ice Reflectance Zones on Glaciers Using Landsat TM Data. *Annals of Glaciology*, **9**, 104–108.

Hall, D.K., Riggs, G.A. and Salomonson, V.V. (1995) Development of methods for mapping global snow cover using moderate resolution imaging spectroradiometer data. *Remote sensing of Environment*, **54**(2), 127-140.

Hanshaw, M. N. and Bookhagen, B. (2014) Glacial areas, lake areas, and snow lines from 1975 to 2012: status of the Cordillera Vilcanota, including the Quelccaya Ice Cap, northern central Andes, Peru. *The Cryosphere*, **8**, 359–376.

Henderson, R. D., and Thompson, S. M. (1999). Extreme Rainfalls in the Southern Alps of New Zealand. *Journal of Hydrology (New Zealand)*, **38**(2), 309–330.

Hock, R., Rasul, G., Adler, C., Cáceres, B., Gruber, S., Hirabayashi, Y., Jackson, M., Kääb, A., Kang, S., Kutuzov, S., Milner, A., Molau, U., Morin, S., Orlove, B. and Steltzer, H. (2019) *High Mountain Areas. In: IPCC Special Report on the Ocean and Cryosphere in a Changing Climate.* Cambridge: Cambridge University Press.

Hofer, S., Tedstone, A. J., Fettweis, X. and Bamber, J. L. (2017). Decreasing cloud cover drives the recent mass loss on the Greenland Ice Sheet. *Science Advances*, **3**(6), e1700584.

Hofmeister, F., Arias-Rodriguez, L.F., Premier, V., Marin, C., Notarnicola, C., Disse, M. and Chiogna, G. (2022) Intercomparison of Sentinel-2 and modelled snow cover maps in a high-elevation Alpine catchment. *Journal of Hydrology*, **15**, 100123.

Huang, L., Li, Z., Tian, BS, Chen, Q., Liu, JL, and Zhang, R. (2011). Classification and snow line detection for glacial areas using the polarimetric SAR image. *Remote Sensing of Environmen*, **115** (7), 1721-1732.

Huber, J., Cook, A. J., Paul, F., and Zemp, M. (2017). A complete glacier inventory of the Antarctic Peninsula based on Landsat 7 images from 2000 to 2002 and other pre-existing data sets. *Earth system science data*, **9**(1), 115-131.

Hugonnet, R., McNabb, R., Berthier, E., Menounos, B., Nuth, C., Girod, L., Farinotti, D., Huss, M., Dussaillant, I., Brun, F. and Kääb, A. (2021) Accelerated global glacier mass loss in the early twenty-first century. *Nature*, **592**(7856), 726-731.

Huss, M. and Hock, R. (2018) Global-scale hydrological response to future glacier mass loss. *Nature Climate Change*, **8**, 135–140.

Imfeld, N., Sedlmeier, K., Gubler, S., Correa Marrou, K., Davila, C. P., Huerta, A., et al. (2021). A combined view on precipitation and temperature climatology and trends in the southern Andes of Peru. *International journal of climatology*, **41**(1), 679-698.

Jasrotia, A.S., Kour, R. and Ashraf, S. (2022) Impact of illumination gradients on the raw, atmospherically and topographically corrected snow and vegetation areas of Jhelum basin, Western Himalayas. *Geocarto International*, **37**(26), 14027-14049.

Jiang, S., Shi, G., Cole-Dai, J., Wang, M., Li, Y., Wu, G., An, C., and Sun, B. (2023). Perchlorate in Year-Round Antarctic Precipitation. *Geophysical Research Letters*, **50**(19), e2023GL104399.

Jones, J., Gille, S., Goosse, H., Abram, N.J., Canziani, P.O., Charman, D.J., Clem, K.R., Crosta, X., de Lavergne, C., Eisenman, I., England, M.H., Fogt, R.L., Frankcombe, L.M., Marshall, G.J., Masson-Delmotte, V., Morrison, A.K., Orsi, A.J., Raphael, M.N., Renwick, J.A., Schneider, D.P., Simpkins, G.R., Steig, E.J., Stenni, B., Swingedouw, D. and Vance, T.R. (2016) Assessing recent trends in high-latitude Southern Hemisphere surface climate. *Nature Climate Change*, **6**, 917–926.

Kaser, G. (1995). Some notes on the behaviour of tropical glaciers. *Bulletin de l'Institut Français d'Études Andines*, **24**(3), 671-681.

Kaser, G. (2001). Glacier-climate interaction at low latitudes. *Journal of Glaciology*, **47**(157), 195-204.

Kaser, G. (2001). Glacier-climate interaction at low latitudes. *Journal of Glaciology*, **47**(157), 195-204.

Kaser, G. and Georges, C. (1997). Changes of the equilibrium-line altitude in the tropical Cordillera Blanca, Peru, 1930–50, and their spatial variations. *Annals of Glaciology*, **24**, 344-349.

Kaser, G. and Osmaston, H. (2002) *Tropical glaciers*. Cambridge: Cambridge University Press.

Kaser, G., Ames, A., and Zamora, M. (1990). Glacier fluctuations and climate in the Cordillera Blanca, Peru. *Annals of Glaciology*, **14**, 136-140.

Kaser, G., Fountain, A., Jansson, P., Heucke, E. and Knaus, M. (2003) *A manual for monitoring the mass balance of mountain glaciers.* Paris: Unesco.

Kim, J. W., Yeh, S. W., and Chang, E. C. (2014). Combined effect of El Niño-Southern Oscillation and Pacific decadal oscillation on the East Asian winter monsoon. *Climate dynamics*, **42**, 957-971.

Kingslake, J., Ely, J. C., Das, I. and Bell, R. E. (2017). Widespread movement of meltwater onto and across Antarctic ice shelves. *Nature*, **544**(7650), 349-352.

Kinnard, C., Ginot, P., Surazakov, A., Macdonell, S., Nicholson, L.I., Patris, N., Rabatel, A., Rivera, A. and Squeo, F. (2020) Mass-balance and climate history of a high-altitude glacier, Desert Andes of Chile. *Frontiers in Earth Science*, **8**, 40.

Kirkbride, M. P., and Winkler, S. (2012). Correlation of Late Quaternary moraines: impact of climate variability, glacier response, and chronological resolution. *Quaternary Science Reviews*, **46**, 1-29.

Laffin, M. K., Zender, C. S., Singh, S., Van Wessem, J. M., Smeets, C. J. P. P. and Reijmer, C. H. (2021). Climatology and evolution of the Antarctic Peninsula föhn wind-induced melt regime from 1979–2018. *Journal of Geophysical Research: Atmospheres*, **126**(4), e2020JD033682.

Lehner, B. and Grill G. (2013) Global river hydrography and network routing: baseline data and new approaches to study the world's large river systems. *Hydrological Processes*, **27**(15), 2171-2186.

Leysinger Vieli, G. M., and Gudmundsson, G. H. (2004). On estimating length fluctuations of glaciers caused by changes in climatic forcing. *Journal of Geophysical Research: Earth Surface*, **109**(F1).

Li, X., Wang, N., and Wu, Y. (2022). Automated Glacier Snow Line Altitude Calculation Method Using Landsat Series Images in the Google Earth Engine Platform. *Remote Sensing*, **14**(10), 2377.

Lim, E. P., Hendon, H. H., Arblaster, J. M., Delage, F., Nguyen, H., Min, S. K. and Wheeler, M. C. (2016). The impact of the Southern Annular Mode on future changes in Southern Hemisphere rainfall. *Geophysical Research Letters*, **43**(13), 7160-7167.

Liu, C., Li, Z., Zhang, P., Tian, B., Zhou, J., and Chen, Q. (2021). Variability of the snowline altitude in the eastern Tibetan Plateau from 1995 to 2016 using Google Earth Engine. *Journal of Applied Remote Sensing*, **15**(4), 048505.

Liu, Y., Moore, J. C., Cheng, X., Gladstone, R. M., Bassis, J. N., Liu, H., Wen, J., and Hui, F. (2015). Ocean-driven thinning enhances iceberg calving and retreat of Antarctic ice shelves. *Proceedings of* Alexander, D., Shulmeister, J., and Davies, T. (2011). High basal melting rates within high-precipitation temperate glaciers. *Journal of Glaciology*, **57**(205), 789-795.

Lliboutry, L. (1965). Traité de glaciologie.

Lliboutry, L. (1998). Glaciers of Chile and Argentina. In R. S. WilliamsJr, & J. G. Ferrigno (Eds.), *Satellite image atlas of glaciers of the world. Professional Paper 1386-I-6*. U.S. Geological Survey.

Loibl, D., Richter, N., and Grünberg, I. (2022) Remote sensing-derived time series of transient snowline altitudes for High Mountain Asia, 1986-2021 [preprint]. Available at: https://doi.org/10.31223/X5WH2D [accessed 25/10/22].

López-Moreno, J. I., Valero-Garcés, B., Mark, B., Condom, T., Revuelto, J., Azorín-Molina, C., et al. (2017). Hydrological and depositional processes associated with recent glacier recession in Yanamarey catchment, Cordillera Blanca (Peru). *Science of the Total Environment*, **579**, 272-282.

López-Moreno, J.I., Fontaneda, S., Bazo, J., Revuelto, J., Azorin-Molina, C., Valero-Garcés, B., Morán-Tejeda, E., Vicente-Serrano, S.M., Zubieta, R. and Alejo-Cochachín, L. (2014) Recent glacier retreat and climate trends in Cordillera Huaytapallana, Peru. *Global and Planetary Change*, **112**, 1-11.

López-Moreno, J. I., Nogués-Bravo, D., Chueca-Cía, J. and Julián-Andrés, A. (2006). Glacier development and topographic context. *Earth Surface Processes and Landforms: The Journal of the British Geomorphological Research Group*, **31**(12), 1585-1594.

López-Moreno, J. I., Rojas-Heredia, F., Ceballos, J. L., Morán-Tejeda, E., Alonso-Gonzalez, E., Vidaller, I., et al. (2022). Recent evolution of glaciers in the Cocuy-Güican Mountains (Colombian Andes) and the hydrological implications. *Land Degradation & Development*, **33**(14), 2606-2618.

Lorrey, A., Vargo, L., Purdie, H., Anderson, B., Cullen, N., Sirguey, P., Mackintosh, A., Willsman, A., Macara, G. and Chinn, W. (2022) Southern Alps equilibrium line altitudes: Four decades of observations show coherent glacier–climate responses and a rising snowline trend. *Journal of Glaciology*, **68**(272), 1127-1140.

Lynch, B. D. (2012). Vulnerabilities, competition and rights in a context of climate change toward equitable water governance in Peru's Rio Santa Valley. *Global Environmental Change*, **22**(2), 364-373.

MacDonald, M. K., Pomeroy, J. W., and Pietroniro, A. (2010). On the importance of sublimation to an alpine snow mass balance in the Canadian Rocky Mountains. *Hydrology and Earth System Sciences*, **14**(7), 1401-1415.

Mackintosh, A. N., Anderson, B. M., Lorrey, A. M., Renwick, J. A., Frei, P., and Dean, S. M. (2017). Regional cooling caused recent New Zealand glacier advances in a period of global warming. *Nature Communications*, **8**(1), 14202.

Malmros, J. K., Mernild, S. H., Wilson, R., Yde, J. C., and Fensholt, R. (2016). Glacier area changes in the central Chilean and Argentinean Andes 1955–2013/14. *Journal of Glaciology*, **62**(232), 391-401.

Mann, M.E., Zhang, Z., Hughes, M.K., Bradley, R.S., Miller, S.K., Rutherford, S., and Ni, F. (2008) Proxy-based reconstructions of hemispheric and global surface temperature variations over the past two millennia. *Proceedings of the National Academy of Sciences*, **105**(36), 13252-13257.

Mao, R., Kim, S. J., Gong, D. Y., Liu, X., Wen, X., Zhang, L., et al. (2021). Increasing difference in interannual summertime surface air temperature between interior East Antarctica and the Antarctic Peninsula under future climate scenarios. *Geophysical Research Letters*, **48**(16), e2020GL092031.

Marinsek, S., and Ermolin, E. (2015). 10 year mass balance by glaciological and geodetic methods of Glaciar Bahía del Diablo, Vega Island, Antarctic Peninsula. *Annals of Glaciology*, **56**(70), 141-146.

Markham, B.L., Storey, J.C., Williams, D.L., and Irons, J.R. (2004) Landsat sensor performance: history and current status. *IEEE transactions on geoscience and remote sensing*, **42**(12), 2691-2694.

Marshall, G. J., Orr, A., van Lipzig, N. P. and King, J. C. (2006). The impact of a changing Southern Hemisphere Annular Mode on Antarctic Peninsula summer temperatures. *Journal of Climate*, **19**(20), 5388-5404.

Martin, J., Davies, B. J., Jones, R., and Thorndycraft, V. (2022). Modelled sensitivity of Monte San Lorenzo ice cap, Patagonian Andes, to past and present climate. *Frontiers in Earth Science*, **10**, 831631.

Masiokas, M. H., Christie, D. A., Le Quesne, C., Pitte, P., Ruiz, L., Villalba, R. and Barcaza, G. (2016). Reconstructing the annual mass balance of the Echaurren Norte glacier (Central Andes, 33.5 S) using local and regional hydroclimatic data. *The Cryosphere*, **10**(2), 927-940.

Masiokas, M.H., Rabatel, A., Rivera, A., Ruiz, L., Pitte, P., Ceballos, J.L., Barcaza, G., Soruco, A., Bown, F., Berthier, E., Dussaillant, I. and MacDonell, S. (2020) A review of the current state and recent changes of the Andean cryosphere. *Frontiers in Earth Science*, **8**(99).

Masiokas, M.H., Villalba, R., Luckman, B., LeQuesne, C., and Aravena, J.C. (2006). Snowpack variations in the central Andes of Argentina and Chile, 1951-2005: large-scale atmospheric influences and implications for water resources in the region. *Journal of Climate*, **19**, 6334–6352.

Matzl, M., and Schneebeli, M. (2006) Measuring specific surface area of snow by near-infrared photography. *Journal of Glaciology*, **52**(179), 558-564.

McFadden, E. M., Ramage, J., and Rodbell, D. T. (2011) Landsat TM and ETM+ derived snowline altitudes in the Cordillera Huayhuash and Cordillera Raura, Peru, 1986–2005. *The Cryosphere*, **5**, 419–430.

Meier, M. E and Post, A. S. (1962) Recent variations in mass net budgets of glaciers in western North America. *Proceedings of Ohergurgl Symposium*, **58**, 63-77.

Meier, M. E. (1961) Mass budget of South Cascade Glacier, 1957-60. *United States Geological Survey Professional Paper*. Publication 242-B, 206-211.

Melkonian, A.K., Willis, M.J., Pritchard, M.E., Rivera, A., Bown, F. and Bernstein, S.A. (2013) Satellite-derived volume loss rates and glacier speeds for the Cordillera Darwin Icefield, Chile. *Cryosphere*, **7**, 823–839.

Mernild, S. H., Liston, G. E., Hiemstra, C. and Wilson, R. (2017). The Andes Cordillera. Part III: glacier surface mass balance and contribution to sea level rise (1979–2014). *International Journal of Climatology*, **37**(7), 3154-3174.

Mernild, S.H., Liston, G.E., Hiemstra, C.A., Yde, J.C., McPhee, J., and Malmros, J.K. (2016) The Andes Cordillera. Part II: Rio Olivares Basin snow conditions (1979–2014), central Chile. *International Journal of Climatology*, **37**(4), 1699-1715.

MetService (2023) New Zealand Climate. Available online: https://about.metservice.com/our-company/learning-centre/new-zealand-climate/ [accessed 20/08/23].

Milner, A.M., Khamis, K., Battin, T.J., Brittain, J.E., Barrand, N.E., Füreder, L., Cauvy-Frauni, S., Gíslason, G.M., Jacobsen, D., Hannah, D.M., Hodson, A.J., Hood, E., Lencioni, V., Ólafsson, J.S., Robinson, C.T., Tranter, M., and Brown, L.E. (2017) Glacier shrinkage driving global changes in downstream systems. *PNAS*, **114**(37), 970-9778.

Minowa, M., Schaefer, M., Sugiyama, S., Sakakibara, D. and Skvarca, P. (2021). Frontal ablation and mass loss of the Patagonian icefields. *Earth and Planetary Science Letters*, **561**, 116811.

Minowa, M., Skvarca, P., and Fujita, K. (2023). Climate and Surface Mass Balance at Glaciar Perito Moreno, Southern Patagonia. *Journal of Climate*, **36**(2), 625-641.

Moreno, P. I., Francois, J. P., Moy, C. M. and Villa-Martínez, R. (2010). Covariability of the Southern Westerlies and atmospheric CO2 during the Holocene. *Geology*, **38**(8), 727-730.

Morris, E.M. and Vaughan, D. (2003) Spatial and Temporal Variation of Surface Temperature on the Antarctic Peninsula And The Limit of Viability of Ice Shelves. *Antarctic Peninsula Climate Variability: Historical and Paleoenvironmental Perspectives*, **79**, 61-68

Mukul, M., Srivastava, V., Jade, S., and Mukul, M. (2017) Uncertainties in the shuttle radar topography mission (SRTM) heights: insights from the Indian Himalaya and Peninsula. *Scientific Reports*, **7**, 41672.

Mullan, A. B., Sood, A. and Stuart, S. (2018). Climate Change Projections for New Zealand: Atmosphere Projections Based on Simulations from the IPCC Fifth Assessment Wellington: Ministry for the Environment. Available online: https://environment.govt.nz/assets/Publications/Files/Climate-change-projections-2nd-edition-final.pdf [accessed 20/08/23].

Mulvaney, R., Abram, N. J., Hindmarsh, R. C., Arrowsmith, C., Fleet, L., Triest, J., et al. (2012). Recent Antarctic Peninsula warming relative to Holocene climate and ice-shelf history. *Nature*, **489**(7414), 141-144.

Muñoz-Sabater, J. (2019) ERA5-Land monthly averaged data from 1981 to present. Copernicus Climate Change Service (C3S) Climate Data Store (CDS) [accessed 10/12/22].

Mutz, S. G., and Aschauer, J. (2022). Empirical glacier mass-balance models for South America. *Journal of Glaciology*, **68**(271), 912-926.

Navarro, F. J., Jonsell, U. Y., Corcuera, M. I., and Martín-Español, A. (2013). Decelerated mass loss of Hurd and Johnsons Glaciers, Livingston Island, Antarctic Peninsula. *Journal of Glaciology*, **59**(213), 115-128.

Navarro, F.J., Jonsell, U.Y., Corcuera, M.I. and Martín-Español, A. (2013) Decelerated mass loss of Hurd and Johnsons Glaciers, Livingston Island, Antarctic Peninsula. *Journal of Glaciology*, **59**(213), 115-128.

Neukom, R., Gergis, J., Karoly, D., Wanner, H., Curran, M., Elbert, J., González-Rouco, F., Linsley, B.K., Moy, A.D., Mundo, I., Raible, C.C., Steig, E.J., van Ommen, T., Vance, T., Villalba, R., Zinke, J. and Frank, D. (2014) Inter-hemispheric temperature variability over the past millennium. *Nature Climate Change*, **4**, 362–367.

Neukom, R., Rohrer, M., Calanca, P., Salzmann, N., Huggel, C., Acuña, D., et al. (2015). Facing unprecedented drying of the Central Andes? Precipitation variability over the period AD 1000–2100. *Environmental Research Letters*, **10**(8), 084017.

NIWA (2012). Understanding New Zealand's mountain climate. Available online: https://niwa.co.nz/sites/niwa.co.nz/files/umc_program_and_abstracts_2012.pdf [accessed 20/08/23].

NIWA (2016). Seasonal Climate Summary: Summer 2015-16 Available online: https://niwa.co.nz/sites/niwa.co.nz/files/Climate_Summary_Summer_2016_FINAL.pdf [accessed 20/08/23].

NIWA (no date). Overview of New Zealand's climate. Available online: https://niwa.co.nz/education-and-training/schools/resources/climate/overview#:~:text=New%20Zealand's%20climate%20is%20complex,conditions%20in%20the%20mountainous%20areas [accessed 20/08/23].

Oerlemans, J. (1994) Quantifying global warming from the retreat of glaciers. *Science*, **264**(5156), 243-245.

Oerlemans, J. (2012). Linear modelling of glacier length fluctuations. *Geografiska Annaler: Series A, Physical Geography*, **94**(2), 183-194.

Oerlemans, J., and Reichert, B. K. (2000). Relating glacier mass balance to meteorological data by using a seasonal sensitivity characteristic. *Journal of Glaciology*, **46**(152), 1-6.

Ohmura, A., Kasser, P. and Funk, M. (1992) Climate at the equilibrium line of glaciers. *Journal of Glaciology*, **38**(130), 397- 411.

Oliva, M., Navarro, F., Hrbáček, F., Hernandéz, A., Nývlt, D., Pereira, P., Ruiz-Fernández, J. and Trigo, R. (2017). Recent regional climate cooling on the Antarctic Peninsula and associated impacts on the cryosphere. *Science of the Total Environment*, **580**, 210-223.

Oliver, E. C., Benthuysen, J. A., Bindoff, N. L., Hobday, A. J., Holbrook, N. J., Mundy, C. N., and Perkins-Kirkpatrick, S. E. (2017). The unprecedented 2015/16 Tasman Sea marine heatwave. *Nature communications*, **8**(1), 16101.

Osmanoglu, B., Navarro, F. J., Hock, R., Braun, M., and Corcuera, M. I. (2014). Surface velocity and mass balance of Livingston Island ice cap, Antarctica. *The Cryosphere*, **8**(5), 1807-1823.

Otsu, N. (1979) A threshold selection method from gray-level histograms. *IEEE Transactions on Systems, Man, and Cybernetics*, **9**, 62–66.

Pabón-Caicedo, J. D., Arias, P. A., Carril, A. F., Espinoza, J. C., Borrel, L. F., Goubanova, K., et al. (2020). Observed and projected hydroclimate changes in the Andes. *Frontiers in Earth Science*, **8**, 61.

Pandey, P., Kulkarni, AV, and Venkataraman, G. (2013). Remote sensing study of snowline altitude at the end of melting season, Chandra-Bhaga basin, Himachal Pradesh, 1980– 2007. *Geocard International*, **28** (4), 311-322.

Parajka, J., Pepe, M., Rampini, A., Rossi, S. and Blöschl, G. (2010) A regional snow-line method for estimating snow cover from MODIS during cloud cover. *Journal of Hydrology*, **381**(3-4), 203-212.

Parla, A., Koppes, M.N., and Coops, N.C. (2020) Glacier Snowline Altitude Mapping in the Canadian High Arctic Using Feature-Oriented Principle Component Analysis. *AGU Fall Meeting Abstracts*, **2020**, C027-07.

Paterson, W.S.B. (1994) *The Physics of Glaciers*, 3rd ed. Oxford: Elsevier Science.

Patterson, M., Bracegirdle, T. and Woollings, T. (2019). Southern Hemisphere atmospheric blocking in CMIP5 and future changes in the Australia-New Zealand sector. *Geophysical Research Letters*, **46**(15), 9281-9290.

Paul, F., Barrand, N.E., Baumann, S., Berthier, E., Bolch, T., Casey, K., Frey, H., Joshi, S.P., Konovalov, V., Le Bris, R., Mölg, N., Nosenko, G., Nuth, C., Pope, A., Racoviteanu, A., Rastner, P., Raup, B., Scharrer, K., Steffen, S., and Winsvold, S. (2013) On the accuracy of glacier outlines derived from remote-sensing data. *Annals of Glaciology*, **54**(63), 171-182.

Pelto, M. (2011) Utility of late summer transient snowline migration rate on Taku Glacier, Alaska. *The Cryosphere*, **5**, 1127-1133.

Pérez, T., Mattar, C. and Fuster, R. (2018). Decrease in snow cover over the Aysén river catchment in Patagonia, Chile. *Water*, **10**(5), 619.

Pfeffer, W.T., Arendt, A.A., Bliss, A., Bolch, T., Cogley, J.G., Gardner, A.S., Hagen, J., Hock, R., Kaser, G., Kienholz, C., Miles, E.S., Moholdt, G., Mölg, N., Paul, F., Radić, V., Rastner, P., Raup, B.H., Rich, J., Sharp, M.J. and The Randolph Consortium (2014) The Randolph Glacier Inventory: a globally complete inventory of glaciers. *Journal of Glaciology*, **60**(221), 537-552.

Poortinga, A., Tenneson, K., Shapiro, A., Nquyen, Q., Aung, K.S., Chishtie, F., and Saah, D. (2019) Mapping Plantations in Myanmar by Fusing Landsat-8, Sentinel-2 and Sentinel-1 Data along with Systematic Error Quantification. *Remote Sensing*, **11**(7), 831.

Porhemmat, R., Purdie, H., Zawar-Reza, P., Zammit, C., and Kerr, T. (2021). The influence of atmospheric circulation patterns during large snowfall events in New Zealand's Southern Alps. *International Journal of Climatology*, **41**(4), 2397-2417.

Potter, E. R., Fyffe, C. L., Orr, A., Quincey, D. J., Ross, A. N., Rangecroft, S., et al. (2023). A future of extreme precipitation and droughts in the Peruvian Andes. *Climate and Atmospheric Science*, **6**(1), 96.

Poveda, G., Espinoza, J. C., Zuluaga, M. D., Solman, S. A., Garreaud, R., and Van Oevelen, P. J. (2020). High impact weather events in the Andes. *Frontiers in Earth Science*, **8**, 162.

Prieur, C., Rabatel, A., Thomas, J.B., Farup, I., and Chanussot, J. (2022) Machine Learning Approaches to Automatically Detect Glacier Snow Lines on Multi-Spectral Satellite Images. *Remote Sensing*, **14**(16), 3868.

Prudente, V.H.R., Martins, V.S., Vieira, D.C., Rodrigues de França e Silva, N., Adami, M., and Sanches, I.D. (2020) Limitations of cloud cover for optical remote sensing of agricultural areas across South America. *Remote Sensing Applications: Society and Environment*, **20**, 100414.

Purdie, H. L., Brook, M. S. and Fuller, I. C. (2008). Seasonal variation in ablation and surface velocity on a temperate maritime glacier: Fox Glacier, New Zealand. *Arctic, Antarctic, and Alpine Research*, **40**(1), 140-147.

Purdie, H., Kerr, T., Rack, W., and Lorrey, A. (2021). *Rolleston Glacier: First decade of mass balance measurement and the implications of climate change on mass balance monitoring.* University of Canterbury, Christchurch, New Zealand: The Snow and ice Research Group Workshop: Understanding Mountain Climate II. 09/02/2021-13/02/2021.

Purdie, H., Mackintosh, A., Lawson, W., and Anderson, B. (2011) Synoptic influences on snow accumulation on glaciers east and west of a topographic divide: Southern Alps, New Zealand. *Arctic, Antarctic, and Alpine Research*, **43**(1), 82-94.

Purdie, H., Mackintosh, A., Lawson, W., and Anderson, B. (2011). Synoptic influences on snow accumulation on glaciers east and west of a topographic divide: Southern Alps, New Zealand. *Arctic, Antarctic, and Alpine Research*, **43**(1), 82-94.

Purdie, J. (2022). Modelling climate change impacts on inflows, lake storage and spill in snow-fed hydroelectric power catchments, Southern Alps, New Zealand. *Journal of Hydrology (New Zealand)*, **61**(2), 151-178.

Qixiang, W., Wang, M., and Xiaohui, F. (2018) Seasonal patterns of warming amplification of high-elevation stations across the globe. *International Journal of Climatology*, **38**(6), 1-8.

Rabatel, A., Bermejo, A., Loarte, E., Soruco, A., Gomez, J., Leonardini, G., Vincent, C. and Sicart, J.E. (2012) Can the snowline be used as an indicator of the equilibrium line and mass balance for glaciers in the outer tropics? *Journal of Glaciology*, **58**(212), 1027-1036.

Rabatel, A., Castebrunet, H., Favier, V., Nicholson, L., and Kinnard, C. (2011). Glacier changes in the Pascua-Lama region, Chilean Andes (29 S): recent mass balance and 50 yr surface area variations. *The Cryosphere*, **5**(4), 1029-1041.

Rabatel, A., Dedieu, J.P., and Vincent, C. (2005) Using Remote-Sensing Data to Determine Equilibrium-Line Altitude and Mass-Balance Time Series: Validation on Three French Glaciers, 1994-2002. *Journal of Glaciology*, **51**(175), 539–546.

Rabatel, A., Francou, B., Soruco, A., Gomez, J., Cáceres, B., Ceballos, J. L., Bastantes, R., Vuille, M., Sicart, J.E., Huggel, C., Scheel, M., Lejeune, Y., Arnaud, Y., Collet, M., Condom, T., Consoli, G., Favier, V., Jomelli, V., Galarraga, R., Ginot, P., Maisincho, L., Mendoza, J., Ménégoz, M., Ramirez, E., Ribstein, P., Suarez, W., Villacis, M. and Wagnon, P. (2013). Current state of glaciers in the tropical Andes: a multi-century perspective on glacier evolution and climate change. *The Cryosphere*, **7**(1), 81-102.

Racoviteanu, A. E., Rittger, K., and Armstrong, R. (2019). An automated approach for estimating snowline altitudes in the Karakoram and eastern Himalaya from remote sensing. *Frontiers in Earth Science*, **7**, 220.

Raper, S. C., and Braithwaite, R. J. (2009). Glacier volume response time and its links to climate and topography based on a conceptual model of glacier hypsometry. *The Cryosphere*, **3**(2), 183-194.

Rastner, P., Prinz, R., Notarnicola, C., Nicholson, L., Sailer, R., Schwaizer, G., and Paul, F. (2019). On the automated mapping of snow cover on glaciers and calculation of snow line altitudes from multi-temporal landsat data. *Remote Sensing*, **11**, 1410.

Rau, F., Braun, M., Saurer, H., Goßmann, H., Kothe, G., Weber, F., Ebel, M. and Beppler, D. (2000) Monitoring Multi-Year Snow Cover Dynamics on the Antarctic Peninsula Using SAR Imagery. *Polarforschung*, **67**(1-2), 27-40.

Raup, B.H., Racoviteanu, A.E., Khalsa, S.J.S., and Helm, C. (2007) The GLIMS Geospatial Glacier Database: a new tool for studying glacier change. *Global and Planetary Change*, **56**(1), 101-110.

Renwick, J. A. (2011). Kidson's synoptic weather types and surface climate variability over New Zealand. *Weather and Climate*, **31**, 3-23.

Risaro, D. B., Chidichimo, M. P. and Piola, A. R. (2022). Interannual variability and trends of sea surface temperature around southern South America. *Frontiers in Marine Science*, **9**, 829144.

Rivera, A., and Casassa, G. (1999) Volume changes on Pio XI glacier, Patagonia: 1975–1995. *Global and Planetary Change*, **22**(1-4), 233-244.

Rivera, J. A., Penalba, O. C., Villalba, R. and Araneo, D. C. (2017). Spatio-temporal patterns of the 2010–2015 extreme hydrological drought across the Central Andes, Argentina. *Water*, **9**(9), 652.

Rott, H., Abdel Jaber, W., Wuite, J., Scheiblauer, S., Floricioiu, D., Van Wessem, J. M., Nagler, T., Miranda, N. and Van Den Broeke, M. R. (2018). Changing pattern of ice flow and mass balance for glaciers discharging into the Larsen A and B embayments, Antarctic Peninsula, 2011 to 2016. *The Cryosphere*, **12**(4), 1273-1291.

Russell, A. M., Gnanadesikan, A., and Zaitchik, B. (2017). Are the central andes mountains a warming hot spot? *Journal of Climate*, **30**, 3589–3608.

Saavedra, F.A., Kampf, S.K., Fassnacht, S.R. and Sibold, J.S. (2017) A snow climatology of the Andes Mountains from MODIS snow cover data. *International Journal of Climatology*, **37**, 1526-1539.

Saavedra, F.A., Kampf, S.K., Fassnacht, S.R. and Sibold, J.S. (2018) Changes in Andes snow cover from MODIS data, 2000–2016. *The Cryosphere*, **12**, 1027–1046.

Sagredo, E. A., and Lowell, T. V. (2012). Climatology of Andean glaciers: A framework to understand glacier response to climate change. *Global and Planetary Change*, **86**, 101-109.

Salinger, M. J., Diamond, H. J. and Renwick, J. A. (2020). Surface temperature trends and variability in New Zealand and surrounding oceans. *Weather and Climate*, **40**(1), 32-51.

Schaefer, M., Machguth, H., Falvey, M. and Casassa, G. (2013). Modeling past and future surface mass balance of the Northern Patagonia Icefield. *Journal of Geophysical Research: Earth Surface*, **118**(2), 571-588.

Schaefer, M., Machguth, H., Falvey, M., Casassa, G. and Rignot, E. (2015). Quantifying mass balance processes on the Southern Patagonia Icefield. *The Cryosphere*, **9**(1), 25-35.

Schaefer, M., Machguth, H., Falvey, M., Casassa, G., and Rignot, E. (2015). Quantifying mass balance processes on the Southern Patagonia Icefield. *The Cryosphere*, **9**(1), 25-35.

Schauwecker, S. (2011) Near-surface temperature lapse rates in a mountainous catchment in the Chilean Andes.

Schauwecker, S., Rohrer, M., Acuña, D., Cochachin, A., Dávila, L., Frey, H., et al. (2014). Climate trends and glacier retreat in the Cordillera Blanca, Peru, revisited. *Global and Planetary Change*, **119**, 85-97.

Schauwecker, S., Rohrer, M., Huggel, C., Endries, J., Montoya, N., Neukom, R., Perry, B., Salzmann, N., Schwarb, M. and Suarez, W. (2017) The freezing level in the tropical Andes, Peru: An indicator for present and future glacier extents. *Journal of Geophysical Research: Atmospheres*, **122**(10).

Schneider, C. and Gies, D. (2004). Effects of El Niño–southern oscillation on southernmost South America precipitation at 53 S revealed from NCEP–NCAR reanalyses and weather station data. *International Journal of Climatology: A Journal of the Royal Meteorological Society*, **24**(9), 1057-1076.

Schneider, D. P., Okumura, Y., and Deser, C. (2012) Observed Antarctic interannual climate variability and tropical linkages. *Journal of climate*, **25**(12), 4048-4066.

Schuawecker, S., Palma, G., MacDonell, S., Ayala, A. and Viale, M. (2022) The snowline and 0°C isotherm altitudes during precipitation events in the dry subtropical Chilean Andes as seen by citizen science, surface stations, and ERA5 reanalysis data. *Frontiers in Earth Science*, **10**(875795).

Seehaus, T., Cook, A. J., Silva, A. B., and Braun, M. (2018). Changes in glacier dynamics in the northern Antarctic Peninsula since 1985. *The Cryosphere*, **12**(2), 577-594.

Seehaus, T., Malz, P., Sommer, C., Lippl, S., Cochachin, A., and Braun, M. (2019). Changes of the tropical glaciers throughout Peru between 2000 and 2016–mass balance and area fluctuations. *The Cryosphere*, **13**(10), 2537-2556.

Selkirk, P.M. (2007) . The nature and importance of the sub-Antarctic. *Papers and Proceedings of the Royal Society of Tasmania*, **141**(1) , 1-6

Shaw, T. E., Ulloa, G., Farías-Barahona, D., Fernandez, R., Lattus, J. M. and McPhee, J. (2021). Glacier albedo reduction and drought effects in the extratropical Andes, 1986–2020. *Journal of Glaciology*, **67**(261), 158-169.

Shukla, A., Banerjee, A., Fujita, K., Nicholson, L. I., Quincey, D. J., eds. (2022). *Debris-Covered Glaciers: Formation, Governing Processes, Present Status and Future Directions.* Lausanne: Frontiers Media SA.

Sicart, J. E., Espinoza, J. C., Quéno, L., and Medina, M. (2016). Radiative properties of clouds over a tropical Bolivian glacier: seasonal variations and relationship with regional atmospheric circulation. *International Journal of Climatology*, **36**(8), 3116-3128.

Sicart, J. E., Hock, R., Ribstein, P., Litt, M., and Ramirez, E. (2011). Analysis of seasonal variations in mass balance and meltwater discharge of the tropical Zongo Glacier by application of a distributed energy balance model. *Journal of Geophysical Research: Atmospheres*, **116**(D13).

Sicart, J. E., Wagnon, P. and Ribstein, P. (2005). Atmospheric controls of the heat balance of Zongo Glacier (16 S, Bolivia). *Journal of Geophysical Research: Atmospheres*, **110**(D12).

Silva, A. B., Arigony-Neto, J., Braun, M. H., Espinoza, J. M. A., Costi, J., and Jaña, R. (2020). Spatial and temporal analysis of changes in the glaciers of the Antarctic Peninsula. *Global and Planetary Change*, **184**, 103079.

Simões, C. L., Rosa, K. K., Simões, J. C., Vieira, R., Costa, R. M., and Silva, A. B. (2020). Recent changes in two outlet glaciers in the Antarctic Peninsula using multi-temporal Landsat and Sentinel-1 data. *Geocarto International*, **35**(11), 1233-1244.

Simões, C.L., Kellem da Rosa, K., Czapela, F.F., Vieira, R., Simões, J.C. (2015) Collins Glacier retreat process and regional climatic variations, King George Island, Antarctica. *Geographical Review*, **105**(4), 462-471.

Slonaker, R. L., and Van Woert, M. L. (1999). Atmospheric moisture transport across the Southern Ocean via satellite observations. *Journal of Geophysical Research: Atmospheres*, **104**(D8), 9229-9249.

Soenen, S.A., Peddle, D.R., and Coburn, C.A. (2005) SCS+C: A Modified Sun-Canopy-Sensor Topographic Correction in Forested Terrain. *IEEE Transactions on Geoscience and Remote Sensing*, **43**(9), 2148-2159.

Stewart, E.J., Wilson, J., Espiner, S., Purdie, H., Lemieux, C. and Dawson, J. (2016) Implications of climate change for glacier tourism. *Tourism Geographies*, **18**(4), 377-398.

Stichler, W., Schotterer, U., Fröhlich, K., Ginot, P., Kull, C., Gäggeler, H., and Pouyaud, B. (2001). Influence of sublimation on stable isotope records recovered from high-altitude glaciers in the tropical Andes. *Journal of Geophysical Research: Atmospheres*, **106**(D19), 22613-22620.

Stoffel, M. and Huggel, C. (2012) Effects of climate change on mass movements in mountain environments. *Progress in physical geography*, **36**(3), 421-439.

Stringer, C.D. (2022) Contemporary (2016–2020) land cover across West Antarctica and the McMurdo Dry Valleys[Code] (Version 1). Zenodo. Available online: https://doi.org/10.5281/zenodo.6720051 [accessed 13/05/23].

Sulca, J., Vuille, M., Silva, Y. and Takahashi, K. (2016). Teleconnections between the Peruvian Central Andes and Northeast Brazil during extreme rainfall events in austral summer. *Journal of Hydrometeorology*, **17**(2), 499-515.

Tadono, T., Nagai, H., Ishida, H., Oda, F., Naito, S., Minakawa, K., and Iwamoto, H. (2016) Generation of the 30 M-mesh global digital surface model by ALOS PRISM. *International Archives of the Photogrammetry, Remote Sensing and Spatial Information Sciences*, **41**.

Takaku, J., Tadono, T. and Tsutsui, K. (2014) Generation of High Resolution Global DSM from ALOS PRISM. *The International Archives of the Photogrammetry, Remote Sensing and Spatial Information Sciences*, **XL-4**.

Tawde, S. A., Kulkarni, A. V., and Bala, G. (2016). Estimation of glacier mass balance on a basin scale: an approach based on satellite-derived snowlines and a temperature index model. *Current Science*, 1977-1989.

Tawde, S.A., Kulkarni, A.V. and Bala, G. (2016) Estimation of glacier mass balance on a basin scale: an approach based on satellite-derived snowlines and a temperature index model. *Current Science*, 1977-1989.

Taylor, L.S., Quincey, D.J., Smith, M.W., Potter, E.R., Castro, J. and Fyffe, C.L. (2022) Multi-Decadal Glacier Area and Mass Balance Change in the Southern Peruvian Andes. *Frontiers in Earth Science*, **10**.

Thibeault, J., Seth, A. and Wang, G. (2012). Mechanisms of summertime precipitation variability in the Bolivian Altiplano: present and future. *International Journal of Climatology*, **32**(13), 2033-2041.

Thompson, D. W., Solomon, S., Kushner, P. J., England, M. H., Grise, K. M. and Karoly, D. J. (2011). Signatures of the Antarctic ozone hole in Southern Hemisphere surface climate change. *Nature geoscience*, **4**(11), 741-749.

Thornton, J.M., Pepin, N., Shagedanova, M., and Adler, C. (2022) Coverage of In Situ Climatological Observations in the World's Mountains. *Frontiers in Climate*, **4**, 814181.

Turner, J., Lu, H., White, I., King, J. C., Phillips, T., Hosking, J. S., Bracegirdle, T.J., Marshall., G.J., Mulvaney, R. and Deb, P. (2016). Absence of 21st century warming on Antarctic Peninsula consistent with natural variability. *Nature*, **535**(7612), 411-415.

Turton, J. V., Kirchgaessner, A., Ross, A. N. and King, J. C. (2018). The spatial distribution and temporal variability of föhn winds over the Larsen C ice shelf, Antarctica. *Quarterly Journal of the Royal Meteorological Society*, **144**(713), 1169-1178.

Ummenhofer, C.C., and England, M.H. (2007) Interannual extremes in New Zealand Precipitation linked to modes of Southern Hemisphere climate variability. *Journal of Climate*, **20**(21), 5418-5440.

Uuemaa, E., Ahi, S., Montibeller, B., Muru, M., and Kmoch, A. (2020) Vertical accuracy of freely available global digital elevation models (ASTER, AW3D30, MERIT, TanDEM-X, SRTM, and NASADEM). *Remote Sensing*, **12**(21), 3482.

van Lipzig, N. P. M., King, J. C., Lachlan-Cope, T. A., and Van den Broeke, M. R. (2004). Precipitation, sublimation, and snow drift in the Antarctic Peninsula region from a regional atmospheric model. *Journal of Geophysical Research: Atmospheres*, **109**(D24).

Van Pelt, W. J., Pohjola, V. A., and Reijmer, C. H. (2016). The changing impact of snow conditions and refreezing on the mass balance of an idealized Svalbard glacier. *Frontiers in Earth Science*, **4**, 102.

van Wessem, J. M., Ligtenberg, S. R. M., Reijmer, C. H., Van De Berg, W. J., Van Den Broeke, M. R., Barrand, N. E., Thomas, E.R., Turner, J., Wuite, J., Scambos, T.A. and Van Meijgaard, E. (2016). The modelled surface mass balance of the Antarctic Peninsula at 5.5 km horizontal resolution. *The Cryosphere*, **10**(1), 271-285.

Vázquez-Jiménez, R., Romero-Calcerrada, R., Ramos-Bernal, R.N., Arrogante-Funes, P., and Novillo, C.J., (2017) Topographic Correction to Landsat Imagery through Slope Classification by Applying the SCS + C Method in Mountainous Forest Areas. *International Journal of Geo-information*, **6**(287).

Veettil, B. and de Souza, S. F. (2017). Study of 40-year glacier retreat in the northern region of the Cordillera Vilcanota, Peru, using satellite images: preliminary results. *Remote Sensing Letters*, **8**(1), 78-85.

Veettil, B. K., Bremer, U. F., de Souza, S. F., Maier, É. L. B. and Simões, J. C. (2016b). Influence of ENSO and PDO on mountain glaciers in the outer tropics: case studies in Bolivia. *Theoretical and applied climatology*, **125**, 757-768.

Veettil, B. K., Leandro Bayer Maier, É., Bremer, U. F. and de Souza, S. F. (2014). Combined influence of PDO and ENSO on northern Andean glaciers: a case study on the Cotopaxi ice-covered volcano, Ecuador. *Climate dynamics*, **43**, 3439-3448.

Veettil, B. K., Wang, S., Simões, J. C., Ruiz Pereira, S. F. and de Souza, S. F. (2018). Regional climate forcing and topographic influence on glacier shrinkage: eastern cordilleras of Peru. *International Journal of Climatology*, **38**(2), 979-995.

Veettil, B.K. and Simões, J.C. (2019) The 2015/16 El Niño-related glacier changes in the tropical Andes. *Frontiers in Earth Science*, **13**, 422–429.

Veettil, B.K., Bremer, U.F., Florêncio de Souza, S., Maier, E.L.B. and Simões, J.C. (2016a) Variations in annual snowline and area of an ice- covered stratovolcano in the Cordillera Ampato, Peru, using remote sensing data (1986–2014). *Geocarto International*.

Veettil, B.K., Wang, S., Bremer, U.F., Florêncio de Souza, S., and Simões, J.C. (2017) Recent trends in annual snowline variations in the northern wet outer tropics: case studies from the southern Cordillera Blanca, Peru. *Theoretical and Applied Climatology*, **129**, 213-227.

Vera, C. S., and Osman, M. (2018). Activity of the Southern Annular Mode during 2015–2016 El Niño event and its impact on Southern Hemisphere climate anomalies. *International Journal of Climatology*, **38**, e1288-e1295.

Vergara, I., Moreiras, S. M., Araneo, D., and Garreaud, R. (2020). Geo-climatic hazards in the eastern subtropical Andes: Distribution, Climate Drivers and Trends. *Natural Hazards and Earth System Sciences*, **20**(5), 1353-1367.

Viale, M., and Garreaud, R. (2014). Summer precipitation events over the western slope of the subtropical Andes. *Monthly Weather Review*, **142**(3), 1074-1092.

Viale, M., Bianchi, E., Cara, L., Ruiz, L. E., Villalba, R., Pitte, P., Masiokas, M., Rivera, J. and Zalazar, L. (2019). Contrasting climates at both sides of the Andes in Argentina and Chile. *Frontiers in Environmental Science*, **7**, 69.

Vicente-Serrano, S. M., López-Moreno, J. I., Correa, K., Avalos, G., Bazo, J., Azorin-Molina, C., et al. (2018). Recent changes in monthly surface air temperature over Peru, 1964–2014. *International Journal of Climatology*, **38**(1), 283-306.

Vuille, M. and Ammann, C. (1997) Regional Snowfall Patterns in the High, Arid Andes. *Climatic Change*, **36**, 413–423.

Vuille, M., Bradley, R. S., and Keimig, F. (2000). Climate variability in the Andes of Ecuador and its relation to tropical Pacific and Atlantic sea surface temperature anomalies. *Journal of climate*, **13**(14), 2520-2535.

Vuille, M., Carey, M., Huggel, C., Buytaert, W., Rabatel, A., Jacobsen, D., et al. (2018). Rapid decline of snow and ice in the tropical Andes–Impacts, uncertainties and challenges ahead. *Earth-science reviews*, **176**, 195-213.

Vuille, M., Franquist, E., Garreaud, R., Lavado Casimiro, W. S., and Cáceres, B. (2015). Impact of the global warming hiatus on Andean temperature. *Journal of Geophysical Research: Atmospheres*, **120**(9), 3745-3757.

Vuille, M., Kaser, G. and Juen, I. (2008). Glacier mass balance variability in the Cordillera Blanca, Peru and its relationship with climate and the large-scale circulation. *Global and Planetary Change*, **62**(1-2), 14-28.

Vuille, M., Kaser, G., and Juen, I. (2008). Glacier mass balance variability in the Cordillera Blanca, Peru and its relationship with climate and the large-scale circulation. *Global and Planetary Change*, **62**(1-2), 14-28.

Wagnon, P., Ribstein, P., Francou, B. and Sicart, J. E. (2001). Anomalous heat and mass balance budget of Glaciar Zongo, Bolivia, during the 1997/98, El Nino year. *Journal of Glaciology*, **47**, 21–28.

Wang, G., Cai, W., Gan, B., Wu, L., Santoso, A., Lin, X., Chen, Z. and McPhaden, M.J. (2017) Continued increase of extreme El Niño frequency long after 1.5 °C warming stabilization. *Nature Climate Change*, **7**, 568–572.

Wang, J., Tang, Z., Deng, G., Hu, G., You, Y., and Zhao, Y. (2023). Landsat Satellites Observed Dynamics of Snowline Altitude at the End of the Melting Season, Himalayas, 1991–2022. *Remote Sensing*, **15**(10), 2534.

Wille, J. D., Favier, V., Jourdain, N. C., Kittel, C., Turton, J. V., Agosta, C., et al. (2022). Intense atmospheric rivers can weaken ice shelf stability at the Antarctic Peninsula. *Communications Earth & Environment*, **3**(1), 90.

Willis, M.J., Melkonian, A.K., Pritchard, M.E., and Rivera, A. (2012) Ice loss from the Southern Patagonian Ice Field, South America, between 2000 and 2012. *Geophysical Research Letters*, **39**(17).

Wilson, R., Carrión, D. and Rivera, A. (2016). Detailed dynamic, geometric and supraglacial moraine data for Glaciar Pio XI, the only surge-type glacier of the Southern Patagonia Icefield. *Annals of Glaciology*, **57**(73), 119-130.

Young, N.E., Anderson, R.A., Chignell, S.M., Vorster, A.G., Lawrence, R., and Evangelista, P.H. (2017) A survival guide to Landsat preprocessing. Ecology: *Ecological Society of America*, **98**(4), 920-932.

Zazulie, N., Rusticucci, M. and Raga, G. B. (2017). Regional climate of the subtropical central Andes using high-resolution CMIP5 models—part I: past performance (1980–2005). *Climate Dynamics*, **49**, 3937-3957.

Zemp, M., Frey, H., Gärtner-Roer, I., Nussbaumer, S., Hoelzle, M., Paul, F., Haeberli, W., Denzinger, F., Ahlstrøm, A.P., Anderson, B., Bajracharya, S., Baroni, C., Braun, L.N., Cáceres, B.E., Casassa, G., Cobos, G., Dávila, L.R., Granados, H.D., Demuth, M.N., Espizua, L., Fischer, A., Fujita, K., Gadek, B., Ghazanfar, A., Hagen, J.O., Holmlund, P., Karimi, N., Li, Z., Pelto, M., Pitte, P., Popovnin, V.V., Portocarrero, C.A., Prinz, R., Sangewar, C.V., Severskiy, I., Sigurðsson, O., Soruco, A., Usubaliev, R., and Vincent, C. (2015) Historically unprecedented global glacier decline in the early 21st century. *Journal of Glaciology*, **61**(228), 745-762.

Zemp, M., Huss, M., Thibert, E., Eckert, N., McNabb, R., Huber, J., and Cogley, JG (2019). Global glacier mass changes and their contributions to sea-level rise from 1961 to 2016. *Nature*, **568**(7752), 382-386.

Zhang, Q. and Kang, S. (2017) Glacier snowline altitude variations in the Pamirs, Tajikistan, 1998-2013: insights from remote sensing images. *Remote Sensing Letters*, **8**(12), 1220-1229.

Zhou, C. and Zheng, L. (2017) Mapping radar glacier zones and dry snow line in the Antarctic Peninsula using Sentinel-1 images. *Remote Sensing*, **9**(11), 1171.

Zhou, C., Liu, Y., and Zheng, L. (2022). Satellite-derived dry-snow line as an indicator of the local climate on the Antarctic Peninsula. *Journal of Glaciology*, **68**(267), 54-64.

Zou, X., Rowe, P. M., Gorodetskaya, I., Bromwich, D. H., Lazzara, M. A., Cordero, R. R., et al. (2022). Strong Warming over the Antarctic Peninsula during Combined Atmospheric River and Foehn Events: Contribution of Shortwave Radiation and Turbulence. *Journal of Geophysical Research: Atmospheres*, e2022JD038138.

Zwally, H.J., and Fiegles, S. (1994) Extent and duration of Antarctic surface melting. *Journal of Glaciology*, **40**(136), 463-475.

Zwally, H.J., Giovinetto, M.B., Beckley, M.A., and Saba, J.L. (2012) Antarctic and Greenland Drainage Systems. *GSFC Cryospheric Sciences Laboratory.*

## Appendix A

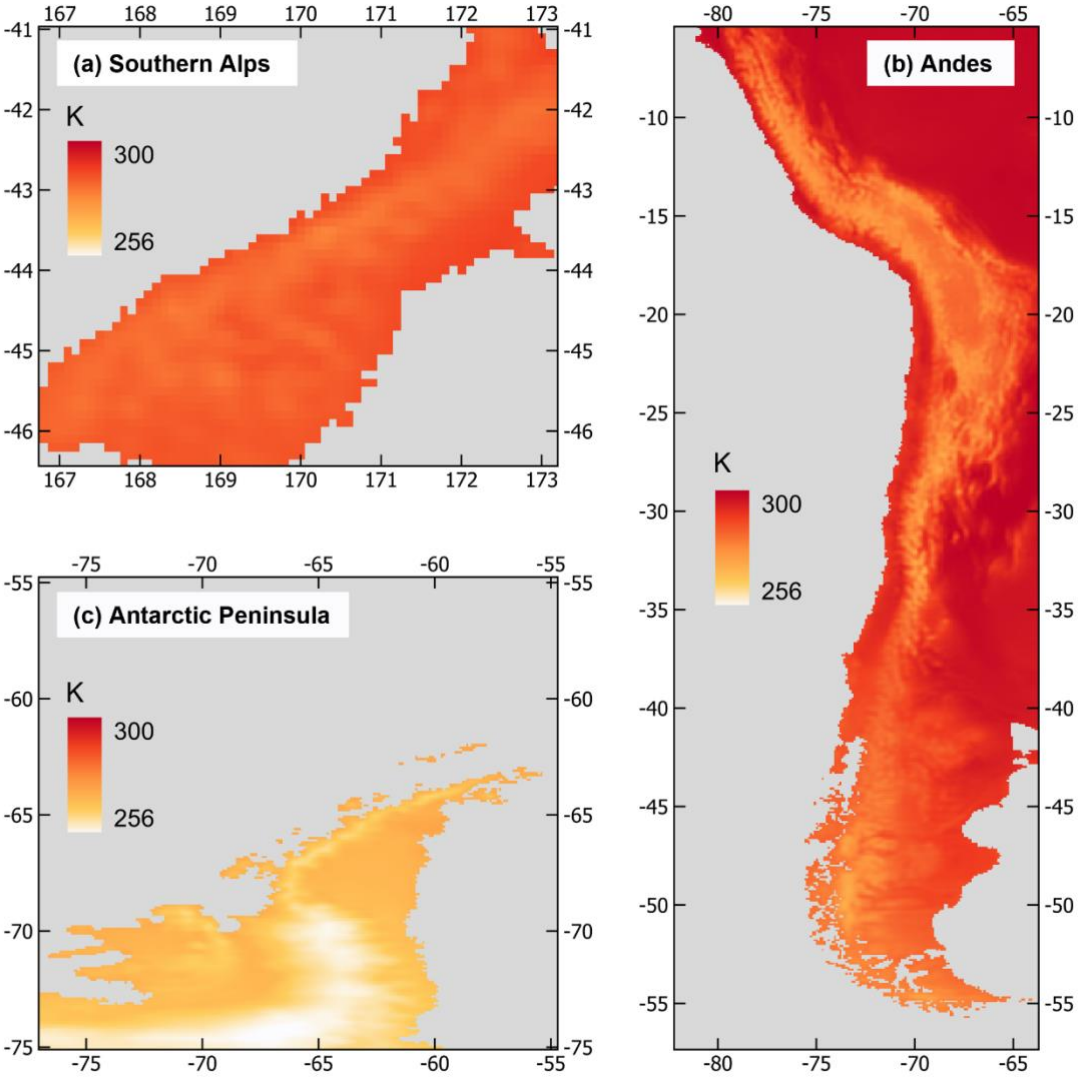


**Figure A1.** ERA5-Land median summer 2 m air temperature across the Southern Hemisphere study regions, 2000-2020.

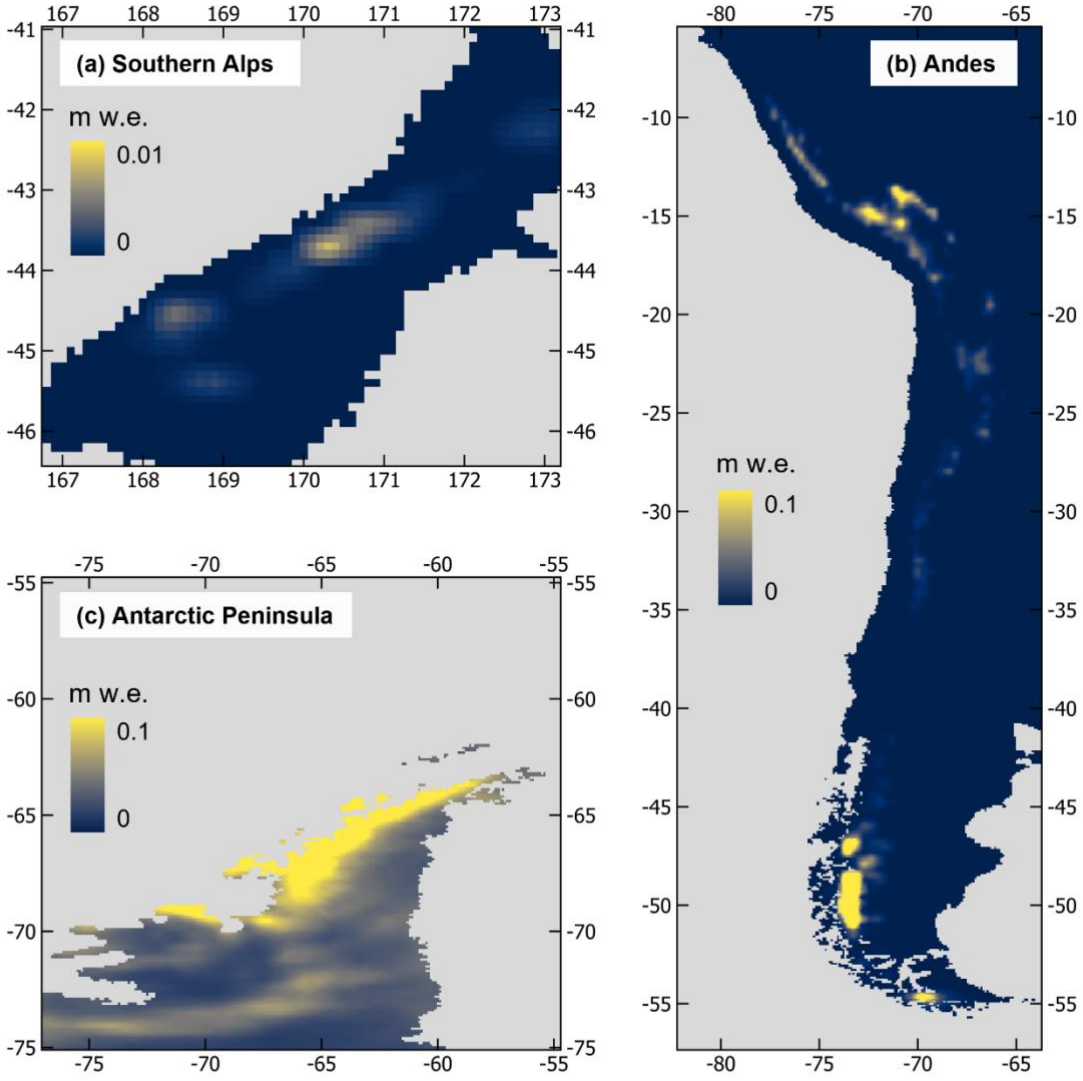


**Figure A2.** ERA5-Land median summer monthly snowfall sum across the Southern Hemisphere study regions, 2000-2020. Note scale difference in (a).

## Appendix B

**Table A1.** Geometries used to define smaller-scale Andean sub-regions.

| Site | Location (N, E, S, W) |
|---|---|
| Northern Patagonia | -47.70, -72.50, -48.20, -74.50 |
| Southern Patagonia | -48.20, -72.50, -51.70, -74.50 |
| Cord. Blanca | -8.60, -77.12, -10.0, -77.89 |
| Cord. Darwin | -54.20, -68.50, -55.00, -71.80 |
| Cord. Vilaconta | -13.39, -70.66, -14.17, -71.41 |

**Table A2.** List of Southern Alps test glaciers (n=34).

| Glacier Name | GLIMS ID |
|---|---|
| Barrier Peak | G167720E44851S |
| Llawrenny Peaks | G167794E44656S |
| Mount Gendarme | G167942E44789S |
| Mount Gunn | G168093E44759S |
| Ailsa Mounts. | G168187E44786S |
| Park Pass | G168242E44591S |
| Bryant | G168287E44824S |
| Findlay | G168446E44323S |
| Mount Larkins | G168482E44881S |
| Snowy Creek | G168635E44554S |
| Mount Stuart | G169261E44109S |
| Brewster | G169437E44072S |
| Thurneyson | G169595E44165S |
| Jack | G169638E43810S |
| Mount McKenzie | G169732E43949S |
| Blair | G169765E43987S |
| Jackson | G169791E43889S |
| Glenmary | G169884E43993S |
| Chancellor Dome | G170126E43510S |
| Salisbury | G170225E43472S |
| Langdale | G170269E43586S |
| Tasman | G170307E43519S |
| Ridge | G170363E43622S |
| Siege | G170538E43272S |
| Vertebrae 12 | G170611E43318S |
| Vertebrae 25 | G170615E43324S |
| Kea | G170806E43177S |
| Dainty | G170887E43232S |
| Mount Butler | G170937E43250S |
| South Cameron | G170988E43355S |
| Retreat | G171304E42963S |
| Marmaduke-Dixon | G171383E42988S |
| Rolleston | G171526E42890S |